

DOSIMETRIC TRANSFERABILITY OF A MEDICAL LINEAR ACCELERATOR
MOUNTED MINI-BEAM COLLIMATOR

A Thesis Submitted to the College of
Graduate Studies and Research
In Partial Fulfillment of the Requirements
For the Degree of Master of Science
In the Department of Physics and Engineering Physics
University of Saskatchewan
Saskatoon
Canada

By

William Michael Davis

© Copyright William Michael Davis, December 2016. All rights reserved.

Permission to Use:

In presenting this thesis in partial fulfilment of the requirements for a Postgraduate degree from the University of Saskatchewan, I agree that the Libraries of this University may make it freely available for inspection. I further agree that permission for copying of this thesis in any manner, in whole or in part, for scholarly purposes may be granted by the professor or professors who supervised my thesis work or, in their absence, by the Head of the Department or the Dean of the College in which my thesis work was done. It is understood that any copying or publication or use of this thesis or parts thereof for financial gain shall not be allowed without my written permission. It is also understood that due recognition shall be given to me and to the University of Saskatchewan in any scholarly use which may be made of any material in my thesis.

Requests for permission to copy or to make other use of material in this thesis in whole or part should be addressed to:

Head of the Department of Physics and Engineering Physics

University of Saskatchewan

Saskatoon, SK, Canada, S7N 5E2

ABSTRACT

The goal of this study was the dosimetric characterization of a mini-beam collimator on three clinically beam matched Varian iX linear accelerators. Measurements of the beam quality (%DD(10)), peak-to-valley dose ratio (PVDR), collimator factor ($CF_{f_{mini}}^w$), and relative output factor ($OF_{f_{mini}}^w$) were carried out for 2 cm x 2 cm, 3 cm x 3 cm, 4 cm x 4 cm, and 5 cm x 5 cm mini-beam collimated 6 MV fields on each linear accelerator. As well, Monte Carlo simulation of the mini-beam collimated fields were used to link the measurement results to a validated linear accelerator model. The quality of the mini-beam collimated field was clinically equivalent to that of the open field. Changes in the mini-beam collimated field in response to changes in both field size and collimator inclination were consistent across all three linear accelerators. However, PVDR, collimator factors, and relative output factors varied in excess of the measurement uncertainty, revealing a difference in the mini-beam collimated fields of each linear accelerator. The change in PVDR was proportional to that of the collimator factor and relative output factor. The Monte Carlo simulations showed that variation in the full-width half-maximum of the linear accelerators' electron beam incident on the Bremsstrahlung target correlated to the variation in collimator factor and PVDR across the accelerators. These results demonstrate that while the mini-beam collimated field varies across linear accelerators, the effect can be accounted for in the linear accelerator model, allowing the planning and delivery of mini-beam collimated fields using medical linear accelerators.

ACKNOWLEDGMENTS

I wish to express my gratitude to my supervisors, Dr. Gavin Cranmer-Sargison and Dr. Chary Rangacharyulu, for all of their insight, teaching, and encouragement during this work. Neither the project nor my education could have been successful without their guidance.

I also wish to thank Cody Crewson and Dr. Andrew Alexander for their valuable advice and assistance throughout the investigation.

Finally, I would be remiss not to thank my parents, Michael and Melanie Davis, for their steadfast love and support throughout my studies.

Funding in support of this project was provided by the Sylvia Fedoruk Canadian Centre for Nuclear Innovation, Grant # J2014-0008.

TABLE OF CONTENTS

Page

PERMISSION TO USE	i
ABSTRACT	ii
ACKNOWLEDGMENTS	iii
LIST OF TABLES	vii
LIST OF FIGURES	viii
LIST OF ABBREVIATIONS	x
 1 INTRODUCTION	 1
1.1. External Beam Radiotherapy	2
1.2. Fractionation	3
1.3. Mini-Beam Collimator Transferability Study	5
1.4. Outline	6
 2 IONIZING RADIATION	 8
2.1. Directly-Ionizing Radiation	9
2.1.1. Coulomb Interactions	9
2.1.2. Clasification of Electron Interactions	12
2.1.3. Stopping Power	12
2.2. Indirectly-Ionizing Radiation	14
2.2.1. Photoelectric Interactions	15
2.2.2. Compton and Rayleigh Scattering	17
2.2.3. Pair and Triplet Production	19
 3 DOSIMETRY	 22
3.1. Dosimetric Quantities	22
3.1.1. Fluence	22
3.1.2. Kerma	23
3.1.3. Absorbed Dose	24
3.1.4. Charged Particle Equilibrium	25
3.2. Cavity Theory	26
3.3. Dosimeters	29
3.3.1. Ionization Chambers	30
3.3.2. Diode Detectors	30
3.4. Dosimetric Measurements	30
3.4.1. Reference Dosimetry	32
3.4.1.1. Beam Quality	32
3.4.1.2. Point Dose Measurement	33
3.4.2. Relative Dosimetry	33
3.4.2.1. Percent Depth Dose	33
3.4.2.2. Dose Profiles	35
3.4.2.3. Point Dose and Relative Output Factors	35
3.5. Uncertainty in Dose	36

4	PRINCIPLES OF MONTE CARLO SIMULATION	38
4.1.	History of Monte Carlo Method	38
4.2.	Theory of the Monte Carlo Method	39
4.3.	Monte Carlo Particle Transport	41
4.3.1.	Electron Transport	42
4.3.2.	Photon Transport	44
4.4.	Variance Reduction Techniques	45
4.4.1.	Particle Splitting	45
4.4.2.	Russian Roulette	46
4.4.3.	Range Rejection	47
4.4.4.	Photon Forcing	47
4.4.5.	Cross Section Enhancement	48
4.5.	EGSnrc	48
4.5.1.	BEAMnrc	48
4.5.2.	DOSXYZnrc and DOSRZnrc	49
5	COLLIMATOR TRANSFERABILITY: DOSIMETRIC CHARACTERIZATION	51
5.1.	The Mini-Beam Collimator.....	52
5.1.1.	Design	52
5.1.2.	Dosimetric Framework	53
5.2.	Experimental Apparatus.....	56
5.2.1.	Medical Linear Accelerators	56
5.2.2.	Diode Detectors	57
5.2.3.	Water Phantom	58
5.2.4.	MEPHYSTO mc ²	59
5.3.	Experimental Setup.....	59
5.3.1.	Water Phantom Setup	60
5.3.2.	Detector Centering	60
5.3.3.	Mini-Beam Collimator Centering	61
5.3.4.	Mini-Beam Collimator Alignment	62
5.4.	Measurement Procedure: Percent Depth Dose and Dose Profile.....	64
5.4.1.	Percent Depth Dose Measurement	65
5.4.2.	Profile Measurement	65
5.4.3.	Data Collation	66
5.5.	Measurement Procedure: Relative Output Factors	66
5.5.1.	Effects of Collimator Inclination Upon Collimator Factor	67
5.5.2.	Uncertainty in Measurements	68
5.6.	Results of Dosimetric Characterization	68
5.6.1.	Open Field Measurements	69
5.6.2.	Mini-Beam Collimated Percent Depth Dose and Dose Profiles	69
5.6.2.1.	Percent Depth Dose	70
5.6.2.2.	Mini-Beam Dose Profile	73
5.6.3.	Collimator Factors	73
5.6.4.	Collimator Factor as a Function of Collimator Inclination	74
5.6.5.	Aligned Dose Profiles	76

5.6.6. Aligned Collimator Factors	78
5.6.6.1. Measured Collimator Factors	78
5.6.6.2. Corrected Collimator Factors	78
5.7. Discussion	79
5.7.1. Open Field Measurements	79
5.7.2. Percent Deth Dose and Dose Profile	80
5.7.3. Collimator Factors and Relative Output Factors	81
6 COLLIMATOR TRANSFERABILITY: MONTE CARLO SIMULATIONS	83
6.1. Simulation Procedure	83
6.1.1. Treatment Head	84
6.1.2. Linac Field	85
6.1.3. Dose Scoring	86
6.2. Parameter Testing	88
6.2.1. Electron Beam FWHM	89
6.2.2. Source-to-Collimator Distance	89
6.3. Results of Parameter Testing	90
6.3.1. Collimator Factor and PVDR as a Function of Electron Beam FWHM	90
6.3.2. Collimator Factor as a Function of Source-to-Collimator Distance	92
6.4. Mini-Beam Correction Factors	93
6.4.1. Calculation	94
6.4.2. Corrected Collimator Factors	95
6.4.3. Corrected Relative Output Factors	96
6.5. Discussion	97
6.5.1. Parameter Testing	97
6.5.2. Corrected Collimator Factors and Relative Output Factors	98
7 CONCLUSION	100
7.1. Transferability	100
7.2. Recommended Procedure for Characterization	102
7.3. Related Work	104
APPENDIX A: EXAMPLE EGSnrc INPUT FILES	106
A.1. BEAMnrc Input for the Treatment Head	106
A.2. BEAMnrc Input for the Linac Field	114
A.3. DOSRZnrc Input for the Dose to Detector	119
APPENDIX B: PERMISSION TO REPRODUCE FIGURES	123
LIST OF REFERENCES	126

LIST OF TABLES

<u>Table</u>	<u>page</u>
5.1. Open field metrics.....	69
5.2. Open field relative output factors	70
5.3. Beam qualities.....	71
5.4. Measured PVDR for unaligned collimator	72
5.5. Measured PVDR for aligned collimator	77
6.1. Fitted electron beam FWHM	92
6.2. Linac- and detector-specific small field correction factors.....	95
6.3. Average collimator factors and relative output factors in water.....	98

LIST OF FIGURES

<u>Figure</u>	<u>page</u>
1.1. Medical linear accelerator.....	3
2.1. Electron-atom interactions	12
2.2. Storm-Israel photon-atom interaction cross sections	16
2.3. Photoelectric interaction and Auger cascade	17
2.4. Compton scattering	19
2.5. Pair and triplet production	21
3.1. Depth dose and collisional kerma of a photon beam	26
3.2. Dosimeter in a medium.....	28
3.3. SSD and SAD experimental configurations	31
3.4. Percent depth dose	34
3.5. Dose profile.....	36
4.1. Condensed history electron transport.....	43
5.1. Mini-beam dose profile.....	53
5.2. The mini-beam collimator.....	54
5.3. Collimator factor measurement.....	55
5.4. Experimental setup.....	57
5.5. Measurement axes.....	58
5.6. Collimator alignment effects.....	62
5.7. Dectector orientation.....	65
5.8. Measured percent depth dose	71
5.9. Measured unaligned dose profiles	72
5.10. Measured unaligned collimator factors vs field size.....	74
5.11. Measured unaligned collimator factors vs collimator inclination.....	75

5.12. Measured aligned dose profile	77
5.13. Measured aligned collimator factors vs field size.....	79
5.14. Measured aligned mini-beam relative output factors vs field size	80
6.1. Simulated linac components	84
6.2. Simulated collimator factors vs electron beam FWHM	91
6.3. Simulated PVDR vs electron beam FWHM	92
6.4. Simulated collimator factors vs source-to-collimator distance	95
6.5. Collimator factors in water vs field size	93
6.6. Mini-beam relative output factors in water vs field size	96

LIST OF ABBREVIATIONS

<u>Abbreviation</u>	<u>Page</u>
Linac - Linear Accelerator	2
kV - Kilovoltage	2
MV - Megavoltage	2
MU - Monitor Unit	2
MRT - Micro-Beam Radiotherapy	4
MBRT - Mini-Beam Radiotherapy	5
SCC - Saskatoon Cancer Centre	5
E_B - Binding Energy	8
m - Mass	10
v - Velocity	10
θ - Electron Scattering Angle	10
ϕ - Electron Emission Angle	10
dE - Change in Energy	12
dl - Change in Position	12
S - Linear Stopping Power	12
$\frac{S}{\rho}$ - Mass Stopping Power	13
ρ - Density	13
S_{col} - Collisional Stopping Power	13
S_{rad} - Radiative Stopping Power	13
LET - Linear Energy Transfer	13
Δ - Energy Threshold	13
μ - Linear Attenuation Coefficient	14

τ - Photoelectric Interaction Cross Section	14
σ - Scattering Cross Section	14
κ - Pair/ Triplet Production Cross Section	14
μ_m - Mass Attenuation Coefficient	14
$h\nu$ - Photon Energy	8
E_e - Electron Energy	8
Φ - Particle Fluence	22
Ψ - Energy Fluence	23
K - Kerma	23
Gy - Gray	23
K_{col} - Collisional Kerma	23
D - Dose	24
d_{max} - Maximum Dose Depth	25
$s_{A,B}$ - Stopping Power Ratio	27
M - Detector Signal	29
SSD - Source-to-Surface Distance	31
SAD - Source-to-Axis Distance	31
%DD - Percent Depth Dose	33
FWHM - Full-Width Half-Maximum	35
OF - Relative Output Factor	35
u - Uncertainty	37
σ - Standard Deviation	37
Pr - Probability	38
RNG - Random Number Generator	39
r - Pseudo-Random Number	40

R - Weighted Pseudo-Random Number.....	40
CSDA - Continuous Slowing Down Approximation	43
VRT - Variance Reduction Technique	46
CF - Collimator Factor.....	54
f_{clin} - Clinical Field of Interest.....	53
f_{mini} - Mini-Beam Collimated Field of Interest.....	53
f_{ref} - Reference Field	54
PTWe - PTW TN60017 Dosimetry Diode E.....	57
SFD - IBA Dosimetry Stereotactic Field Diode	57
PVDR - Peak-to-Valley Dose Ratio	66
$k_{f_{\text{mini}}}^{\text{det}}$ - Small Field Correction Factor for the Mini-Beam Collimated Field	93

CHAPTER 1

INTRODUCTION

Radiation oncology involves the use of ionizing radiation in the treatment of cancer. The ionizations produced by high energy radiation can disrupt molecular structures. When incident on living cells, ionizing radiation is known to damage DNA, leading to errors in repair or replication. Rapidly multiplying cells, such as cancer cells, are more likely to replicate the damaged strand before it can be repaired [1]. These errors can render the cell non-viable, leading to a decrease in cell population when it is unable to multiply, or simply kill it outright. However, the same effects occur in healthy cells, causing damage to surrounding tissue. The trade-off between killing cancer cells and sparing healthy cells is quantified by the therapeutic index, a comparison of the likelihood of tumor control versus healthy cell death [2]. Increased therapeutic index is likely to improve patient outcomes, and is therefore a desirable feature in new or refined treatment methods.

The goal of this project is the dosimetric characterization of a mini-beam collimator intended for use with medical linear accelerators. The collimator is an attachment for linear accelerators used in external beam radiotherapy, which allows the use of spatial fractionation techniques by any treatment center.

1.1. External Beam Radiotherapy

Methods of delivering radiation to patients can be divided into external and internal radiotherapy, depending on the location of the source. External beam radiotherapy involves the use of externally-generated radiation beams to deliver radiation to targets within the body.

Medical linear accelerators (linacs) are used to generate radiation beams for use in radiation oncology. Electrons are accelerated into a magnetic field generated by a bending magnet. This magnet rotates the beam through 270° onto an aperture. Only electrons at or near the selected energy will pass through the aperture, with the paths of the other electrons being bent too little or too much, striking the shielding in the accelerator treatment head. The collimated electron beam is then incident upon either a Bremsstrahlung target, if being used to create a photon beam, or a scattering foil, if being used to create an electron beam. This beam is shaped according to the treatment plan by a set of jaws and the multi-leaf collimators. These components are located in a gantry, which rotates around a center point known as the isocenter. This configuration allows for the delivery of radiation beams from multiple angles. Figure 1.1 depicts a medical linear accelerator of this type.

Since photons produced by Bremsstrahlung interaction have a range of energies, photon beam energies are specified by the accelerating potential of the electron beam, in units of peak kilovoltage (kV) or peak Megavoltage (MV). The duration of the beam delivery is defined in terms of monitor units (MU), defined such that 1 MU beam-on time for a 10 cm x 10 cm field delivers 1 cGy to a point at the depth of maximum dose in water. X-ray beams irradiate everything in the path, rather than only the target volume. Treatments must account for this effect to maximize the therapeutic index.

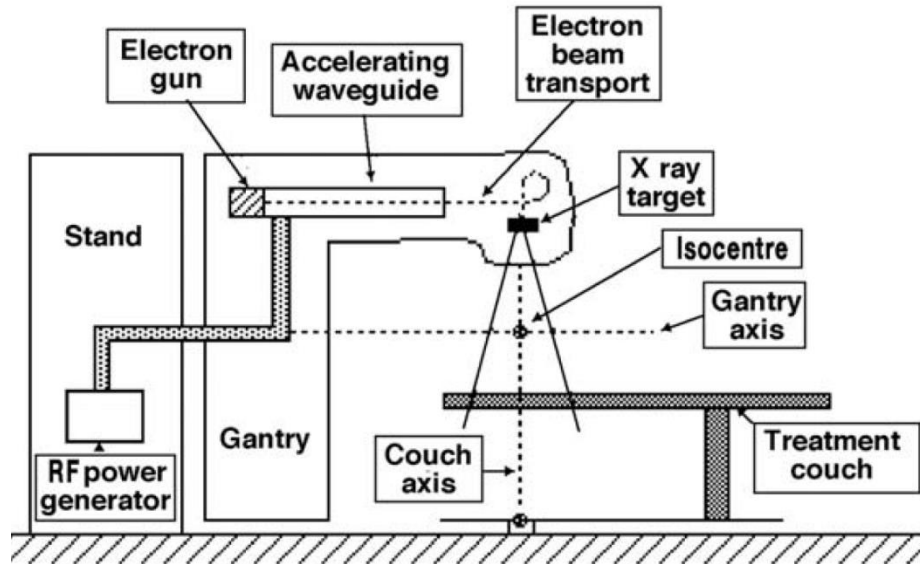


Figure 1.1. A medical linear accelerator used to produce high energy X-rays. All major components are shown. Image from Podgorsak 2005 [3], used with permission.

1.2. Fractionation

Several methods to increase the therapeutic index by reducing healthy cell death have been developed. A category of these techniques are referred to as fractionation, splitting the delivery of radiation in some way to reduce the damage to healthy cells. Temporal fractionation delivers the planned dose in multiple “fractions”, separated by a fixed period of time. By splitting the delivery, the repair mechanisms of healthy cells have time to repair DNA damage. This effect is not as significant in cancer cells; as mentioned above, DNA damage tends to propagate before the repair mechanisms can take effect, due to their more rapid reproduction [1]. Temporal fractionation is a commonly used and effective treatment method, but even greater benefits are sought via alternative methods.

A less common, though long understood method is spatial fractionation. Unlike beams intended to deliver a spatially-invariant dose across the field, spatial fractionation techniques deliver dosages in a non-uniform pattern. One of the earliest spatial fractionation techniques was

known as GRID therapy [4], which delivers an array of centimeter scale pencil beams. Originally used to limit normal tissue toxicity when irradiating deep targets, it fell out of favor with the development of medical linear accelerators. However, in recent years, it has been revived for the purpose of reducing the volume of shallow bulky tumors. GRID therapy can be delivered by conventional medical linear accelerators through the use of a specialized collimator [5, 6] or multi-leaf collimation [7, 8]. These techniques have shown promise for the control of bulky tumours, but have limited application for treating smaller volumes.

Another variant, micro-beam radiotherapy (MRT) [9, 10] makes use of synchrotron-generated photon beams. MRT is delivered using an array of beams with an approximate full-width-half-maximum of $25 - 75 \mu\text{m}$ with $100 - 400 \mu\text{m}$ spacing, as measured at the target surface [11]. The use of synchrotron-generated photons facilitates the fine control over beam energy and the spatial distribution of the micro-beam array. MRT delivers extremely high doses to tightly defined regions. Studies in rats have obtained promising results when examining the use of micro-beams to treat brain lesions in rats [12, 13, 14, 15], achieving tumour control while inflicting minimal damage to healthy tissue around the directly-irradiated region, in what is called the “tissue-sparing effect” [16, 17, 18]. However, MRT has two major impediments to widespread use. Generation of micro-beams requires a synchrotron, limiting the study or use of MRT to major centers. As well, micro-beams are poorly suited for irradiating target volumes within the patient due to their low energy (approximately 200 kV).

One possibility to overcome these limitations is the development of higher energy spatially fractionated beams, which are suited to irradiating deeper targets. Increased beam energy also allows the delivery of this variety of spatially fractionated treatment using conventional medical linear accelerators, since higher energy beams can deliver the needed doses without requiring the

intensity of a synchrotron source. Treatments of this type may make use of thicker beams, up to millimeter width, called mini-beams, in what is called mini-beam radiotherapy (MBRT). Well-defined kV mini-beams up to 0.68 mm in width have been observed to exhibit the same tissue-sparing effect seen for micro-beams [19, 20, 21]. That MBRT may possess the radiobiological benefits of MRT without the accompanying limitations in accessibility makes it an intriguing treatment modality. The use of an accessory to generate mini-beam arrays using a kV orthovoltage beam [22] was studied as a step towards widely accessible MBRT. The study demonstrated the feasibility of the mini-beam collimator concept, but revealed limitations imposed by the low beam intensity of the orthovoltage machine.

1.3. Mini-Beam Collimator Transferability Study

A mini-beam collimator for use with 6 MV photon beams has been designed and constructed at the Saskatoon Cancer Centre. The collimator is intended to serve as an accessory for Varian iX linear accelerators.

The mini-beam collimator was initially commissioned for one of the medical linear accelerators at the Saskatoon Cancer Centre (SCC) [23]. The design process used Monte Carlo simulations to refine the collimator design. After the collimator was constructed, the first step was dosimetric characterization to validate the design. Dose profiles and relative output factors¹ were measured for the mini-beam collimated field.

By comparing the simulated and measured results, the initial Monte Carlo model of the collimator and detectors was matched to the completed model. However, to fulfill the intention of

¹Both dose profiles and relative output factors are discussed in greater detail in Chapter 3.

making mini-beam radiotherapy widely available, the mini-beam collimated field must be shown to exhibit consistent dosimetric characteristics on different medical linear accelerators.

In this work, dosimetric characterization of the mini-beam collimator was carried out on three clinically beam matched² Varian accelerators operating at a nominal 6 MV photon beam mode. The characterization process involved measuring the percent depth dose curves, dose profiles, and collimator factors on each linear accelerator. The results were used to determine how the mini-beam collimated field varied between beam matched accelerators.

Monte Carlo simulations of electron and photon transport were used to study the response of the collimated field output to variations in the linac parameters across linear accelerators. By simulating the collimated beam incident on the detectors used in the study, specific aspects of the collimated field could be examined. The simulation results were used to identify the cause of differences between the collimated outputs on different accelerators.

1.4. Outline

This work covers the characterization and analysis of the mini-beam collimator on multiple linear accelerators.

Chapter 2 covers the basics of ionizing radiation and its interactions with matter. Directly-ionizing radiation and indirectly-ionizing radiation are each introduced. The process by which directly-ionizing radiation interacts with the medium is discussed, followed by the classification of these interactions. The concept of stopping power is introduced. Indirectly-ionizing radiation

² The “beam matched” criterion is defined in Chapter 5.

is similarly described. The three main interactions of indirectly-ionizing radiation: the photoelectric effect, scattering, and pair production are discussed.

Chapter 3 discusses the measurement of radiation as used in the study. The key quantities are introduced. An overview of cavity theory, the theoretical basis for dosimetry, is given, followed by a discussion of dosimeters and their use. Finally, the specific measurements used in the study are described in detail.

Chapter 4 introduces Monte Carlo simulation methods as applied to the study of radiation beams. A brief history of Monte Carlo methods is given. Next, the mechanics of Monte Carlo particle transport are described. A discussion of the uncertainty analysis and management of Monte Carlo simulations follows. Finally, the EGSnrc Monte Carlo simulation package is introduced and the individual simulation codes used in this study are described.

Chapter 5 explains the procedure followed for the dosimetric characterization measurements of the mini-beam collimated field. The experimental apparatus is described. An outline of the procedure for each of the measurements is given. The results of the measurements are presented and discussed.

Chapter 6 describes the procedure used for Monte Carlo simulation of the mini-beam collimated field. First, a description of the accelerator model used in the simulations is given. A description of the process, with the inputs and outputs of each step follows. The results of the simulations are presented and discussed.

Chapter 7 provides recommendations regarding further use of the mini-beam collimator. Finally, a recommended characterization and QA procedure for the mini-beam collimator is presented.

CHAPTER 2

IONIZING RADIATION

Radiation is simply defined as emitted energy [24]. It can be in the form of energetic sub-atomic particles, atoms, or photons. Properly used, radiation can be a powerful tool in medicine. The effective use of radiation demands a sound knowledge of the underlying physics. This chapter will discuss ionizing radiation and its interactions with matter as they relate to radiation oncology.

Radiation is categorized by the nature of its interactions with a medium. A clear division is between ionizing and non-ionizing radiation. This distinction is based on the energy of the radiation. Ionizing radiation is able to free atomic electrons from the atom, releasing them as free electrons and leaving behind an ion, a charged atom.

In order to ionize an atom, sufficient energy must be delivered to overcome the energy of the bond between the electron and the nucleus, called the ionization or binding energy (E_B). Non-ionizing radiation does not have sufficient energy to free electrons from an atom. Excitation via interaction is possible, but the electron remains bound to the nucleus. The selection of a dividing line is complicated by the range of ionization energies for different atoms, but a threshold of 10 eV is considered adequate for radiobiological applications [24, 25].

Ionizing radiation can be further divided by the means of energy transfer to the medium. The two types are directly-ionizing radiation and indirectly-ionizing radiation.

2.1. Directly Ionizing Radiation

Directly-ionizing radiation consists of energetic charged particles (e.g. electrons or protons) which deposit energy via Coulomb interactions with the atoms of the medium. Electron interactions with the atoms of the medium are a key mechanism of energy deposition for all radiation therapy treatment modalities.

2.1.1. Coulomb Interactions

The mechanism by which charged particles transfer energy to atoms in the medium is based on Coulomb's Law, which describes the force exerted by charged bodies on one another:

$$\mathbf{F}_{Coul} = \frac{qq'}{4\pi\epsilon_0 r^2} \hat{\mathbf{r}}, \quad (2.1)$$

where \mathbf{F}_{Coul} is the force on the charge q due to charge q' , r is the position of charge q relative to charge q' , and ϵ_0 is the permittivity of free space [26].

The energy E required to move a charged particle against this force is found by integrating Equation 2.1 over the path of the particle. Therefore, the energy lost by a particle of charge q moving from an arbitrarily large distance to a distance r from a particle of charge q' is:

$$E = \frac{q}{4\pi\epsilon_0} * \frac{q'}{r}. \quad (2.2)$$

All energy lost by the moving particle is transferred to the electric field between the particles [26]. If the second particle was an atomic electron, it may be excited or ejected from the atom when the energy in the field exceeds its excitation or ionization energy, respectively. The moving particle is accelerated in a new direction by the Coulomb force, accounting for any energy not absorbed by the other particle.

Since the Coulomb force between charged particles is exerted at range, electrons lose energy in this manner at all times in the medium. Furthermore, they are deflected by the interactions, resulting in a highly erratic path. The trajectory of the interacting particles before and after the interaction are constrained by conservation of momentum such that:

$$\sum (m\mathbf{v})_{initial} = \sum (m\mathbf{v})_{final} \quad (2.3)$$

and

$$(m\mathbf{v})_{initial} = \sum_j^n m_j v_j \cos \theta_j, \quad (2.4)$$

where m is the mass of the particle, \mathbf{v} is the velocity of the particle, and θ is the angle between the trajectory of the incident particle and that of the emitted particle [24]. Most interactions involve only two particles, so momentum conservation may be described by:

$$(m\mathbf{v})_{initial} = m_1 v_1 \cos \theta + m_2 v_2 \cos \phi, \quad (2.5)$$

where θ is the scattering angle of the incident particle and ϕ is the emission angle of the resultant particle. In some interactions, particularly those with much more massive particles, (e.g. nuclei) the momentum lost by the electron will not be fully transferred to the other particle in the interaction. In this event, the electron will emit Bremsstrahlung photons opposite the new trajectory of the scattered electron in order to conserve momentum.

It is clear from Equations 2.3 – 2.5 that interactions between free and atomic electrons result in significant scattering, since the two electrons are of equal mass, and substantial changes in velocity must result if an atomic electron is freed. Conversely, if the interaction is between an electron and a nucleus, the energy transfer causes negligible acceleration of the nucleus and only scatters the electron, due to the significant difference in mass.

2.1.2. Classification of Electron Interactions

The type of interaction which takes place depends upon the impact parameter, b , the separation of the trajectory of the free electron and the central axis of the nucleus. The size of b relative to the atomic radius, a , determines which particles interact and how much energy is transferred in the interaction. Figure 2.1 depicts the three possible electron interactions.

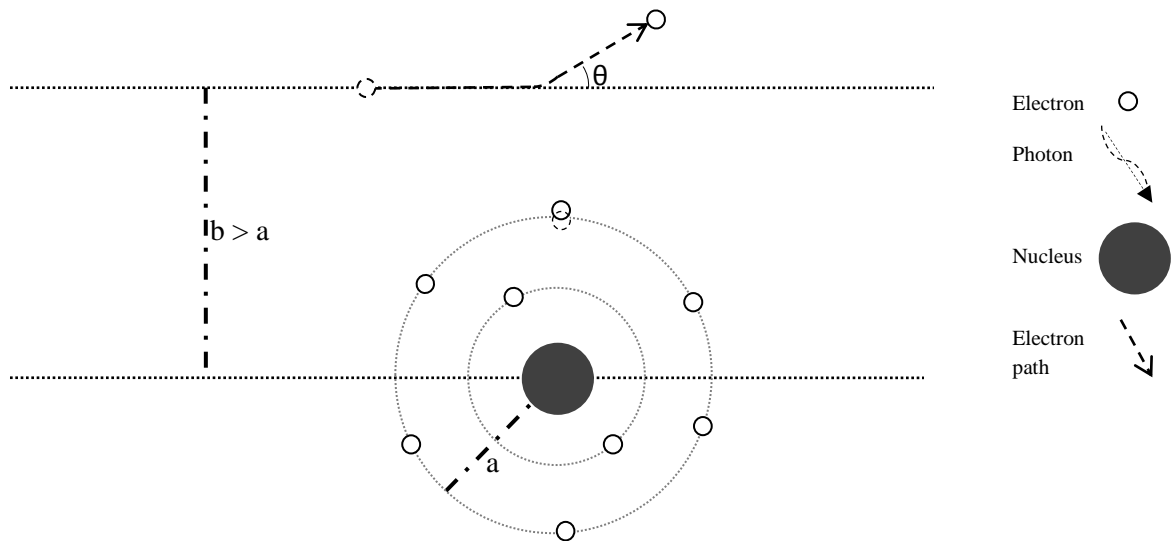
If $b > a$, a soft collision between the free electron and an atomic electron occurs. Soft collisions transfer only a small amount of energy, often less than the amount necessary to free the atomic electron, and occur constantly in a medium [27].

If $b \approx a$, a hard collision between the free electron and an atomic electron occurs. These are direct collisions, resulting in much of the free electron's energy being transferred to the atomic electron. Hard collisions are highly likely to eject the atomic electron as a delta particle. Despite occurring far less often than soft collisions, hard collisions transfer approximately half of the energy lost by the electron [27].

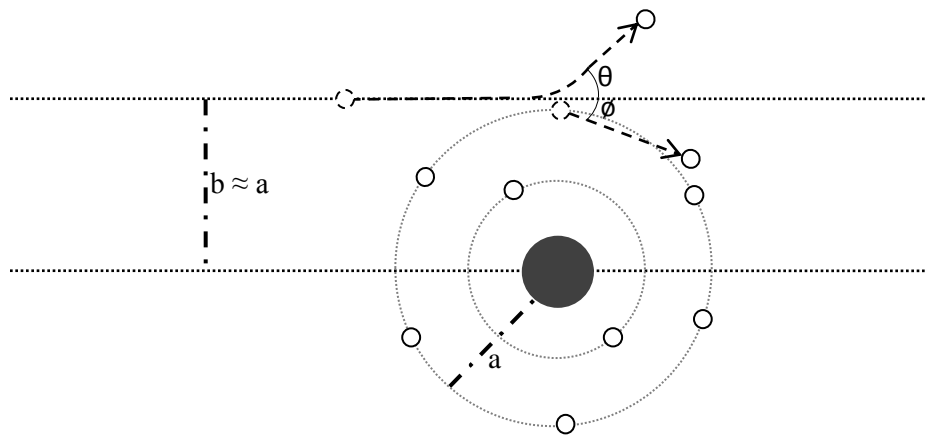
If $b \ll a$, a radiative interaction between the free electron and an atomic nucleus occurs. The electron scatters off the nucleus, changing its trajectory, while almost no effect on the nucleus can be observed. The majority of radiative interactions are fully elastic, only resulting in a change in the free electron's trajectory. Non-elastic interactions release Bremsstrahlung photons. The energy of the photon is inversely proportional to the impact parameter [24].

2.1.3. Stopping Power

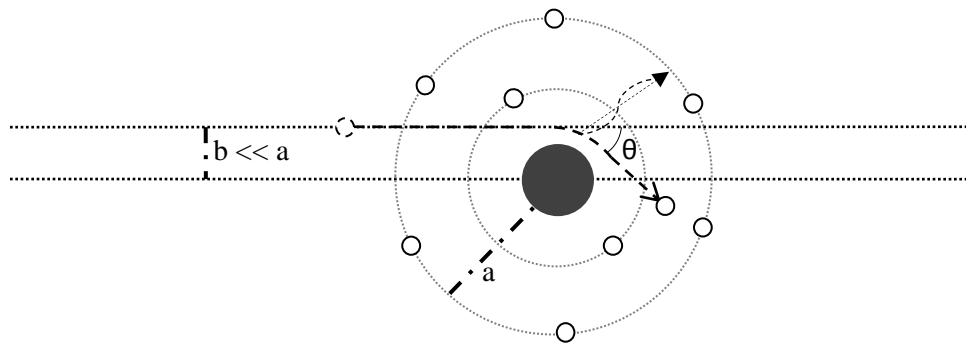
The rate of energy deposition in a medium by electron interactions can be characterized by the stopping power. Stopping power is defined as the rate of energy lost, dE , per path length, dl . It can be expressed in terms of distance travelled, giving the linear stopping power, S :



(i) Soft collision. The free electron is scattered, while an atomic electron is excited.



(ii) Hard collision. The free electron is scattered, while an atomic electron is ejected.



(iii) Inelastic radiative interaction. The electron is scattered off of the nucleus, releasing a Bremsstrahlung photon to conserve momentum.

Figure 2.1. Bohr representation of the three Coulomb electron-atom interactions.

$$S = -\frac{dE}{dl} \left[\frac{\text{MeV}}{\text{cm}} \right], \quad (2.6)$$

or in terms of the mass thickness, giving the mass stopping power, $\frac{S}{\rho}$ [29]:

$$\frac{S}{\rho} = -\frac{1}{\rho} \frac{dE}{dl} \left[\frac{\text{MeV} \cdot \text{cm}^2}{\text{g}} \right]. \quad (2.7)$$

The total stopping power consists of two terms which correspond to collisional, S_{col} , and radiative, S_{rad} , interactions. S_{col} can be further divided into terms for hard and soft collisions, such that the total stopping power is given by:

$$S_{tot} = S_{col}^{hard} + S_{col}^{soft} + S_{rad}, \quad (2.8)$$

Generally, the collisional term predominates for low energy particles, and the radiative term predominates for higher energy particles. The threshold for this transition is approximately $\frac{800}{Z}$ MeV [24].

The linear energy transfer (LET or L_{Δ}), of a radiation beam is a restricted form of the linear stopping power. LET is defined as the energy lost due to interactions which emit particles of energy less than a threshold (Δ) per unit length [3], and written as:

$$L_{\Delta} = \left(\frac{dE}{dl} \right)_{\Delta}. \quad (2.9)$$

Δ serves to define the stopping power in terms of interactions which emit secondary particles which will deposit energy within a given distance from the interaction. The size of this region is proportional to the threshold, which is selected to define a pertinent region of interest. This is of particular interest when considering biological effects. High-LET radiation will deposit a great deal of energy in a small area, such as a cell nucleus. This has been shown to increase the probability of severely damaging a DNA strand, greatly increasing the probability of cell death relative to low-LET radiation [1].

2.2. Indirectly-Ionizing Radiation

Indirectly-ionizing radiation consists of neutral particles (e.g. photons and neutrons). Energy from indirectly-ionizing radiation is deposited via a two step process. First, the incident neutral particles interact with the atoms of the medium, freeing atomic electrons. These freed electrons then deposit energy in the medium via Coulomb interactions, as previously described.

A key difference between indirectly-ionizing and directly-ionizing radiation is that while directly ionizing radiation undergoes constant interactions in the medium, indirectly-ionizing radiation interacts with the medium only through direct and discrete interactions with atomic electrons. Thus, the intensity (I) of an indirectly-ionizing radiation beam at distance d from the surface of medium is described by the attenuation relation:

$$I(d) = I_0 e^{-\mu d}, \quad (2.10)$$

where μ is the linear attenuation coefficient [cm^{-1}]. The linear attenuation coefficient is a medium dependent quantity which describes the rate of energy loss due to interactions per unit length [24]. Specific attenuation coefficients exist for the particular interactions: the photoelectric coefficient (τ) the Compton/Rayleigh scattering coefficients (σ) and the pair/triplet production coefficients (κ). Thus, the total attenuation relates to the attenuation coefficients of each interaction such that:

$$\mu = \tau + \sigma_C + \sigma_R + \kappa_{PP} + \kappa_{TP} \text{ [cm}^{-1}\text{]}. \quad (2.11)$$

Like stopping power, the linear attenuation coefficient can also be expressed in terms of mass, leading to the mass attenuation coefficient:

$$\mu_m = \frac{\mu}{\rho} = \frac{\tau}{\rho} + \frac{\sigma_C}{\rho} + \frac{\sigma_R}{\rho} + \frac{\kappa_{PP}}{\rho} + \frac{\kappa_{TP}}{\rho} \left[\frac{\text{cm}^2}{\text{g}} \right]. \quad (2.12)$$

The linear attenuation coefficient can also be expressed as a cross section per electron, $_{e}\mu$, by:

$${}_e\mu = \frac{\mu}{n} [\text{cm}^2] \quad (2.13)$$

and per atom, ${}_a\mu$, by:

$${}_a\mu = \frac{\mu Z}{n} = Z {}_e\mu [\text{cm}^2], \quad (2.14)$$

where n is the number density of the particle and Z is the atomic number of the atom.

These cross sections represent the probability of the interaction occurring as the apparent size of the target to the photon. The interaction cross sections, ${}_e\tau$ or ${}_a\tau$ for photoelectric interactions, ${}_e\sigma$ or ${}_a\sigma$ for Compton and Rayleigh scattering, and ${}_e\kappa$ or ${}_a\kappa$ for pair and triplet production, all contribute to the total interaction cross sections in the same way as the linear attenuation coefficients described in Equations 2.11 – 2.12 [24].

Figure 2.2 depicts the relative interaction cross section for the photoelectric effect, scattering, and pair/triplet production. The cross section for each interaction depends on the energy of the photon ($E = h\nu$), resulting in different interactions predominating in different energy regions. In this way, all of the interactions contribute to the attenuation of the photon.

2.2.1. Photoelectric Interactions

For low energy photons, the photoelectric effect is the dominant interaction. Photoelectric interactions are the total absorption of the photon by a tightly-bound electron ($h\nu \approx E_B$). Conservation of energy and momentum require a third particle be present in the interaction to absorb recoil, hence the requirement that the electron be tightly bound [30]. Ionizing photoelectric interactions result in the emission of an electron with energy:

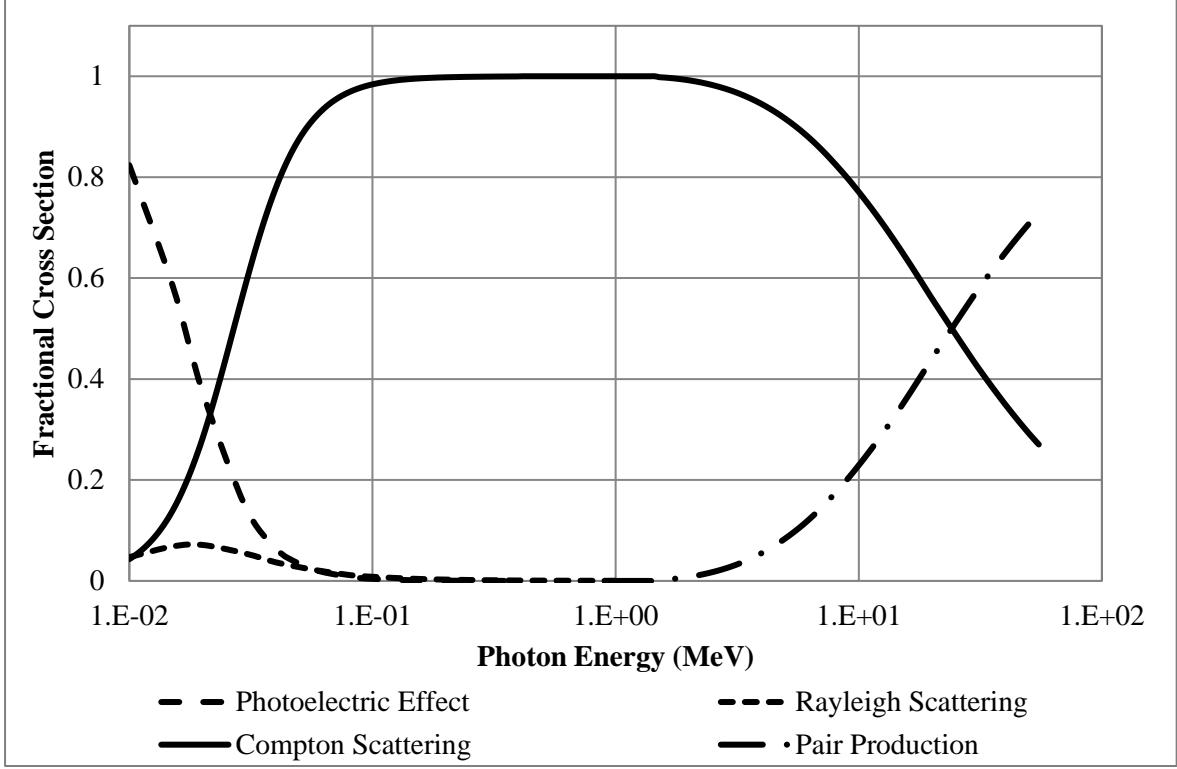
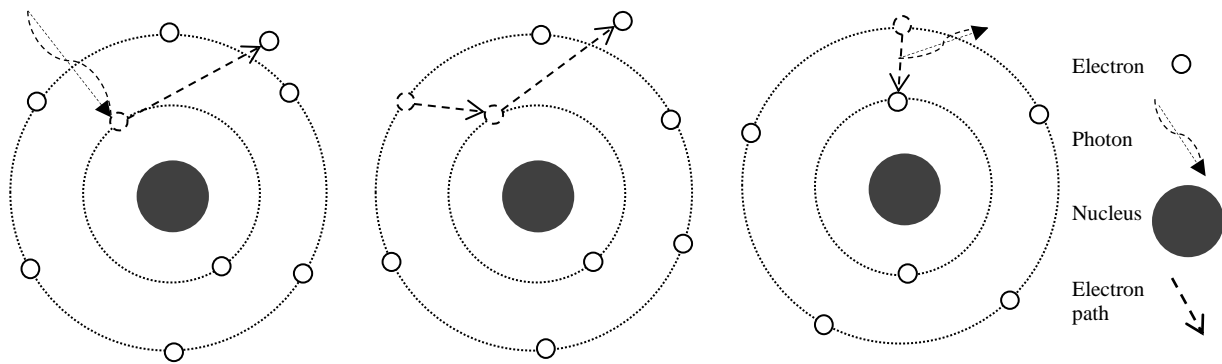


Figure 2.2. Plot of relative photon interaction cross sections for water [28].

$$E_e = h\nu - E_B. \quad (2.15)$$

Tightly-bound electrons tend to occupy low energy states. When they are emitted via ionization, a vacancy is produced, which will then be filled by a higher energy electron. If the energy difference between the two states is larger than the lower state’s new ionization potential, the second electron will also be freed, becoming an “Auger electron.”

The process will repeat until the binding energy is higher than the energy difference, in which case the excess energy is released as a fluorescent photon. The total energy released by this “cascade” is equal to the energy of the initial photon [24]. A photoelectric interaction and subsequent Auger cascade are depicted in Figure 2.3.



(i) Photoelectric absorption (ii) Auger electron emission (iii) Fluorescent photon emission

Figure 2.3. Bohr representation of a photoelectric interaction and Auger cascade.

The photoelectrons are emitted at an angle (ϕ) off of the incident photon's trajectory. ϕ is non-deterministic, and is treated as a distribution of possible angles. The width and mean of the distribution are inversely proportional to the incident photon energy.

The cross section for photoelectric interaction with electrons, τ , generally decreases with increasing photon energy, but exhibits spikes, called absorption edges, where the likelihood of interaction abruptly increases. These edges correspond with electron shell binding energies, where total absorption is more probable. For sufficiently high energy photons, τ is effectively zero, as seen in Figure 2.2. Higher energy photons will exceed the binding energy of more electrons, making total absorption improbable.

2.2.2. Compton and Rayleigh Scattering

At high photon energies, scattering becomes the dominant photon interaction. Rayleigh scattering is the elastic collision of photons with tightly-bound electrons. As an elastic collision, the photon loses no energy, but does transfer some momentum to the electron, changing the photon

trajectory and limiting the maximum depth achievable in the medium. The scattering angle is approximated by:

$$\theta_R \cong 2\sin^{-1}\left(\frac{0.026\sqrt[3]{Z}}{\left(\frac{hv}{m_e c^2}\right)}\right). \quad (2.16)$$

Rayleigh scattering generally occurs at lower photon energies and higher atomic numbers than Compton scattering [24].

Compton scattering is an inelastic collision between a photon and a loosely-bound ($E_B \ll hv$) electron, resulting in the emission of a scattered photon and a recoil electron. The energy of the scattered photon is given by:

$$hv' = \frac{hv_o}{1 + \frac{hv_o}{m_e c^2} (1 - \cos\theta)}, \quad (2.17)$$

where v' is the post scattering frequency of the photon, v_o is the pre-scattering frequency of the photon, and θ is the scattering angle [31]. Thus, the resultant energy of the recoil electron is:

$$E_e = hv_o - hv' - E_B. \quad (2.18)$$

Since Compton scattering must occur with loosely bound electrons, E_B is small, and can be approximated as equal to zero.

A Compton interaction is depicted in Figure 2.4. The scattering angle θ and recoil angle ϕ relate to the initial photon trajectory as described for electron-electron interactions in Equations 2.3 – 2.5. Note also that Equation 2.16 shows a proportional relationship between hv' and θ when $\theta < 90^\circ$, and does not allow for $\theta \geq 90^\circ$. The scattering angle θ and electron recoil angle ϕ from the original photon trajectory relate to momentum conservation in the same manner as described for electron-electron interactions by Equations 2.3 – 2.5.

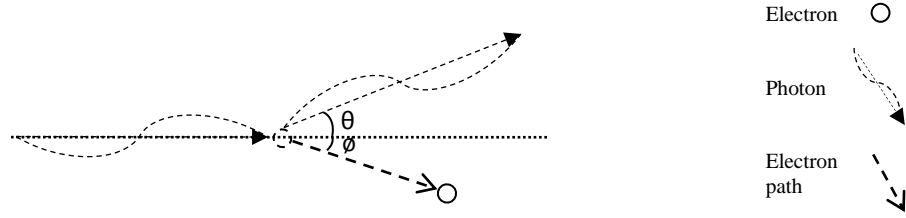


Figure 2.4. Compton scattering of a photon with a loosely bound electron. The photon is scattered at angle θ , and the electron is ejected from the atom at recoil angle ϕ .

The interaction cross section for Compton scattering with of a free electron was derived from the Dirac theory of the electron by Oskar Klein and Yoshio Nishina [32]. Klein and Nishina's formulation (σ_c^{KN}) offered a refinement of the earlier models by way of the Klein-Nishina form factor, which reduced the calculated values to be more in line with experimental observation [30]. As seen in Figure 2.2, σ_c is the dominant interaction cross section for photon energies between tens of keV and 10 MeV, dropping off outside this range. Unlike the photoelectric effect and pair production, the scattering cross sections do not drop to zero at any photon energy, though they become extremely small in very low and very high energy regimes.

2.2.3. Pair and Triplet Production

At photon energies above 1.022 MeV ($2m_e c^2$) pair production becomes possible. In pair production interactions the photon creates an electron-positron pair. Since the total momentum of the electron-positron pair is less than that of the incident photon, pair production must occur near an atom, where a third particle can absorb the excess momentum. This requirement raises the energy threshold for pair production by a factor dependent on the atomic mass (m_A), such that:

$$E_{th}^{PP} = 2m_e c^2 \left(1 + \frac{m_e c^2}{m_A c^2} \right). \quad (2.19)$$

The additional energy requirement is slight, and decreases for heavier atoms.

When the third particle in the interaction is a nucleus, the interaction results in the emission of an electron-positron pair [27]. However, when the third particle is an electron, the recoil energy resulting from the momentum transfer may result in an ionization. This is called triplet production. Only photons with energies above 2.044 MeV ($4m_e c^2$) can undergo triplet production. Since an atomic electron is ejected in triplet production an Auger cascade may result.

In pair and triplet production interactions the photon energy above the reaction threshold is transferred to the electron-positron pair, such that:

$$E_{Pair} = h\nu - 2m_e c^2 \left(1 + \frac{m_e c^2}{m_A c^2} \right) \quad (2.20)$$

and

$$E_{Triplet} = h\nu - 4m_e c^2 - E_B. \quad (2.21)$$

As with Compton scattering, E_B is generally negligible relative to the photon energy.

The energy is not transferred to the individual particles equally; any distribution of energies except 100% and 0% is possible, and no distribution is more probable than any other [24]. Both pair and triplet production are depicted in Figure 2.5. The emission angle of the electron and positron is non-deterministic and forward distributed [27].

Since the positron is an antiparticle, it annihilates on contact with an electron. In most interactions with these stopped positrons release two 511 keV photons travelling in opposing directions. However, some positrons directly collide with atomic electrons before losing all of their energy. If the atomic electron is tightly bound the excess momentum is absorbed by the

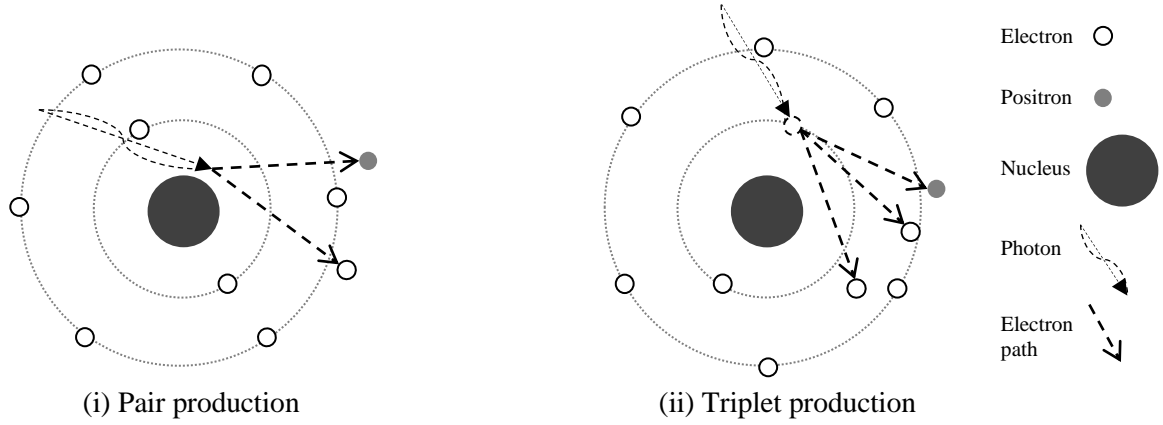


Figure 2.5. Pair production and triplet production.

nucleus, and a single photon (with $h\nu = 1.022 \text{ MeV} + E_K^{e^+}$) is emitted [24]. If the electron is loosely bound the momentum cannot be transferred to the nucleus, and is conserved by the two emitted photons, as described in Equations 2.3-2.5 [24].

The pair/triplet production cross section (σ) rises with increasing photon energy, causing pair/triplet production to become the dominant interaction at high photon energies. It is also proportional to Z^2 , meaning that pair/triplet production is more prevalent for heavier elements [30].

Photon energy is transferred to charged particles, which deposit the energy in the medium. This energy will cause the desired changes in the medium. However, as described in Chapter 1, radiation damages cells indiscriminately, meaning that careful control of the energy deposited in the target and its surroundings is crucial. A means of quantifying the energy delivered by radiation is necessary to achieve the intended outcomes.

CHAPTER 3

DOSIMETRY

As described in Chapter 2, a means of measuring the energy deposited in a medium by radiation is crucial for use in medical applications. Dosimetry serves this purpose.

This chapter will give an overview of dosimetry as it relates to radiation therapy. The quantities of interest will be introduced, as will the theoretical basis for the use of dosimeters. This will be followed with a brief overview of several varieties of dosimeters and the methods of operation. Finally, the chapter will conclude with a description of dosimetric characterization of medical linear accelerator generated radiation beams.

3.1. Dosimetric Quantities

Dosimetry is the measurement of the energy deposited in a medium by radiation. Several related quantities are used in the characterization process.

3.1.1. Fluence

In dosimetry, both particle and energy fluence are considered. Particle fluence is defined as the number of particles (dN) incident upon a cross-section normal to the path of the beam (dA) such that:

$$\Phi = \frac{dN}{dA} [m^{-2}]. \quad (3.1)$$

Energy fluence is defined as the amount of energy (dE) incident upon a cross-section normal to the path of the beam dA :

$$\Psi = \frac{dE}{dA} \left[\frac{J}{m^2} \right]. \quad (3.2)$$

Note that particle fluence is related to energy fluence such that:

$$\Psi = E * \Phi. \quad (3.3)$$

To more accurately represent a polyenergetic radiation beam the fluence can be expressed as a spectrum in terms of energy [25]. The particle fluence spectrum (Φ_E) is defined as:

$$\Phi_E = \frac{d\Phi}{dE} \quad (3.4)$$

and the energy fluence spectrum (Ψ_E) is defined as:

$$\Psi_E = \frac{d\Psi}{dE}. \quad (3.5)$$

3.1.2. Kerma

The kinetic energy released per unit mass (kerma), is a measure of the energy transferred to secondary charged particles by indirectly ionizing radiation. Kerma is defined as:

$$K = \frac{dE_{tr}}{dm} \left[\frac{J}{kg} \right]. \quad (3.6)$$

where E_{tr} is the energy transferred [25]. Kerma is measured in Gray (Gy), a derived unit defined in the International System of Units (SI) as Joules per kilogram.

As the resulting energy of the charged particles is the feature of interest in kerma, it is often more useful to ignore energy losses and consider only the energy which is immediately transferred to the medium. Collisional kerma (K_{col}) accounts for the energy transferred to charged particles

via photoelectric and scattering interactions, while ignoring the energy lost by the charged particles via Bremsstrahlung emission. It is defined as:

$$K_{col} = K(1 - g), \quad (3.7)$$

where g is the radiative fraction, the percentage of the total energy transferred to charged particles which is subsequently emitted via Bremsstrahlung radiation [25].

Kerma is related to energy fluence by the attenuation coefficient (Equation 2.12) such that:

$$K_{col} = \Psi * \mu_m = \int_0^{E_{max}} dE (\Psi_E) * \mu_m. \quad (3.8)$$

For polyenergetic radiation beams, it is necessary to integrate Ψ_E over the full range of energies to find the energy released by a polyenergetic photon beam [3].

3.1.3. Absorbed Dose

Absorbed dose is the energy imparted to the medium by charged particles per unit mass and is defined as:

$$D = \frac{d\bar{E}}{dm} \left[\frac{J}{kg} \right], \quad (3.9)$$

where $d\bar{E}$ is the average energy deposited in the volume of mass dm . Energy converted to mass via pair-production is not considered absorbed, and is not included in the definition. Like kerma, absorbed dose is measured in Gy [29].

Dose is related to electron fluence by the mass stopping power (Equation 2.7) such that:

$$D = \Phi * \left(\frac{S_{col}}{\rho} \right) = \int_0^{E_{max}} dE (\Phi_E) * \left(\frac{S_{col}}{\rho} \right). \quad (3.10)$$

Note that this relation only holds where the range of Bremsstrahlung photons in the medium is much greater than the range of the secondary electrons [3]. This requirement exists to ensure that

the electron fluence incident upon the region of interest is the only mechanism for energy deposition.

The distinction between dose and kerma arises because the charged particles freed by photons will travel some distance before depositing a non-negligible amount of energy, potentially leaving the region of interest. Thus, the energy transferred to charged particles will not be entirely absorbed by the medium in the vicinity of the energy transfer. This effect necessitates a “dose-buildup” region when using high energy (>300 kV) indirectly ionizing radiation [33].

3.1.4. Charged Particle Equilibrium

The spatial separation between energy transfer to charged particles and energy deposition in the medium leads to an effect called charged particle equilibrium, where the energy entering and leaving a volume in the form of charged particles is equal.

When a photon beam is incident upon a medium, such as water, collisional kerma is highest at the surface. At the surface, photon energy fluence is at its peak in the medium, and both Ψ and K_{coll} decrease with depth [3]. Thus, the largest number of electrons is freed at the surface. Similarly, they will have the greatest average energy of the electrons freed at any depth. The freed electrons will travel a short distance in the water, depositing energy along the path. At a depth approximately equal to the average range of the electrons freed at the surface the energy deposited reaches a peak. This depth is called d_{max} , the depth of maximum dose. Past d_{max} the dose decreases with depth, as more energy is deposited by delta electrons than is freed by photons to deposit energy at greater depth. A plot of D and K_{coll} against depth for an ideal photon beam is shown in Figure 3.1.

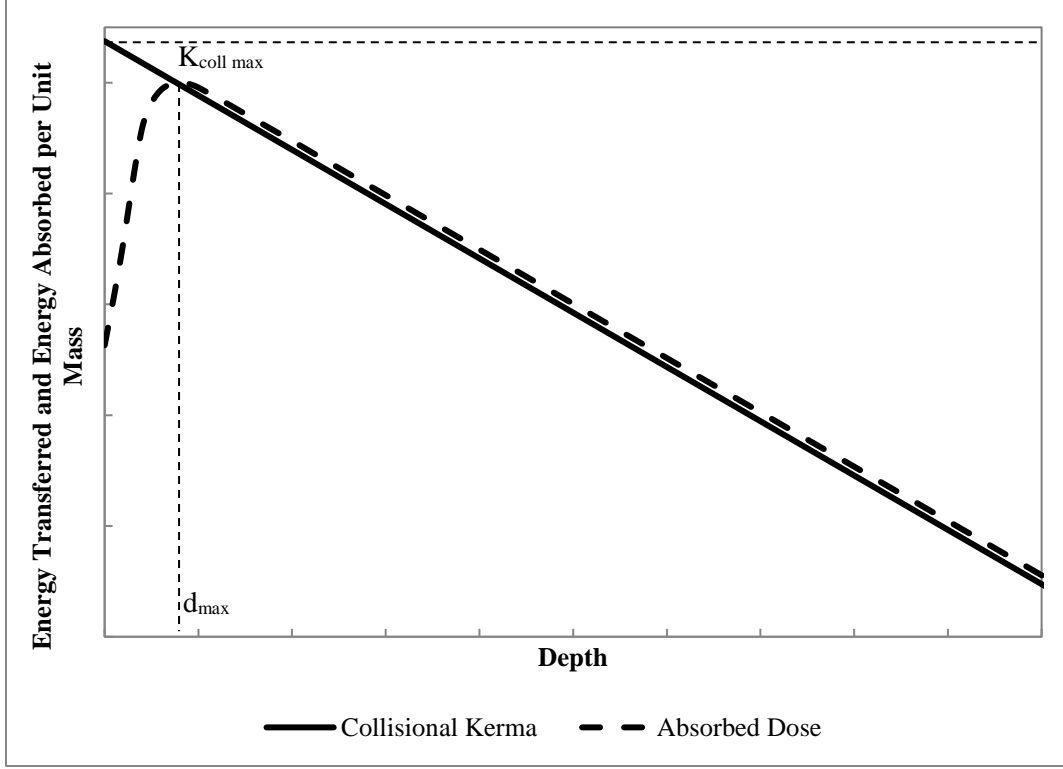


Figure 3.1. Depth dose and K_{coll} for an ideal photon beam.

The condition of true charged particle equilibrium is met only at the depth of peak dose (d_{max}). However, a related condition called transient charged particle equilibrium is said to exist at depths greater than d_{max} where the rate of change in K_{coll} is approximately equal to the rate of change in dose [35].

3.2. Cavity Theory

Thus far, descriptions have been given for a homogenous medium under irradiation. To account for the effects of transitions between media, a method of correlating doses between regions with different stopping powers and attenuations is necessary.

Consider a medium A containing a region B with different stopping power and attenuation coefficients. The dose to a point in region B is known, but the dose to the equivalent point in

region A is not. The ratio $(s_{A,B})$ of the predicted dose to the same volume within a homogenous region A and the dose to region B follows from Equation 3.10 such that:

$$s_{A,B} = \frac{D_A}{D_B} = \frac{\Phi_A * \left(\frac{S_{col}}{\rho}\right)_A}{\Phi_B * \left(\frac{S_{col}}{\rho}\right)_B} = \frac{\int_0^{E_{max}} dE (\Phi_E)_A * \left(\frac{S_{col}}{\rho}\right)_A}{\int_0^{E_{max}} dE (\Phi_E)_B * \left(\frac{S_{col}}{\rho}\right)_B}. \quad (3.11)$$

This relationship is the basis of cavity theory. A “cavity” is simply a volume of some material within a medium composed of a different material (e.g. region B in the above example), as depicted in Figure 3.2. Cavities are described by their size relative to the path length of the secondary particles being considered. Small cavities are those smaller than the average path length. They tend to have a minimal effect on particle fluence, and it is assumed that all absorbed dose in the cavity was deposited by particles produced outside the cavity [3]. As a result, many detectors are considered “small” when used with high energy beams, but this condition is difficult to achieve for low energy beams [36]. Large cavities are larger in all dimensions than the average path length of secondary particles. Under this condition, it is assumed that all dose to the cavity was deposited by particles produced within the cavity [3]. While conceptually convenient for dose calculations, large cavities have a significant effect on the radiation fluence, and necessarily have poor spatial resolution. These considerations led to the formulation of several models for considering small cavities. The Bragg-Gray [37] and Spencer-Attix [38] formulations for small cavities are notable.

Bragg-Gray cavity theory assumes that the cavity is sufficiently small to cause no observable change in particle fluence. In this case, Equation 3.11 becomes:

$$s_{A,B} = \frac{\int_0^{E_{max}} dE \left(\frac{S_{col}}{\rho}\right)_A}{\int_0^{E_{max}} dE \left(\frac{S_{col}}{\rho}\right)_B}. \quad (3.12)$$

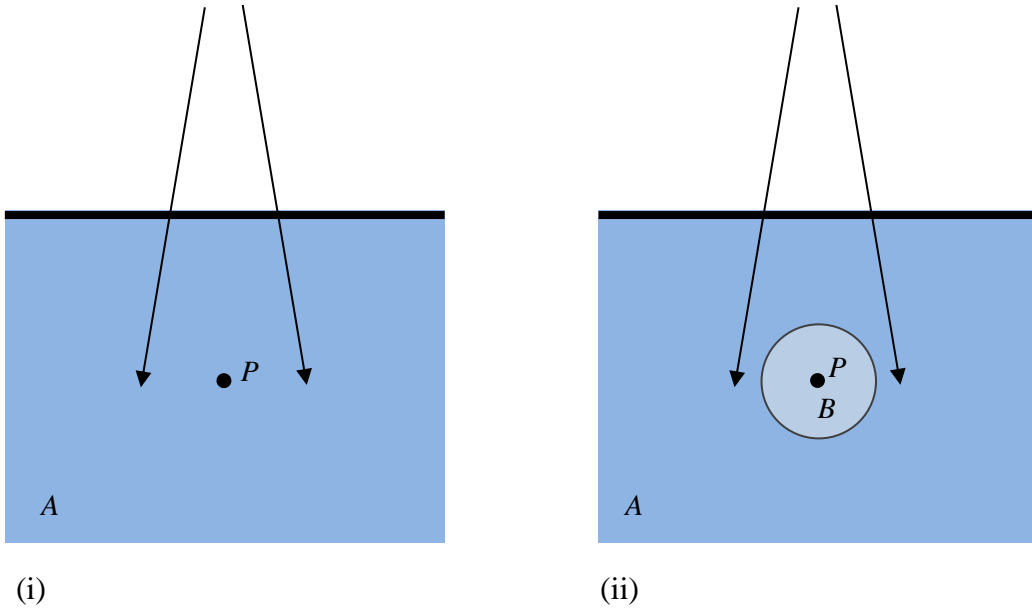


Figure 3.2. A dosimeter inserted into a uniform medium A under irradiation by a photon beam. (i) shows the homogenous medium, with the point of interest P labelled. (ii) shows the medium with a cavity B of another material inserted around point P . Cavity theory must be used to account for the impact of the cavity on the dose to P .

Spencer-Attix cavity theory extends the Bragg-Gray model to account for the production of delta particles in the cavity. As any delta particles with sufficient energy will exit the cavity without depositing the freed energy, the Spencer-Attix formulation uses the restricted stopping power, described in Chapter 2, to limit the interactions considered to those which deposit their energy within the cavity. Any delta particles with energy above Δ are treated as part of the electron fluence spectrum [30]. With this adjustment, Equation 3.12 becomes:

$$S_{A,B} = \frac{\int_{\Delta}^{E_{max}} dE (\Phi_E)_A * \left(\frac{L_{\Delta}}{\rho}\right)_A + (\Phi_E(\Delta))_A \left(\frac{S_{col}}{\rho}(\Delta)\right)_A \Delta}{\int_{\Delta}^{E_{max}} dE (\Phi_E)_B * \left(\frac{L_{\Delta}}{\rho}\right)_B + (\Phi_E(\Delta))_B \left(\frac{S_{col}}{\rho}(\Delta)\right)_B \Delta}. \quad (3.13)$$

3.3. Dosimeters

The application of cavity theory allows the use of dosimeters to rigorously measure dose to media. By definition, a dosimeter is any device with a measurable quantity which correlates to a quantity of radiation [35]. This definition is as broad as it sounds, and many varieties of dosimeter exist. Different types of dosimeter are suitable for different applications. For example, calorimeters offer a direct measurement of the energy deposited, but are difficult to use. As a result, they are limited to use in primary standards labs. Less demanding devices, such as ionization chambers or diode detectors, are commonly used for clinical dosimetry of radiation beams.

To ensure accuracy in the result, the measured signal M_{raw} must be corrected. Corrections to the measured signal for environmental conditions, electron-ion recombination within the detector, and signal losses within the measurement apparatus exist for most detectors. The exact corrections necessary depend on the type of detector and measurement.

Generally, the dose D to a point in the medium can be determined from the corrected detector response M and the absorbed dose to the detector dose \bar{D}_{det} via:

$$D = \frac{M}{\left(\frac{M}{\bar{D}_{det}}\right)} * S_{med,det} \quad (3.14)$$

The ratio $\frac{M}{\bar{D}_{det}}$ is the detector response, which is determined by relation to a primary standard. Correction factors are applied to $S_{med,det}$ to account for effects neglected in the ideal case (e.g. energy deposited by electrons generated within a Spencer-Attix cavity) [35].

3.3.1. Ionization Chambers

Ionization chambers are a common form of dosimeter. They consist of a gas filled cavity containing an anode and cathode. This cavity is known as the active volume of the detector, and is the region in which energy deposition is measured. Ionizing radiation produces electron-ion pairs in the gas, which are accelerated by the electric field between the electrodes. The charge collected by the electrodes is correlated to the dose. Ionization chambers are very well established measuring devices, being the standard for clinical reference dosimetry in radiation oncology [39].

3.3.2. Diode Detectors

The active volume of a diode detector is the depletion region of a silicon p-n junction. An electric field is produced in this region by the buildup of excess electrons on one side and the absence of electrons on the other. Any atomic electron freed from the silicon crystal in this region will be accelerated to one side by the electric field while the resulting “hole” will be filled by an electron from up-field, causing the hole to appear to move with the electric field. The charge collected at the ends of the junction is correlated to dose in a similar manner to ionization chambers. Though not used in reference dosimetry, diodes are known to have a good energy response and excellent spatial resolution, and remain useful for other clinical applications, particularly small field dosimetry [40].

3.4. Dosimetric Measurements

Dosimetric characterization focuses on particular features of the beam. This focus defines the beam in terms of easily quantified features, ensuring the accuracy of comparisons without excessive complexity. Percent-depth dose curves, dose profiles, and point dose measurements are

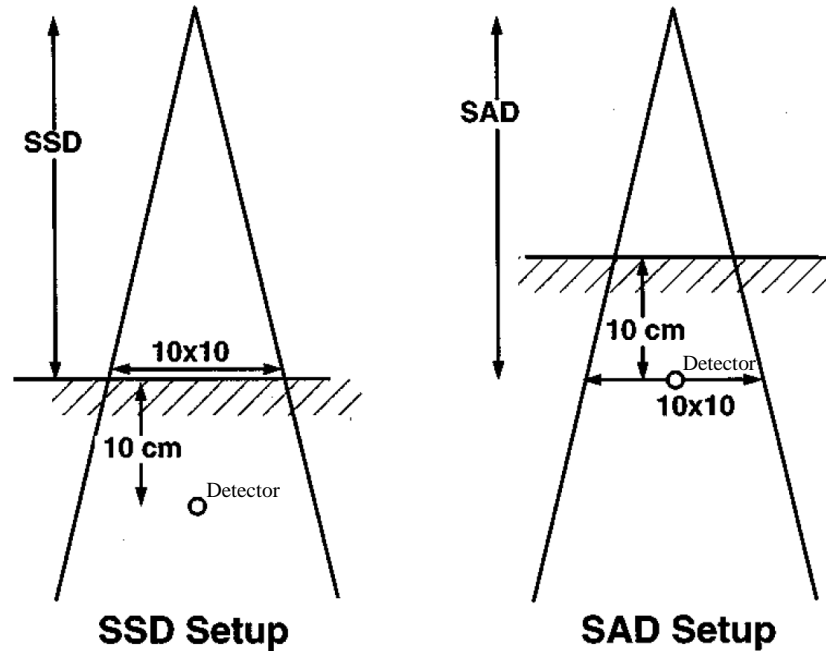


Figure 3.3. Detector setup and field size definitions. Source-surface distance (SSD) and source-axis distance (SAD) are shown. Image from Almond *et al.* 1999 [34], used with permission.

used to characterize radiation beams used in radiotherapy.

The source used to generate the radiation beam will influence the measurements. ^{60}Co sources are used as a reference for radiation dosimetry because they have a constant and universal photon energy. Measurements of any other source (e.g. linac or synchrotron-generated beams) are referenced to ^{60}Co for dose calculations [34].

To ensure consistency, the measurement medium must be positioned at a set distance from the source for all measurements. This may be defined by the source-to-surface distance (SSD), the distance from the beam source to the medium surface, or the source-to-axis distance (SAD), the distance from the source to the dosimetric reference point. These configurations are shown in Figure 3.3. It is recommended that measurements of high energy photon beams be performed in water [34]. Water provides a dose buildup region which allows the detector to be repositioned freely, and its interactions with ionizing radiation are well known. Furthermore, for medical

applications, humans are considered to be nearly water-equivalent, since soft tissue consists mainly of water and the differences are generally too small to be observed [35]. Low energy photon beams are instead characterized by air-kerma measurements, since water attenuates the beam by too great an extent for dose at depth to be an informative measure [41]. Two categories of clinical dosimetric measurements exist: reference dosimetry and relative dosimetry.

3.4.1. Reference Dosimetry

Reference dosimetry serves to establish the baseline output of a radiation source. It is performed at the time of commissioning, and updated periodically thereafter. Reference dosimetry makes use of percent depth dose measurements and single point measurements to formally establish the output of a radiation beam and reference it to a national standard.

3.4.1.1. Beam Quality

Beam quality (Q) is a factor which depends on the energy spectrum of the beam, which serves to relate an MV photon beam to a ^{60}Co source [34]. It is used to trace dosimetric measurements back to a national standard to ensure consistency in reported values. The beam quality is defined using percent depth dose, described in Section 3.4.2.1. The American Association of Physicists in Medicine (AAPM) recommend that the percentage of the maximum dose at 10 cm depth in water be used to specify beam quality. An alternate formalism published by the International Atomic Energy Agency (IAEA) uses the tissue-phantom ratio, the ratio of doses at 20 cm and 10 cm depth, for the same purpose [42]. The two methods were shown to specify beam qualities which agree to within $\pm 2\%$ for high energy photon beams, so either formalism may be used in reference dosimetry [43].

3.4.1.2. Point Dose

Point dose measurements record the energy absorbed by a region at a reference location. Point dose measurements are extremely important in radiation oncology, being crucial for treatment planning.

Measurements of absolute point dose are necessary to quantify the output of the radiation beam. Reference dosimetry is the procedure used to set the dose to a reference point. The detector response must be converted to dose to water (D_w^Q) via:

$$D_w^Q = k_Q N_{D,w}^{^{60}\text{Co}} M, \quad (3.15)$$

where k_Q is the quality conversion factor, which converts the detector calibration factor determined by calibration with a ^{60}Co ($N_{D,w}^{^{60}\text{Co}}$) source to a value for the clinical beam [34]. With the dose to a reference point known, the beam's relative dosimetric qualities can be extrapolated.

3.4.2. Relative Dosimetry

Relative dosimetry is used to relate the dose delivered by a radiation beam for any setting back to the reference value determined by reference dosimetry. It makes use of relative measurements to determine how variations in the beam definition affect the delivered dose.

3.4.2.1. Percent Depth Dose

Since interaction cross-sections are energy dependent, and particles lose energy as they travel through matter, radiation beams can be effectively characterized by how the dose changes along the central axis of the beam. Percent depth dose (%DD) curves are a plot of dose as a function of depth normalized to d_{max} . %DD for a 6 MV photon beam is shown in Figure 3.4.

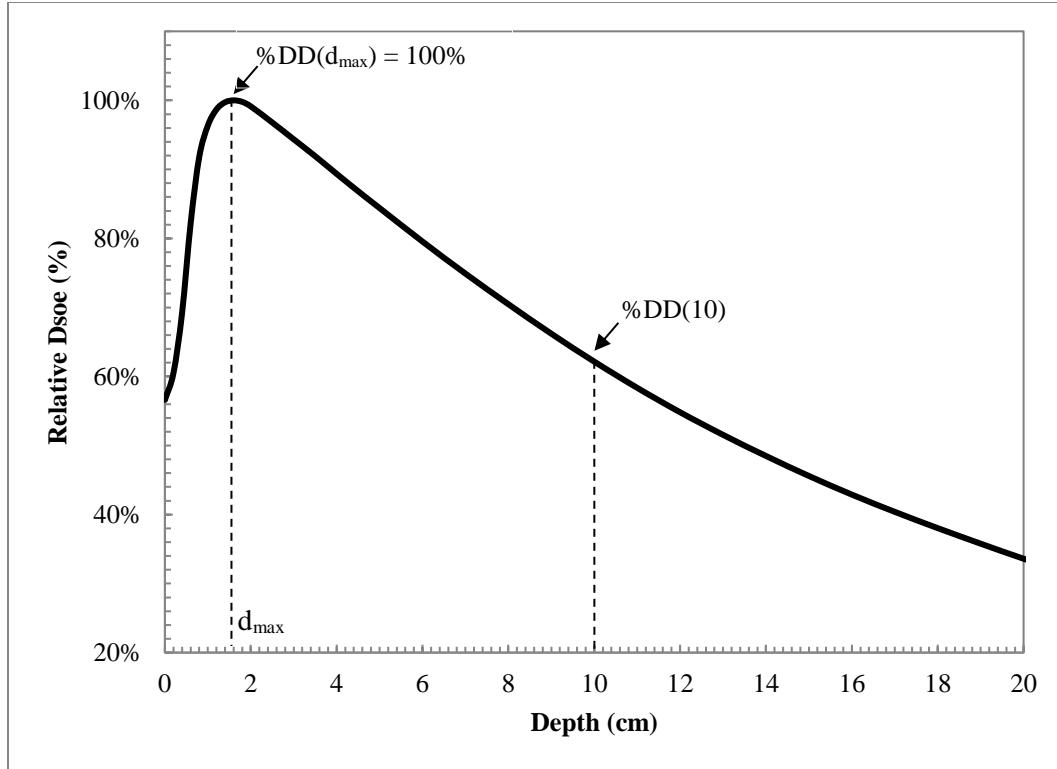


Figure 3.4. A percent depth dose curve for a 6 MV photon beam. $\%DD(d_{max})$ and $\%DD(10)$ are labelled.

The main features of interest in a percent depth dose are d_{max} and the percent dose at a depth of 10 cm ($\%DD(10)$). Recall from Section 3.1.4 that d_{max} is the location of true charged particle equilibrium. As seen in Figure 3.4, relative dose increases with depth up to d_{max} , and decreases thereafter as more electrons deposit all of their energy and stop. Obviously, the depth at which electrons can be freed, and the energy of the electrons, is proportional to the energy of the incident photons, making d_{max} a clear indicator of beam energy [35].

$\%DD(x)$, the percentage of the peak dose delivered at depth x , is defined as:

$$\%DD(x) = \frac{D(x)}{D(d_{max})}. \quad (3.16)$$

3.4.2.2. Dose Profiles

Dose profiles are a plot of the relative dose as a function of axial position at a constant depth in the medium. In the case of irregular dose distributions, such as the mini-beam collimated field, they are extremely useful for correlating the relative dose to position in the field. Figure 3.5 shows the dose profile of a 10 cm x 10 cm beam at 10 cm depth, with an SSD of 100 cm. The width of the beam is defined at the Full Width – Half Maximum (FWHM), the width of the profile at a dose level of 50%.

The central region of the field is where lateral charged particle equilibrium is observed. Due to this condition, dose is roughly constant across the central region. The penumbra is the transition region where lateral charged particle equilibrium is lost due to the jaws occluding the field. The standard penumbra definition is the region between two specified dose levels (e.g. 80% to 20%) [44]. The umbra is the region where the beam is entirely occluded by the jaws, with only a very few stray particles delivering a dose [3]. Note that the umbra spans a much wider area than the rest of the profile.

3.4.2.3. Point Dose and Relative Output Factors

In addition to the obvious utility of checking the dose delivered to a reference point, point dose measurements are also used to relate the dose delivered using different field sizes. This comparison uses relative output factors (OF), the ratio of point dose in the clinical field of interest (f_{clin}) to the point dose in a reference field (f_{ref}). Relative output factors are defined as:

$$OF_{f_{clin}}^w = \frac{D_{f_{clin}}^w}{D_{f_{ref}}^w} \quad (3.17)$$

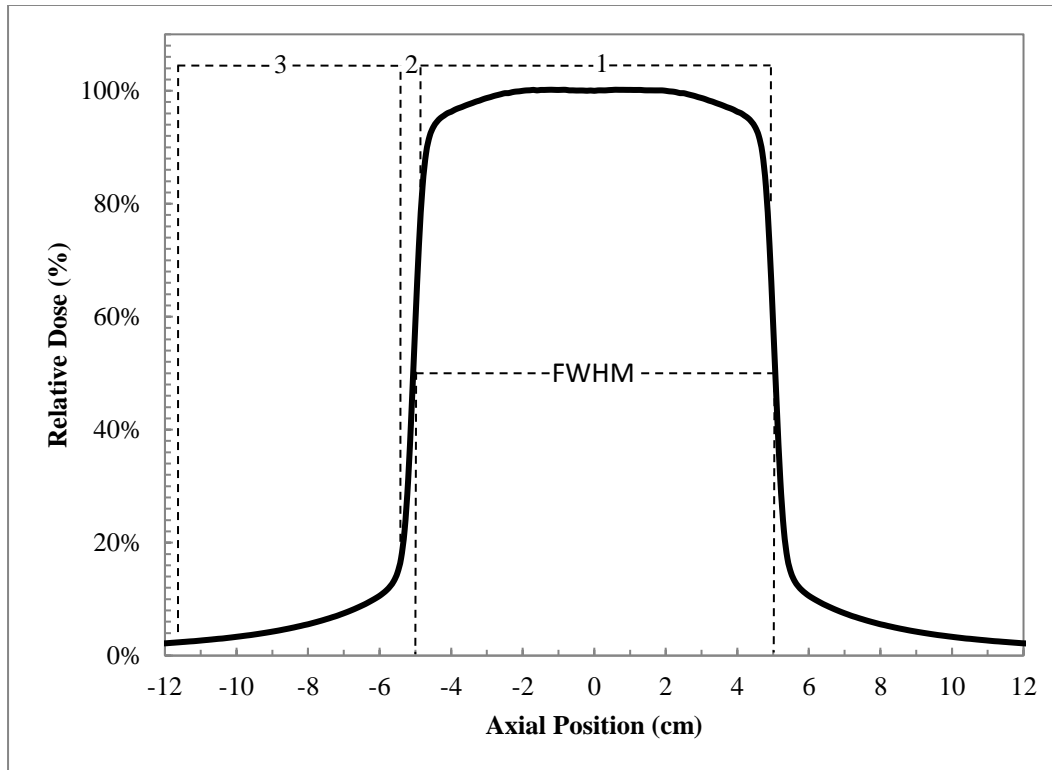


Figure 3.5. A dose profile for a 6 MV photon beam with a field size of 10 cm x 10 cm at 10 cm depth. The dose is normalized to the central axis value. The central region (1), penumbra (2), umbra (3), and FWHM are labelled.

By determining the relative output factors for a range of fields, the changes in delivered dose due to change in field can be characterized. In conjunction with characterization of how the beam energy changes with depth via the percent depth dose, the dose delivered by the beam can be predicted for a range of clinical fields.

3.5. Uncertainty Analysis

Obviously, no measurement can be perfect. All measured values possess an uncertainty, representing the range of values the quantity could reasonably be said to equal. Quantifying the

uncertainty serves to quantify the precision of the measured values and allows one to see whether or not multiple measured values are in agreement.

Uncertainties are divided into two categories: Type A and Type B. Type A uncertainty accounts for random variation between measurements. It is estimated from the standard deviation of repeated experimental trials. Given a series of N independent experimental measurements of a quantity x , such as point dose or %DD(10), the mean value:

$$\bar{x} = \frac{\sum x_i}{N}, \quad (3.18)$$

is taken to be the measured result and the 1σ Type A uncertainty (u_A) would be calculated from the variance (σ) such that:

$$u_A = \frac{\sigma(x)}{\sqrt{N}} = \sqrt{\frac{\sum (x_i - \bar{x})^2}{N(N-1)}}. \quad (3.19)$$

Since 1σ uncertainty reflects a confidence interval of only 68%, this estimate may be multiplied by a “coverage factor” corresponding to higher sigma confidence intervals. 2σ (95%) and 3σ (99.7%) are the most commonly used intervals [45]. Type B uncertainties account for any external influence that cannot be identified via statistical analysis. There are no established rules for estimating Type B uncertainty, but steps can be taken in the experimental structure to mitigate the effects. Uncertainties, being standard deviations, must be combined as the sum of the variance of each quantity [45].

Direct measurements of dose are not always feasible. For example, time or material constraints may prevent repeated experimental measurements to determine how to deliver the selected dose, or the region of interest may be inaccessible to detectors, as with a live patient. For such situations, simulations of the beam may be used.

CHAPTER 4

MONTE CARLO SIMULATION TECHNIQUES

Simulations are a valuable tool for the study of radiation. Properly validated simulations allow convenient analysis of beams, accelerators, and attachments. In medical physics, radiation beams are often simulated using Monte Carlo particle transport algorithms. Monte Carlo simulations sample probability distributions for interactions to model the path of particles in a medium. A representation of the radiation beam can be constructed by simulating the paths of many particles.

This chapter will provide a brief history of the Monte Carlo method and introduce the mechanics of Monte Carlo particle transport. Variance reduction techniques will be presented before closing with an introduction to EGSnrc³, the Monte Carlo user code employed in this study.

4.1. History of the Monte Carlo Method

The idea of using repeated randomized tests to calculate a quantity of interest dates back to 1777, when Georges-Louis Leclerc proposed a method of calculating the probability (Pr) that a needle would overlap a line on a ruled sheet of paper when tossed onto it by recording the result of repeated tosses. A century later, Pierre-Simon Laplace noted that Leclerc's result was equivalent to:

³ EGSnrc is a development of the Electron Gamma Shower 4 [46] Monte Carlo software package developed at the Stanford Linear Accelerator Center.

$$\Pr(\textit{crossing}) = \frac{2l}{\pi d}, \quad (4.1)$$

where l is the length of the needle and d is the line spacing. Laplace proposed that this result could be rearranged to calculate π via repeated tosses of the needle [47]. The accuracy of this estimation increases with the number of trials, as the fraction of tosses which cross a line converges to the actual probability. However, calculating π in this way is inefficient and tedious.

The use of results randomly sampled from a probability distribution to simulate particle transport is credited to Stanislaw Ulam and John von Neumann, who expanded an insight of Ulam's to model neutron transport in thermonuclear weapon designs. The sampling method was used to ease the theoretical calculations involved by analyzing probable outcomes from a sample of possibilities rather than performing the necessary matrix operations to rigorously track particle outcomes through a medium. In their 1949 paper, Ulam and Metropolis codified the evaluation of computationally difficult problems via the examination of many random trials, which coined the term "Monte Carlo method." This paper also advanced the idea of simulating particle transport via "chains of events," which made computation feasible [48].

4.2. Theory of the Monte Carlo Method

The Monte Carlo method is sometimes called the "method of statistical trials," since it is based on approximating quantities through repeated random events. If the probability distribution used is accurate and the number of particles tracked is sufficient, the results will converge to the actual outcome.

In order to perform Monte Carlo calculations it is necessary to generate random numbers. Truly random numbers cannot be chosen by a computer, but routines called random number generators (RNG) can generate "pseudo-random" numbers that are nearly random for the purposes

of the simulation. RNGs use an algorithm to produce a sequence of numbers which bear no apparent connection to one another. This is generally accomplished by manipulating the bits of a seed number to produce a new number. Any repeated call of an RNG will eventually restart the sequence, which is the key difference between pseudo-random and truly random numbers. An RNG suitable for Monte Carlo calculation must output a sequence of numbers which is uniformly distributed, does not repeat within the duration of a simulation, and cannot be statistically correlated [49].

For many applications where the Monte Carlo method is advantageous, evenly distributed random numbers are not sufficient. Monte Carlo algorithms must use random numbers which accurately reflect the probability distribution of each result. This is accomplished by defining a probability density function $p(x)$ such that the probability of a result with a value between a and b is:

$$\Pr(a < x < b) = \int_a^b dx p(x), \quad (4.2)$$

which reflects the probability of each interaction or result. Using such a distribution to weight an RNG output r uses the cumulative probability function:

$$G(x) = \Pr(a < x) = \int_a^x dx' p(x'), \quad (4.3)$$

where a is chosen such that $\Pr(a) = 0$ [50]. By transposing $G(x)$, the weighted random output R is found such that:

$$R = G^{-1}(r) \quad (4.4)$$

where R is distributed according to $p(x)$.

If G^{-1} cannot be determined, the rejection method must be used instead. The rejection method involves selecting a transposable comparison function g' such that $g'(x) > p(x)$ to be

used for sampling. If a random number between 0 and $g'(R)$ is less than $p(R)$, R is accepted as following $p(x)$, otherwise new numbers are selected [46].

As the results of a Monte Carlo simulation are based on N repeated measurements of a quantity, the uncertainty in the quantity of interest is given by:

$$u_{MC} = \frac{\sigma}{\sqrt{N}}, \quad (4.5)$$

just as described for repeated measurements in Chapter 3 [49].

4.3. Monte Carlo Particle Transport

Due to the many complex dependencies involved in modelling particle interactions, accurate analytic solutions are often difficult to obtain. However, the Monte Carlo method simulates particle transport as a series of interactions. The interaction and result at each event can be determined by sampling the probability distributions for the interaction cross sections and resultant particle energies and trajectories. By using the result of each interaction to set the initial conditions of the next, the state of the particle and the energy it deposits as it passes through the medium are recorded. A full particle path simulated in this manner is called a “history.” By simulating the histories of many particles, a representation of a radiation beam can be constructed. Due to the random nature of the calculations, no two simulations will produce an identical history, but the outcomes of multiple simulations of sufficiently numerous histories will produce overall results that are equivalent within the simulated uncertainties.

To define $p(x)$ for the interactions, the medium must be described. Monte Carlo programs make use of files containing geometric and cross-sectional data to model the simulated media. In some implementations, such as the EGSnrc package used in this work, the simulated media are defined by groups of three-dimensional volume elements called “voxels.” Each voxel is composed

of a single substance (e.g. air, water, bone). Monte Carlo simulations transport particles through arrangements of voxels corresponding to the structure of the radiation source and irradiated media.

At each simulated step the particle undergoes an interaction. The standard process for simulating a particle interaction is as follows:

- Determine the location of the interaction from the result of the last step.
- Select the interaction by sampling the cross-sectional data.
- Simulate the interaction to determine the resulting energy and trajectory of the particle.
- Update the “stack”, the list of particles queued for simulation and begin the next iteration.

This process is repeated for all interactions experienced by each particle in the simulation. Most Monte Carlo codes follow particles via a “last-in, first-out” scheme, where secondary particles created by an interaction are followed until they fully attenuate before the transport of the initial particle resumes [51]. The particulars of each step depend on the particle being transported.

4.3.1. Electron Transport

As described in Chapter 2, electrons experience constant Coulomb interactions rather than discrete interactions in the medium. It was not until Martin Berger’s condensed history method came into use that electron transport could be easily simulated [52]. The condensed history method treats all of the electron interactions within a medium and energy-dependent distance as a single hard interaction. In the simulation, the division between soft and hard collisions is set by an energy threshold for freed electrons and Bremsstrahlung photons. Berger described two methods for condensed histories: Class I, which groups soft and hard collisions, and Class II, which groups only the soft collisions and explicitly simulates hard collisions [51]. An example electron path and the associated condensed history path are depicted in Figure 4.1.

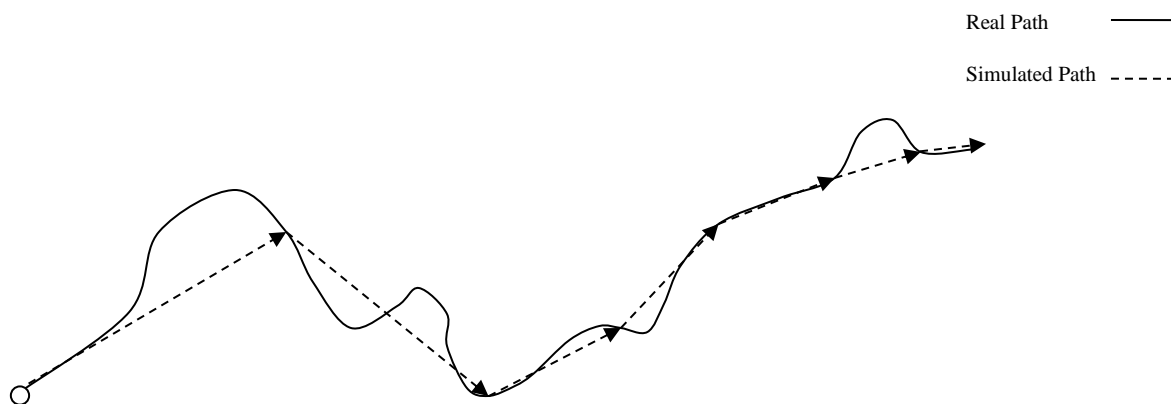


Figure 4.1. Electron path and an associated condensed history electron transport path. Secondary particle tracks are not shown.

The implementation of condensed histories used by the EGSnrc user code is summarized here as an example of the process. The electron energy at the time of the next high energy interaction is sampled from the atomic cross sections for collisional and radiative interactions. The electron energy, position, and trajectory which most closely agree with the electron transport parameters are determined based on the sampled energy. The interaction type is sampled from the relative interaction cross sections and simulated. Following the interaction the resulting particles and associated energies and trajectories are logged, and the process repeats for the next step [53].

The continuous slowing down approximation (CSDA) is used to determine the electron path lengths and describe the soft collisions which are grouped in the condensed history. CSDA assumes that the electron loses energy in a steady and predictable manner, and ignores the deflections caused by soft interactions. It determines the path length from the stopping power of the medium for the electron energy. As a result, the spatial separation between the simulated hard collisions decreases as the electron loses energy [54].

4.3.2. Photon Transport

As described in Chapter 2, photons experience discrete interactions with the medium. Thus, interactions of indirectly ionizing radiation translate naturally to the process described in Section 4.2.2. Each interaction can be treated separately, being separated in space. The distance d between two photon interactions is randomly determined from the linear attenuation coefficient for the medium via:

$$d = -\frac{\ln(1 - r)}{\mu}. \quad (4.6)$$

Upon reaching the interaction site, the photon interaction is determined by sampling the relative interaction cross sections for the photon energy. The results of the interaction are calculated in a similar fashion to electron interactions. Any secondary particles are added to the stack for future transport [51].

The EGSnrc process for simulating photon interactions is again used as an example. The interaction type, atom, and electron shell are selected by sampling the interaction cross sections. Next, the outcome of the interaction is selected. Each interaction requires a different process. If a photoelectric interaction is simulated, the resultant kinetic energy of the electron is known from the target shell's binding energy, and the electron emission angle is sampled from the angular distribution. If a Rayleigh interaction is simulated, the only quantity of interest is the emission angle, which is found by sampling the emission angle distribution. If a Compton interaction is simulated, the scattering angle of the photon is sampled from the scattering angle distribution, and used to calculate the electron recoil angle and the associated energy of each particle. If a pair production interaction is simulated, the emission angles are calculated by sampling the angular distributions, and the particle energies are calculated by sampling the energy split [53].

4.4. Variance Reduction Techniques

As described in Equation 4.5, the uncertainty in the result of a Monte Carlo simulation improves as the number of trials increases. In order to evaluate the precision of the simulation, a method of determining the uncertainty is necessary.

The uncertainty in the simulation results can be decreased by using a greater number of histories. However, since the uncertainty is inversely proportional to the square root of the number of histories, the duration of the simulation increases quadratically with the precision. This is quantified by the efficiency (ϵ) such that:

$$\epsilon = \frac{1}{|u_{MC}|^2 T}, \quad (4.7)$$

where T is the time required to simulate the number of histories.

Variance reduction techniques (VRT) are modifications to the Monte Carlo algorithms which improve the efficiency of the simulation by reducing the uncertainty without increasing the number of histories. VRTs make the regular use of Monte Carlo simulation techniques much more feasible by reducing the time required to compute a result with sufficiently low uncertainty. By the formal definition, a VRT will obtain an equivalent result for a simulation with a fixed uncertainty. However, approximate techniques which can change the result are often referred to as VRTs as well, and care must be taken to ensure that the techniques used to not influence the result [55].

4.4.1. Particle Splitting

Particle splitting involves replacing a secondary particle that would ordinarily be emitted by an interaction with multiple unique secondary particles. Each of the split particles is treated as

having an equal fraction of the total statistical weight of the initial particle [53]. Particle splitting is commonly applied to Bremsstrahlung emission, but the principle can be applied to any particle generated by an interaction (e.g. Compton emission or annihilation photons).

Particle splitting improves the uncertainty of a simulation by increasing the number of particles which pass through the medium without requiring extra histories to generate them. However, excessive splitting can lead to a large number of statistically insignificant particles being simulated. If many split particles are generated alongside non-split particles, the results of the “fat” (high statistical weight) particles will tend to suppress the results of the split particles. This will lead to an increase in simulation time without significant improvements in the uncertainty. Careful selection of the splitting number is required to maximize simulation efficiency [55].

4.4.2. Russian Roulette

Russian roulette involves randomly discarding particles at the time of their creation. Particles are selected for elimination by comparing a random number between zero and one to the survival threshold, the fraction of particles which are kept, for a given particle type. The statistical weight of all remaining particles is raised in response to discarded particles [55].

Russian roulette serves to reduce the time for the simulation by reducing the computation time necessary to achieve the desired uncertainty. It tends to have the opposite effect to particle splitting, in that fat particles can be produced, causing some outcomes to be afforded greater statistical weight than would be accurate. The survival threshold must be set appropriately to balance this possibility.

Particle splitting and Russian roulette are often used in conjunction to balance the drawbacks of each method. Particle splitting is applied to the bremsstrahlung photons to rapidly

produce a full photon spectrum while the delta particles are subjected to Russian roulette to save time on electron transport. In this case, the recommended practice is to set the survival threshold to be the reciprocal of the splitting number [56].

4.4.3. Range Rejection

Range rejection involves terminating the transport of an electron and forcing it to deposit all remaining energy in the current dose scoring region if it is not likely to leave the current region of interest. Electrons are selected by comparing the energy of the electron to a threshold called the cut-off energy, and terminating it if it is below the cut-off. The cut-off energy must be selected according to the average range of electrons in the medium, such that the majority of particles eliminated would have deposited their energy in the voxel. Failure to select an appropriate cut-off energy will introduce error into the simulation. Some Monte Carlo simulation programs, such as EGSnrc, are coded to set the threshold for each region to reduce the potential for error [56]. Given a properly selected threshold, range rejection reduces the simulation time without affecting the accuracy of the result.

4.4.4. Photon Forcing

Photon forcing involves triggering an interaction within a given component module, for all photons which pass through it. The result of the forced interaction is a scattered photon with statistical weight proportional to the probability of an unforced interaction, and an unscattered photon with the remaining statistical weight [56]. It is primarily used when the simulation is intended to study the effects of a small component module, which may not be subject to a large number of unforced interactions. However, the process of transporting the photon to the

interaction point may increase the simulation time, especially if the component is large enough to allow multiple interactions [55].

4.4.5. Cross Section Enhancement

Cross section enhancement is used to increase Bremsstrahlung production by multiplying the probability of radiative electron interactions by an enhancement factor. It allows more rapid generation of photon fluence useful for further simulation. The statistical weight of each photon is decreased proportionally to the enhancement factor [55]. Cross section enhancement is best used for low energy charged particles, which produce so few photons that particle splitting does not improve the simulation time, or in conjunction with particle splitting to produce a large number of photons in few histories [56].

4.5. EGSnrc

EGSnrc is a Monte Carlo particle transport code developed by the National Research Council of Canada. EGSnrc includes several refinements to the physics models used by EGS4, and is periodically updated with the latest developments [53]. EGSnrc consists of several applications which address different aspects of the simulation and analysis of radiation transport as applies to dosimetry.

4.5.1. BEAMnrc

BEAMnrc [57] is a software tool used to simulate radiation beam sources (e.g. a medical linear accelerator). BEAMnrc simulates a radiation source via an accelerator file, consisting of a series of component modules ordered by their position along the main axis of the accelerator. One

BEAMnrc output is a phase space file, which contains a record of particle position, energy, and trajectory at a plane. A phase space file can be used in further simulations or used to analyze the output of a source.

BEAMnrc inputs specify the accelerator file, the simulation settings (e.g. number of histories, desired outputs), the particle source, the transport parameters (e.g. maximum step size, VRT settings), and the location and composition of the component modules. The particle source may be a Gaussian or rectangular particle source, a phase space file, or even another BEAMnrc simulation to generate a particle for each new history. The source is defined in terms of particle type, particle energy, position, and orientation. BEAMnrc outputs a phase space file for a specified plane or planes normal to the main axis, and a data file containing the statistics on the simulation as a whole [56].

4.5.2. DOSXYZnrc and DOSRZnrc

DOSXYZnrc and DOSRZnrc are software tools used to calculate absorbed dose in media defined using Cartesian and cylindrical coordinates respectively. The volumes of interest are defined by ranges of voxels located relative to a reference point. Each voxel both defines the medium and serves as a dose scoring region.

DOSXYZnrc and DOSRZnrc inputs define the beam and transport geometry, set the simulation parameters, and specify the output format. Like BEAMnrc, they can use particle sources, phase spaces, or BEAMnrc simulations as sources. The two codes produce different outputs. DOSXYZnrc produces a "3ddose" file, which stores the dose to each scoring region in the voxel array and the associated uncertainty [58]. This can be analyzed and represented via profiles and percent depth dose curves. DOSRZnrc records the dose absorbed by specified scoring

region or regions. DOSRZnrc can also record other aspects of energy deposition (e.g. dose due to scattered particles, kerma) for analysis [59].

Monte Carlo simulations are a powerful tool in medical physics research. Simulations can be used to easily test the effects of variation in the experimental parameters. The ability to precisely alter and control parameters is invaluable. However, no one tool can accomplish every task. The outcomes of Monte Carlo simulations, especially those of novel delivery methods or accessories, must be validated against experimental data.

CHAPTER 5

COLLIMATOR TRANSFERABILITY:

DOSIMETRIC CHARACTERIZATION

A design requirement of the mini-beam collimator was that it be easily implemented across multiple medical linear accelerators. To verify that this condition is met, dosimetric characterization measurements of the mini-beam collimated field on multiple linacs was carried out. The experimental measurements were divided into two parts. One consisted of the spatially-dependent measurements of the open and mini-beam collimated field. These measurements included dose profiles and percent depth dose curves which were used to characterize the dose distribution and beam quality of the open and mini-beam collimated fields. The other part consisted of the central axis point dose measurements of the collimated and open fields. These measurements were used to calculate the relative output factors of the open and mini-beam collimated fields for each linear accelerator.

This chapter will first give an overview of the initial dosimetric characterization measurements, including an overview of the setup and use of the mini-beam collimator and a summary of the quantities of interest. Next, the experimental tools used in performing the measurements will be introduced. The method by which the measurements were taken will be explained. Finally, the results of the measurements will be presented and a discussion of the implications of these results presented.

5.1. The Mini-Beam Collimator

The dosimetric transferability of the mini-beam collimator was the goal of this study. However, the mini-beam collimator produces a mini-beam array, which exhibits significant changes in dose over very small spatial displacements. Certain factors must be considered in the characterization of such a field that do not arise in a conventional field. An overview of the mini-beam collimator and the dosimetric framework necessary to characterize the beam is provided to place the measurements in context.

5.1.1. Design

The collimator uses an array of tungsten blades 100 mm in depth and 0.6 mm wide mounted in an aluminum frame, which produces alternating high and low dose regions, as shown in Figure 5.1. The blades are arranged parallel to the nominal beam divergence angle, to ensure that the dose at each peak remains constant across the field. The collimator assembly's aperture is 4.2 cm x 4.2 cm, which allows for a mini-beam array for any field up to 5 cm x 5 cm projected at isocenter. The collimator assembly is mounted in a standard Varian accessory mount for attachment to the accelerator head. The collimator mounting includes angular and lateral position adjustments. The lateral position control has a precision of 1.0 micrometer.

The mini-beam collimator divides the field by occluding regular sections with the tungsten blades. The spaces between the blades, called “septa,” allow the beam to pass uninterrupted, producing the mini-beam array. The blade spacing was specified to produce mini-beams with a width of 1 mm at isocenter [23].

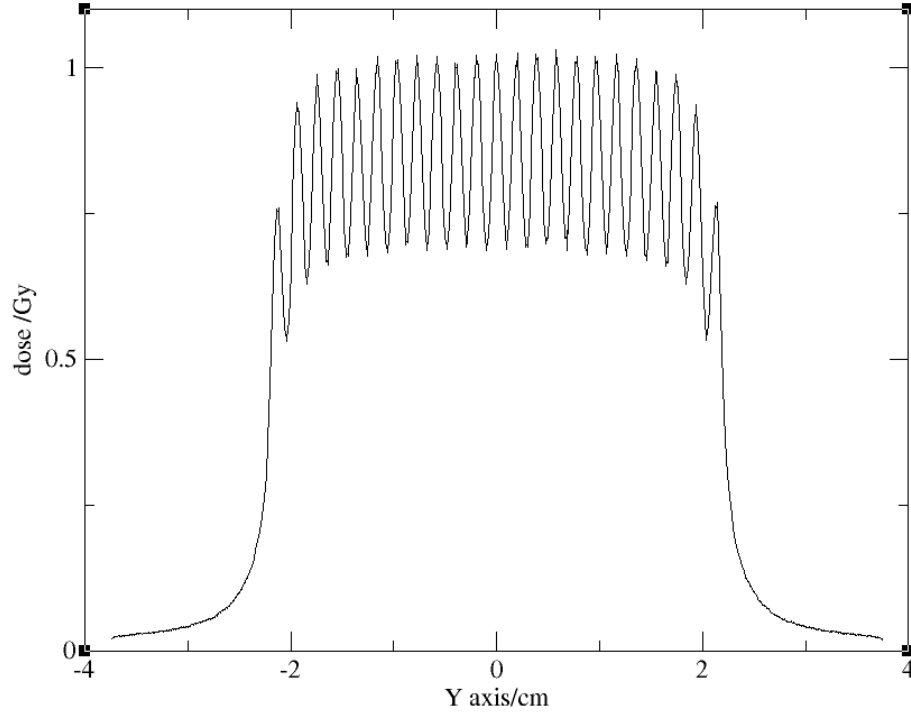


Figure 5.1. Simulated dose profile of a mini-beam array at 10 cm depth in water.

The collimator is shown in Figure 5.2. The mini-beam collimator fits into the linear accelerator accessory mount below the jaws and multi-leaf collimators (MLC). Thus, the only change between generation of a mini-beam collimated field and an open field is the presence or absence of the mini-beam collimator.

5.1.2. Dosimetric Framework

Relative output factors (OF_f^w) and collimator factors (CF_f^w) were obtained for the open fields (f_{clin}) and mini-beam collimated fields (f_{mini}), respectively. These values were linked by a dosimetric framework developed during the commissioning of the mini beam collimator [23]. As described in Equation 3.17, relative output factors are ratios of doses to water (D_f^w) used to characterize a field of interest (f_{clin}), relative to a reference field (f_{ref}), such that:

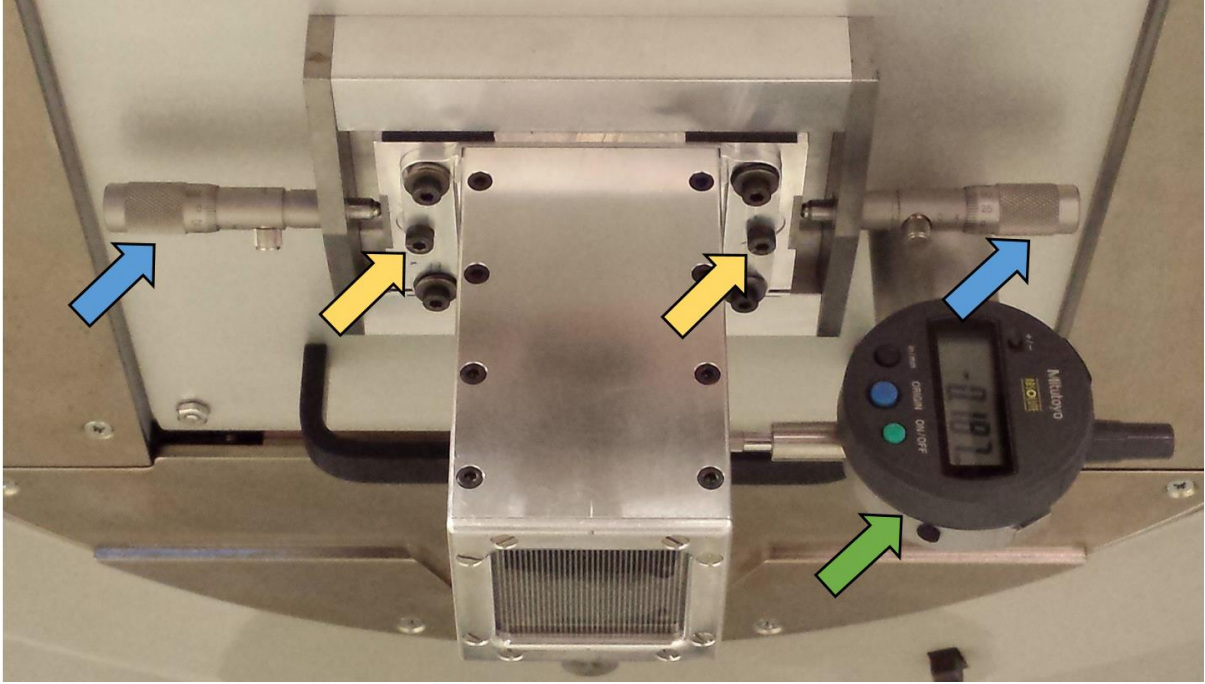


Figure 5.2. The mini-beam collimator mounted in the accessory mount of a Varian iX linear accelerator. The yellow arrows indicate the collimator inclination adjustment screws, the blue arrows indicate the lateral adjustment micrometers, and the green arrow indicates the digital micrometer used to display lateral position [23].

$$OF_{f_{clin}}^w = \frac{D_{f_{clin}}^w}{D_{f_{ref}}^w}. \quad (5.1)$$

When using the mini-beam collimator, the mini-beam relative output factor is defined as the product of the open field relative output factor ($OF_{f_{clin}}^w$) and the collimator factor, such that:

$$OF_{f_{mini}}^w = OF_{f_{clin}}^w * CF_{f_{mini}}^w. \quad (5.2)$$

It follows that the collimator factor, which accounts for the effect of the mini-beam collimator can be determined by the ratio of point doses along the central axis in the mini-beam collimated field to that in the open field, as depicted in Figure 5.3, such that:

$$CF_{f_{mini}}^w = \frac{D_{f_{mini}}^w}{D_{f_{clin}}^w}. \quad (5.3)$$

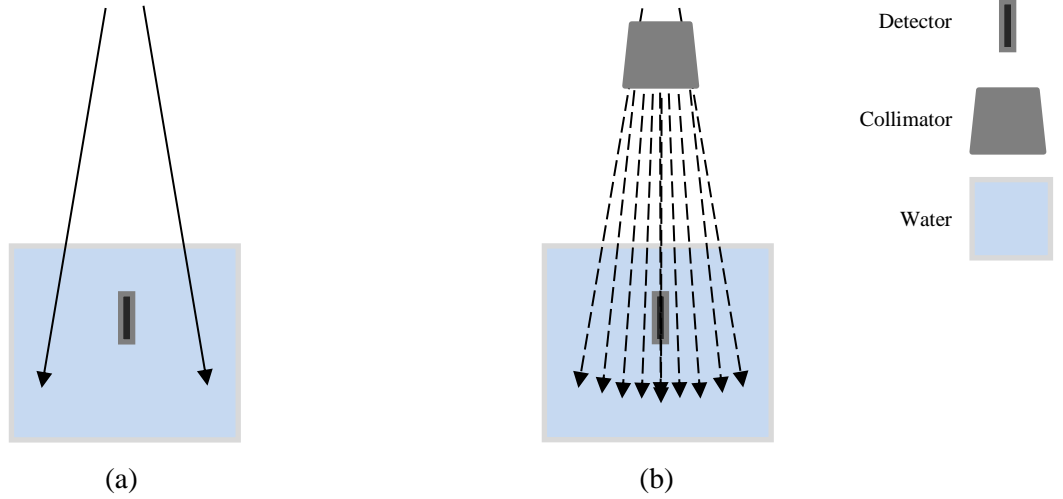


Figure 5.3. Experimental setups for collimator factor measurement. (a) shows the detector in water under an open field. (b) shows the detector in water with the mini-beam collimator in place. The detector position and field size remain unchanged between the two setups.

However, dose-to-water cannot be measured directly, and the calculation of a dose ratio based on measurement must account for the relative stopping powers and mass attenuation coefficients of the detector relative to water, as described in Equations 3.11 and 3.13 [60]. These coefficients are dependent on the field sizes being measured [61]. Therefore, measured collimator factor is more appropriately defined as:

$$CF_{f_{mini}}^{det} = \frac{D_{f_{mini}}^{det}}{D_{f_{clin}}^{det}}, \quad (5.4)$$

and:

$$OF_{f_{mini}}^{det} = OF_{f_{clin}}^{det} * CF_{f_{mini}}^{det}. \quad (5.5)$$

where D_f^{det} is the dose to the detector active volume in the field of interest.

In the case of this experimental setup, the stopping power ratio between water and the detector active volume is relatively insensitive to a change between f_{clin} and f_{mini} [23]. Therefore, it can be assumed that the change in D_{field}^{det} is due entirely to the change in electron fluence between

fields, as described in Equation 3.11, and the relative dose can be considered equivalent to the ratio of detector signals (M_{field}^{det}) such that:

$$\frac{D_{f_{mini}}^{det}}{D_{f_{clin}}^{det}} = \frac{M_{f_{mini}}^{det}}{M_{f_{clin}}^{det}}, \quad (5.6)$$

And, therefore, Equation 5.4 can be expressed as:

$$CF_{f_{mini}}^{det} = \frac{M_{f_{mini}}^{det}}{M_{f_{clin}}^{det}}. \quad (5.7)$$

The open field relative output factor can be simplified similarly, such that Equation 3.17 can be expressed as follows:

$$OF_{f_{mini}}^{det} = \frac{M_{f_{clin}}^{det}}{M_{f_{ref}}^{det}}. \quad (5.8)$$

5.2. Experimental Apparatus

Experimental measurements using the mini-beam collimated field on each of the three medical linear accelerators (linacs) were performed with two unshielded diode detectors in a water phantom. The experimental apparatus is shown in Figure 5.4.

5.2.1. Medical Linear Accelerators

Three clinically beam matched medical linear accelerators were used in this study. All three were Varian Clinac iX accelerators, designated Linacs 1 – 3 for the purposes of this study. The medical linear accelerators are located at the Saskatoon Cancer Center. All measurements were performed at a nominal beam energy of 6 MV.



Figure 5.4. Linac 1 with the mini-beam collimator installed, the MP3 water phantom positioned, and the TANDEM electrometer unit connected to the detector.

The Saskatoon Cancer Centre's requirement for clinical beam matching is agreement to within less than half the threshold recommended by TG-142 [62]. As described in Chapter 3, the AAPM TG-51 code of practice for reference dosimetry is used to calibrate the linear accelerator outputs and ensure consistency [34].

5.2.2. Diode Detectors

Two unshielded diode detectors were used for the characterization measurements. Diodes were selected over ionization chambers due to their small active volume size, granting the greater spatial resolution necessary to properly resolve the mini-beams. The PTW⁴ 60017 (PTWe) has a circular active volume with a manufacturer specified diameter of 1.2 mm and an effective depth

⁴ PTW - New York Corporation, Brooklyn, NY, United States - www.ptw.de

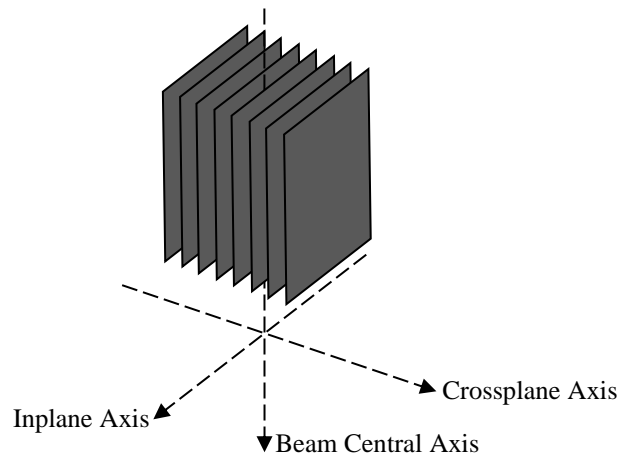


Figure 5.5. The measurement axes defined with respect to the mini-beam collimator blades.

of 3 mm. The Scanditronix⁵ stereotactic field diode (SFD) has a circular active volume with a manufacturer specified diameter 0.6 mm and effective depth of 0.06 mm. The accumulated charge from these detectors was read using a PTW TANDEM electrometer. It should be noted that clinical dosimetric characterization measurements are typically performed using an ion chamber. However, the intent of these measurements was to compare the results across multiple linacs, which requires only that the same detector used on all measurements being compared, permitting the use of the higher resolution diode detectors.

5.2.3. Water Phantom

A PTW MP3 water phantom was used for all measurements. The phantom consists of a water tank containing arms for positioning the detector. The phantom is able to position the detector within a 50 cm x 50 cm x 40 cm volume with a manufacturer quoted uncertainty of ± 0.01

⁵ IBA Dosimetry, Bartlett, TN - <http://www.iba-dosimetry.com>

cm in three dimensions. When describing measurements with the mini-beam collimator, the axis perpendicular to the mini-beams is the “crossplane” axis and the axis parallel to the mini-beams is the “inplane” axis. The axes relative to the mini-beam collimator blades are shown in Figure 5.5.

5.2.4. MEPHYSTO mc²

The PTW MEPHYSTO mc² software package was used to perform and process the water tank measurements. The characterization measurements made use of the CenterCheck, tbaScan, DataAnalyze, and TanSoft applications executed within the MEPHYSTO interface.

- CenterCheck was used to determine the center point and inclination of the field relative to the water tank by examination of profiles of a square field in both axes at two depths.
- tbaScan was used to perform profile and percent depth dose measurements. It is also capable of analysis of the measured profiles and percent depth dose curves (e.g. calculating field size and d_{max}).
- DataAnalyze was used to analyze and format (e.g. normalize or smooth) the profiles and percent depth dose curves. As well, it can add or average multiple profiles or percent depth dose curves.
- TanSoft was used as the software interface with the TANDEM electrometer when performing point dose measurements. Measurements were performed using the charge measurement node over a 20 second integration time. The TanSoft/TANDEM reading has a stated reproducibility of $\pm 0.5\%$.

5.3. Experimental Setup

To ensure consistency in the measurements, a standard procedure for setup was established and followed. The AAPM recommendations for reference dosimetry [34] and commissioning [62] of high energy photon beams were used to guide the measurement procedure in order to ensure consistency with established dosimetry practice. The following procedure was used for all experimental measurements.

5.3.1. Water Phantom Setup

The first step was to position the water phantom and set up the associated equipment. With the linear accelerator gantry angle set to 0° , the water tank was aligned with the linear accelerator field and levelled using the adjustable base. All angles were verified by the use of a digital level with a precision of $\pm 0.05^\circ$. The detector and electrometers were connected to the phantom and the computer operating MEPHYSTO. All electrometers were located at the end of the treatment couch opposite the beam to prevent contamination of the signal by the radiation. After all electronics were connected, the water phantom was filled to an SSD of 100 cm, the standard distance for reference dosimetry [34, 42]. The detector and positioning mechanism were kept below the water surface to ensure that water displacement was accounted for in the SSD measurement.

5.3.2. Detector Centering

MEPHYSTO uses a set center point as the origin when locating the detector. The centering process matches this point to the physical center of the field at the water's surface. The diode center was set before any measurements were taken and whenever the detector position was adjusted.

The centering procedure for the mini-beam field was adopted from earlier dosimetry work involving very small photon fields [64]. The diode was located near the beam center by visual inspection of detector center and the linear accelerator beam crosshairs. CenterCheck was used to center the diode in a 2 cm x 2 cm open field with scans at 5 cm and 15 cm depth. This step localized the detector to better than 1 mm of the field center, and served to verify that the gantry and water tank were level. After this, tbaScan was used to double check the diode position. Profiles in both axes were taken for 1 cm x 1 cm and 0.5 cm x 0.5 cm fields at a depth of 10 cm with a detector axial positional increment of 0.03 cm. The tbaScan Analysis tool was used to determine the central axis offset (CAX) from the beam. The center point was corrected by the measured CAX, until the calculated offset from the field center was below ± 0.01 cm, the maximum resolution of the detector positioning, for both fields.

5.3.3. Mini-Beam Collimator Centering

Due to the small size of the mini-beams, and the collimator being an attachment to the linear accelerator that was removed and replaced between measurements, it was necessary to verify the position of the mini-beam collimator as well. This procedure was developed in the initial commissioning study of the mini-beam collimator [23]. First, the collimator inclination was checked with the level to ensure that it was aligned with the field. After this was verified, the crossplane dose profile was measured for a 4 cm x 4 cm field at a depth of 10 cm with a detector position increment of 0.02 cm, twice the uncertainty of the detector position. This provided the highest resolution possible while minimizing overlap of the active volume between measurement points. The detector alignment with the central mini-beam was verified by visual inspection of the profiles to ensure that the central peak was coincident with the detector center position.

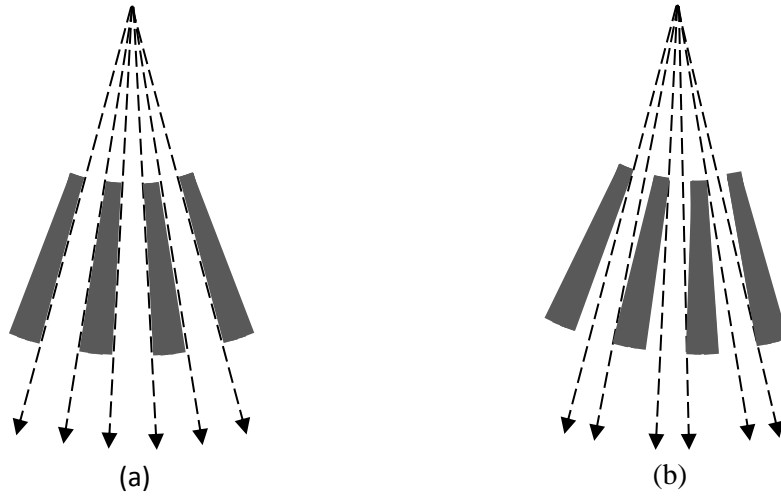


Figure 5.6. An illustration of the effect of angular misalignment. (a) collimator inclination and beam inclination in alignment. (b) collimator inclination out of alignment with the beam inclination,

In the event that an offset was found, it was necessary to adjust the collimator position. When performing this adjustment, the lateral positioning micrometers on the collimator base were adjusted by the offset measured by tbaScan until the central mini-beam was aligned with the central axis of the open field.

5.3.4. Mini-Beam Collimator Alignment

The design process and initial characterization of the mini-beam collimator assumed that the collimator was perfectly aligned with the beam central axis. As shown in Figure 5.6, misalignment results in an increase in effective blade width, with an accompanying reduction in the effective width of the air septa which define the mini-beams. The blade width was one of the key parameters during the design process, which had a significant impact on the dose distribution [23].

During dosimetric characterization, it was observed that the beam alignment with respect to the accessory mount varies between accelerators by an amount sufficient to cause observable changes to the measured collimator factor. In order to eliminate this variation between the accelerators, it was necessary to adjust the collimator inclination to match the inclination of the beam central axis. The collimator alignment step was added to the established measurement procedure to account for the effect.

When measuring the collimator factor over a range of collimator inclinations, the highest measured collimator factor corresponds with the inclination at which the collimator is aligned with the beam. Therefore, the collimator could be aligned by finding the inclination at which the collimated field point dose peaked, as this point has the highest ratio of $M_{f_{mini}}^{det}$ to $M_{f_{clin}}^{det}$ (Equation 5.7). The alignment was carried out by seeking this point.

The inclination of the collimator was set using the angular adjustment screws. Due to the high precision necessary to consistently locate the collimator inclination aligned to the beam, the position was defined by the change in the micrometer reading, and the corresponding change in angle was calculated from the collimator position at the level of the micrometer. To locate the point of maximum dose, TanSoft was used to perform point dose measurements in a 4 cm x 4 cm field at 10 cm depth. At each collimator inclination, the detector was centered in the mini-beam by adjusting the detector position in 0.01 cm increments in the crossplane axis and performing repeated measurements of the point dose at each step. The centered detector position was that which obtained the highest dose. The centered detector doses were compared in order to identify the point of maximum dose. The 0° inclination was defined as the aligned inclination for the linac.

It was observed that the peak dose tended to remain constant within measurement uncertainty near the peak, meaning the optimal inclination could not be conclusively determined

by a single measurement. While the variation in dose over this region was within clinical tolerance, the range was too wide to carry out repeatable measurements at non-zero inclinations. A second check was used to set the zero point of the collimator inclination with sufficient precision. First, the approximate center was located by finding the range of inclinations over which the point dose remained unchanged. The center of this region was taken as a starting center position. The location of the center point was refined by performing point dose measurements at some non-zero inclination on each side of the peak. The ideal center position was taken to be the point equidistant from equal point doses. This condition was met by adjusting the offset measurement to minimize the difference between the point doses at each inclination. An offset of 0.075 mm (0.086°), the largest change in inclination used in characterization measurements, was used for centering.

5.4. Measurement Procedure: Dose Profile and Percent Depth Dose

The same nominal 6 MV photon beam was used for all profile and percent depth dose measurements. While 10 cm x 10 cm fields are the accepted standard for reference dosimetry [34, 42], the width of the collimator aperture precluded such a wide beam. A 4 cm x 4 cm field was used for profile and %DD measurements, as the 4 cm field was selected as the largest field which would be necessary during the collimator design process and was used as a benchmark during the commissioning study. To reduce the effects of a particular setup, all measurements were performed at least three times for independent setups and averaged to calculate the reported value and associated uncertainty. These measurements were taken with the SFD diode detector in the horizontal orientation. This served to ensure that the active volume was wholly within the central mini-beams for %DD measurements and maximized the crossplane positional resolution in the dose profile measurements [65], as shown in Figure 5.7.

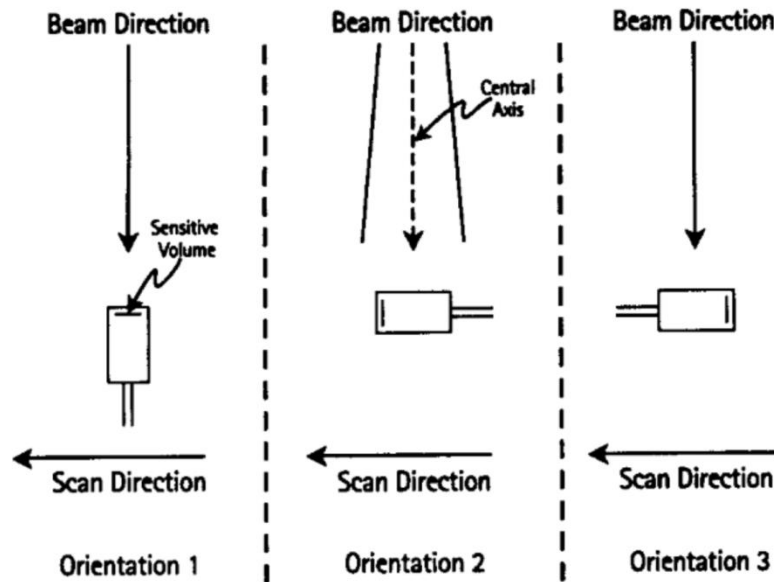


Figure 5.7. Diode detector structure and orientation. Orientations 1 and 2 were used in this study, according to the needs of the measurement. The same orientation was used for all measurements of a given type. Image from Beddar *et al.* 1994 [65], used with permission.

5.4.1. Percent Depth Dose Measurement

An important feature of the collimator which required verification was that the mini-beams are of equal beam quality to the open field. This condition was tested via %DD measurements. %DD were taken along the beam central axis at increments of 0.1 cm from 0 cm to 2 cm depth, 0.25 cm steps from 2 cm to 6 cm depth, and 0.5 cm from 6 cm to 25 cm depth. %DD were measured for both collimated fields and open fields on each linear accelerator.

5.4.2. Profile Measurement

Dose profile measurements were taken along the central crossplane axis at increments of 0.2 mm at the reference depth in water of 10 cm. This fine increment was selected to properly resolve the mini-beams while ensuring that the separation between each measurement point was

greater than the positional uncertainty offered by the water tank. For consistency, this resolution was also used for the open field measurements. Dose profiles were obtained for both mini-beam collimated fields and open fields on each linear accelerator. The mini-beam collimated profiles can be compared using the peak-to-valley dose ratio (PVDR). The PVDR was calculated as the ratio of the average of the peak doses to the average of the valley doses such that:

$$PVDR = \frac{D_{peak}^{avg}}{D_{valley}^{avg}}. \quad (5.9)$$

Only the peaks and valleys within the central region of the beam are included when calculating the average values.

5.4.3. Data Collation

DataAnalyze was used to amalgamate the profile and percent depth dose measurements from multiple sessions. The “Average” function was used to combine multiple measurements into a single result for each linac. A minimum of three profiles or percent depth dose measurements were used to construct each averaged data set. The “Smooth” function was used once on percent depth dose and open field profiles to eliminate any remaining noise in the averaged data set. The profiles for the mini-beam collimated field could not be smoothed, as the smoothing algorithm removed the peaks and valleys which distinguish the mini-beam array.

5.5. Measurement Procedure: Output Factors

Point dose measurements were taken for the mini-beam collimated and open fields for field sizes of 2 cm x 2 cm, 3 cm x 3 cm, 4 cm x 4 cm, and 5 cm x 5 cm. The measurement point was at 10 cm depth in water and centered in the field. To reduce the effects of a particular setup, all

measurements were performed at least three times for independent experimental setups and averaged to calculate the reported value and associated uncertainty.

All point dose measurements for each field were performed for both detectors. The detectors were used in the vertical orientation for point dose measurements. In each measurement session, the measurements were first performed for all four collimated fields then for all four open fields to ensure that the collimator position was constant for all fields. Each point dose reading was performed five times and the average of the values was taken. These averages were taken to be the field point dose for that measurement session.

The open field relative output factor was calculated from the ratio of point dose in the open field of interest relative to the point dose in the 5 cm x 5 cm field for the 2 cm x 2 cm, 3 cm x 3 cm, and 4 cm x 4 cm fields, as described in Equation 5.8. The 5 cm x 5 cm field was selected as the reference field [60].

Measured collimator factors for each session were calculated from the ratio of the collimated field point dose to the open field point doses for the 2 cm x 2 cm, 3 cm x 3 cm, 4 cm x 4 cm, and 5 cm x 5 cm fields, as described in Equation 5.4. The mini-beam relative output factors were calculated by taking the product of the open-field relative output factors and the measured collimator factor, as described in Equation 5.5.

5.5.1. Effects of Collimator Inclination on Collimator Factor

In order to characterize the relationship between collimator factor and collimator inclination with respect to the beam central axis, point dose measurements were performed for four collimator inclinations. Both the PTWe and SFD detectors were used in the vertical orientation.

Point dose measurements in the mini-beam collimated field and open field were taken at collimator positions of 0.000, ± 0.025 , ± 0.050 , and ± 0.075 mm offset from the baseline position described in Section 5.3.3 and 5.3.4 (corresponding to changes in inclination of 0.00, ± 0.03 , ± 0.06 , and $\pm 0.09^\circ$, respectively) for 2 cm x 2 cm, 3 cm x 3 cm, 4 cm x 4 cm, and 5 cm x 5 cm. The measurements at the three non-zero inclinations were performed at the given offset in both directions from the 0.0° collimator inclination. The collimator factor obtained for the collimator inclination of 0° was taken as the optimized collimator factor.

5.5.2. Uncertainty in Measurements

The uncertainty in the average measured value of N experimental setups was determined as described in Chapter 3, such that:

$$u_{CF_{f_{mini}}^{det}} = \frac{2\sigma(CF_{f_{mini}}^{det})}{\sqrt{N}} \quad (5.10)$$

The uncertainty in the relative output factor was obtained in the same way. When calculating the relative output factor as described in Equation 5.5, the uncertainties are added in quadrature, such that:

$$u_{OF_{f_{mini}}^{det}} = \sqrt{\left(u_{OF_{f_{clin}}^{det}}\right)^2 + \left(u_{CF_{f_{mini}}^{det}}\right)^2}. \quad (5.11)$$

5.6. Experimental Results

Measurements of the open field and mini-beam collimated field were used to dosimetrically characterize the mini-beam collimator on each medical linear accelerators.

	Linac 1	Linac 2	Linac 3	Mean
%DD(10 cm) (%)	61.75 ± 0.21	61.83 ± 0.28	62.15 ± 0.64	61.84 ± 0.24
d_{max} (cm)	15.99 ± 0.11	16.00 ± 0.68	16.10 ± 0.06	16.06 ± 0.07
Field Size (cm)	4.40 ± 0.02	4.39 ± 0.02	4.40 ± 0.03	4.40 ± 0.01
Beam Symmetry (%)	0.29 ± 0.01	0.43 ± 0.08	0.39 ± 0.02	0.33 ± 0.08

Table 5.1. Metrics of the open field and the associated uncertainty across the three linear accelerators. The mean value and measurement uncertainty for each quantity are also given.

5.6.1. Open Field Measurements

Table 5.1 summarizes the main features of the open field on the three linear accelerators. The %DD(10 cm) and d_{max} were obtained from the percent depth dose curves, and the field size and beam symmetry were obtained from the dose profiles. The %DD, d_{max} , and field size at 10 cm depth were compared to the mean value to quantify the dosimetric variation across linacs.

The SCC requirement for clinical beam matching is agreement to within half the threshold recommended by TG-142 [62]. In the context of these measurements, the condition is satisfied by the %DD(10), d_{max} , and field size all showing agreement back to the baseline value within $\pm 0.5\%$, and the beam symmetry being within $\pm 0.5\%$ of zero.

Table 5.2 states the open field relative output factors calculated for each linear accelerator. The open field dose measurements for each field obtained by each detector were used to calculate these values for comparison. All values were found to agree within $\pm 0.5\%$ of the mean, meeting the threshold for clinical beam matching.

5.6.2. Mini-Beam Collimated Percent Depth Dose and Dose Profiles

Measurements of percent-depth dose curves and dose profiles were performed before the effect of changes in the collimator inclination angle was quantified. These results serve to demonstrate the effect of collimator alignment.

	Linac 1		Linac 2		Linac 3	
Field (cm ²)	PTWe	SFD	PTWe	SFD	PTWe	SFD
4 x 4	0.964 ± 0.001	0.963 ± 0.001	0.963 ± 0.001	0.961 ± 0.001	0.962 ± 0.001	0.961 ± 0.001
3 x 3	0.924 ± 0.001	0.919 ± 0.001	0.923 ± 0.001	0.918 ± 0.001	0.923 ± 0.001	0.919 ± 0.001
2 x 2	0.880 ± 0.001	0.871 ± 0.001	0.878 ± 0.001	0.870 ± 0.001	0.878 ± 0.001	0.870 ± 0.001

Table 5.2. The measured open field relative output factors (relative to a 5 cm x 5 cm reference field) with the measurement uncertainty for each accelerator and diode detector.

5.6.2.1. Percent Depth Dose

Figure 5.8 compares the percent depth dose for the collimated fields with the average open field percent depth dose. Table 5.3 states the d_{max} and $\%DD(10)$. Little deviation from the open field can be seen, with a nearly identical d_{max} and $\%DD(10)$. All collimated field d_{max} differ from the averaged open field d_{max} by less than $\pm 0.43\%$. All three linacs differed from the mean mini-beam collimated field $\%DD(10)$ by $\pm 0.6\%$ or less, slightly in excess of the local standard of $\pm 0.5\%$, but satisfying the TG-142 standard. The averaged open field $\%DD(10)$ was consistent with this range. This satisfies the clinically beam matched criterion and shows that beam quality of the mini-beam collimated fields is clinically equivalent to that of the open field. However, the surface dose is slightly higher for the mini-beam collimated fields than for the open field. This is indicative of electron contamination: low energy electrons freed from the mini-beam collimator by photon interactions influencing the energy spectrum [33].

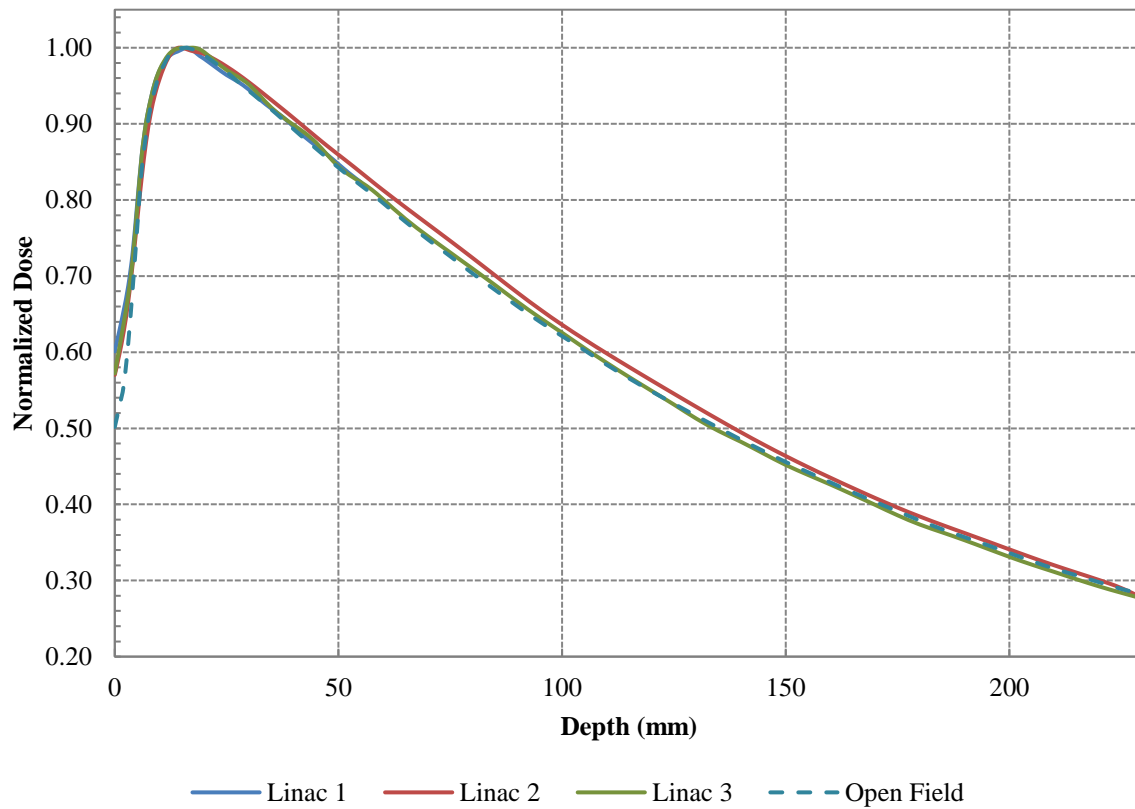


Figure 5.8. %DD for the mini-beam collimated field on each linear accelerator. Also shown is the average of the %DD for the open field, as calculated using the MEPHYSTO software.

Linac	%DD(10)	d_{\max} (mm)
1	61.25 ± 0.18	16.10 ± 0.29
2	61.93 ± 0.24	15.99 ± 0.36
3	61.49 ± 0.17	16.00 ± 0.49
Open	61.84 ± 0.24	16.06 ± 0.07

Table 5.3. Beam quality specification for the collimated fields on each linear accelerator and the average of the open fields, all with the measurement uncertainty.

5.6.2.2. Dose Profile

Figure 5.9 shows the dose profiles of the mini-beam collimated field on each linear accelerator, normalized to the central axis dose. Also included is the average of the three open-

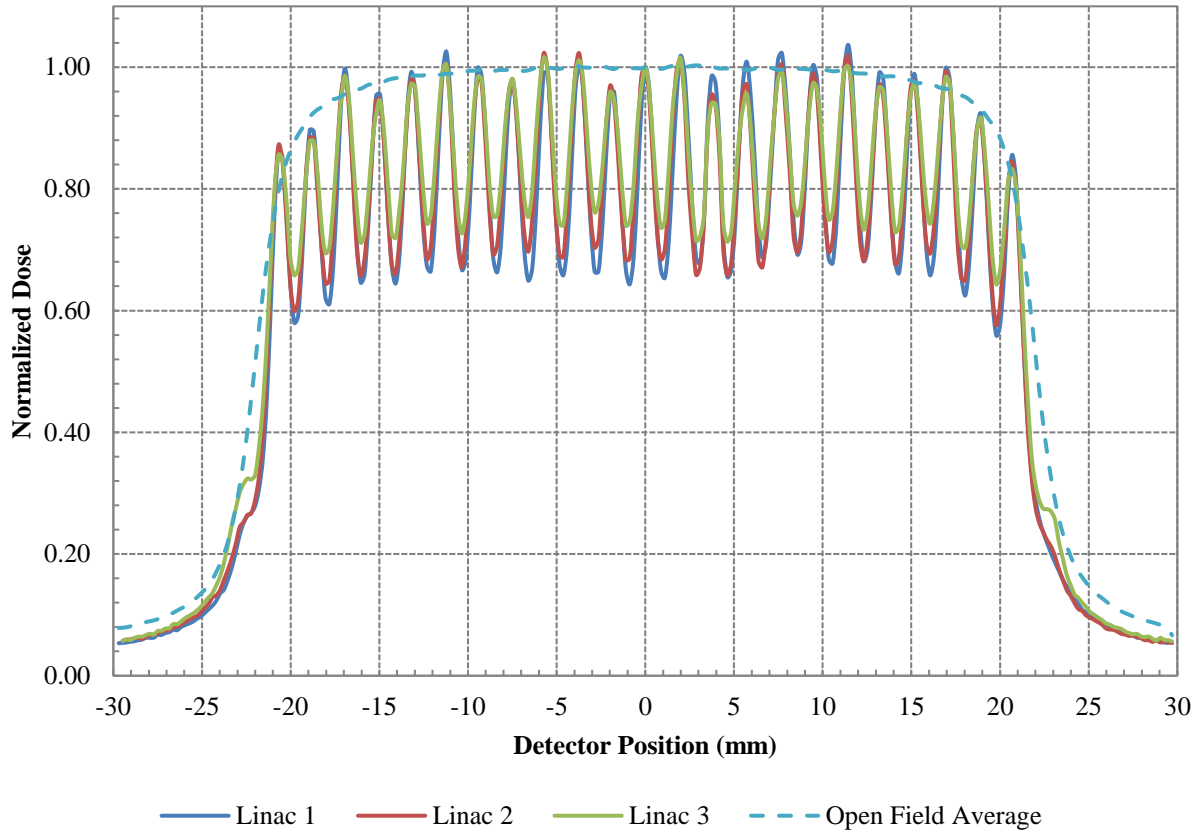


Figure 5.9. Dose profiles (normalized to the central axis dose) at 10 cm depth for the mini-beam collimated field on each linear accelerator. The average of the dose profiles at 10 cm depth for the open field, as calculated by MEPHYSTO, is also shown.

Linac	PVDR
1	1.510 ± 0.003
2	1.446 ± 0.003
3	1.343 ± 0.003

Table 5.4. The calculated peak-to-valley dose ratio and uncertainty for each linear accelerator.

field profiles. The associated PVDR are shown in Table 5.4. The overall spatial dose distribution is consistent across the linacs, and matches the footprint of the open field measurements. However, the profiles disagree across linacs in two main regards.

The most interesting result shown in Figure 5.9 and Table 5.4 is the variation in PVDR. The lowest PVDR (Linac 3) and the highest PVDR (Linac 1) differ by 11.1%, having a maximum deviation from the mean PVDR of 6.3% in the case of Linac 3, exceeding the measurement uncertainty and beam matching threshold.

Note also that the peak doses are not perfectly consistent from peak to peak. This is due to the limitations of the manufacturing process, since subtle irregularities in the blade spacing can cause an observable difference in the peak dose. However, the relative dose of each peak is consistent across all medical linear accelerators (e.g. the peak immediately to the left of the central peak is lower than average for all three linacs). While non-ideal from a dosimetric perspective, this variation remains within acceptable bounds, and proved useful to ensure that the collimator was always centered on the same peak.

5.6.3. Collimator Factors

Collimator factor measurements were performed on each linear accelerator. Figure 5.10 shows the measured collimator factors for each linac correlated with field side length. The values are also stated in Table 5.5. They show that the collimator factor decreases with increasing field side length. The relationship between the two quantities is linear within the measurement uncertainty.

Also evident in Figure 5.10 is the change in collimator factor across linacs, with deviation from the mean of up to 2.8% in the case of Linac 3. This is well in excess of the measured uncertainty, and exceeds the threshold for beam matching. This discrepancy is observed for both detectors, which show the same ordering of collimator factors. Also note that the collimator factors measured by the two detectors differ. This is a feature of the detectors. The nominal diameter of

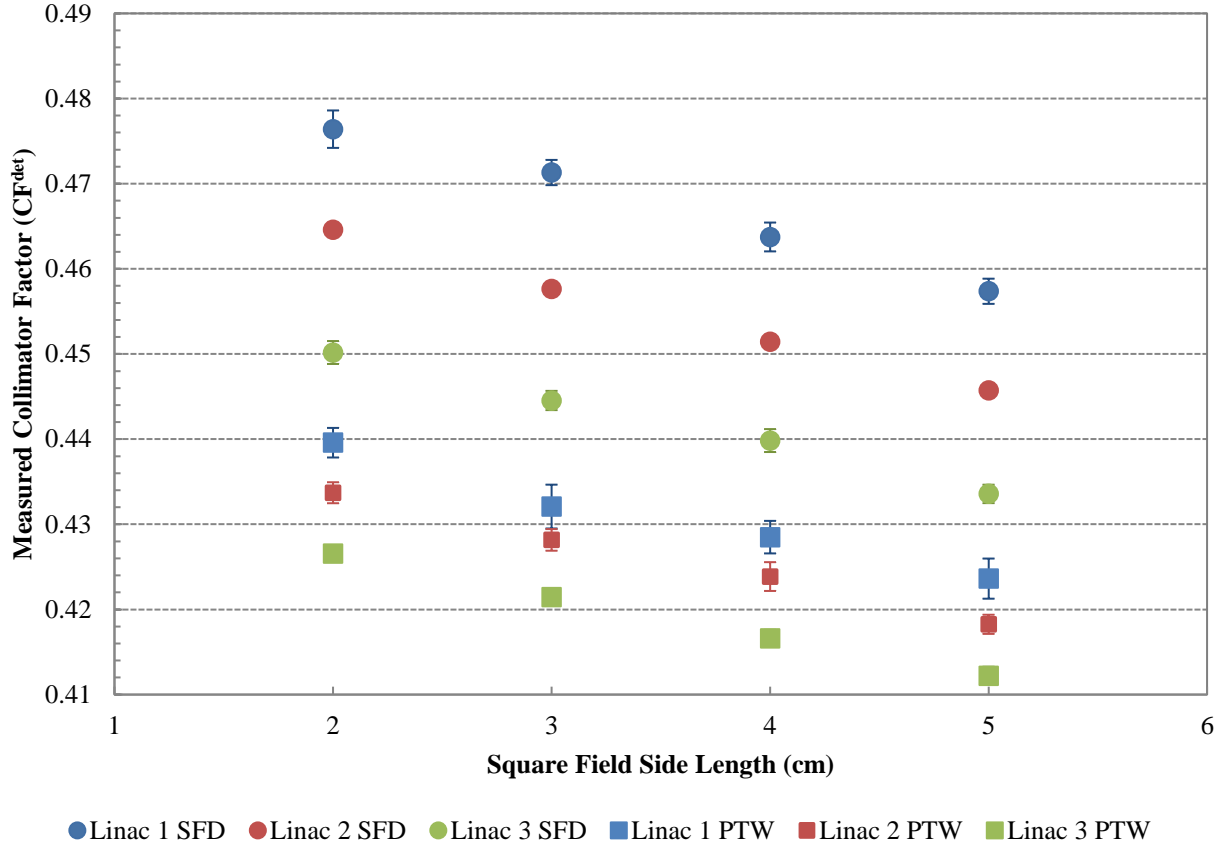


Figure 5.10. Measured collimator factors for each diode detector.

the PTWe active volume (1.2 mm) is slightly larger than the nominal FWHM of the mini-beams at a depth of 10 cm for SSD = 100 cm (1.1 mm). This leads to some volume averaging across the mini-beam array, resulting in a reduced detector signal. The SFD does not display this effect because its active volume is narrower than the mini-beams.

5.6.4. Collimator Factor as a Function of Collimator Inclination

Figure 5.11 shows the measured collimator factor plotted against collimator inclination angle with respect to the beam central axis. The measured collimator factors show a strong and nonlinear dependence on inclination angle. Near alignment, the collimator factor is mostly insensitive to changes in inclination. However, a greater dependence on changes in inclination is

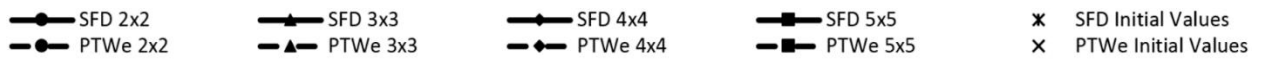
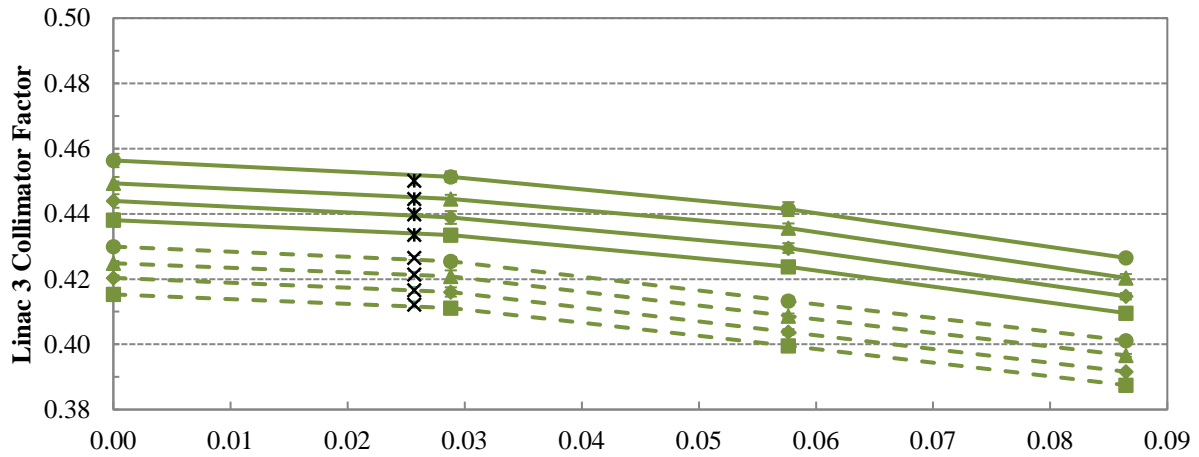
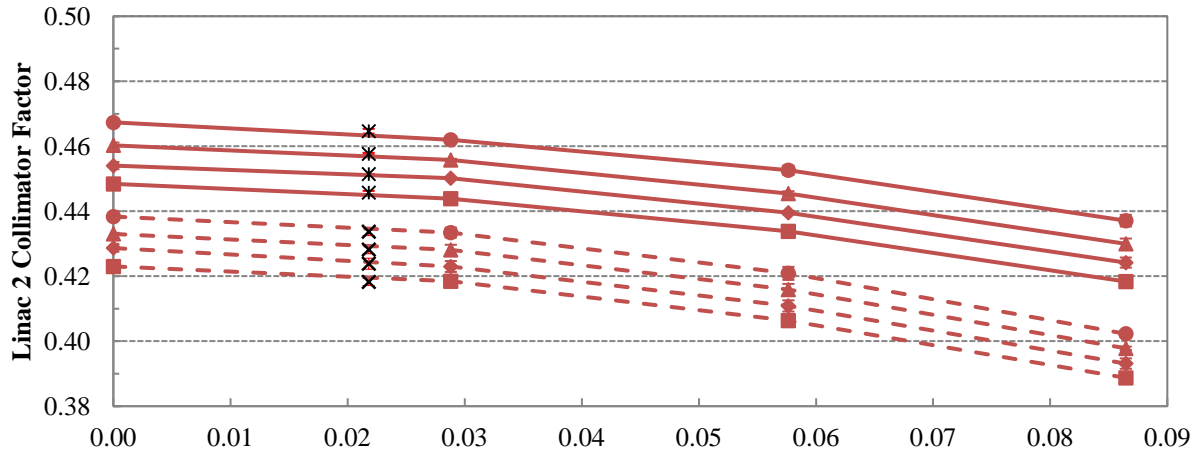
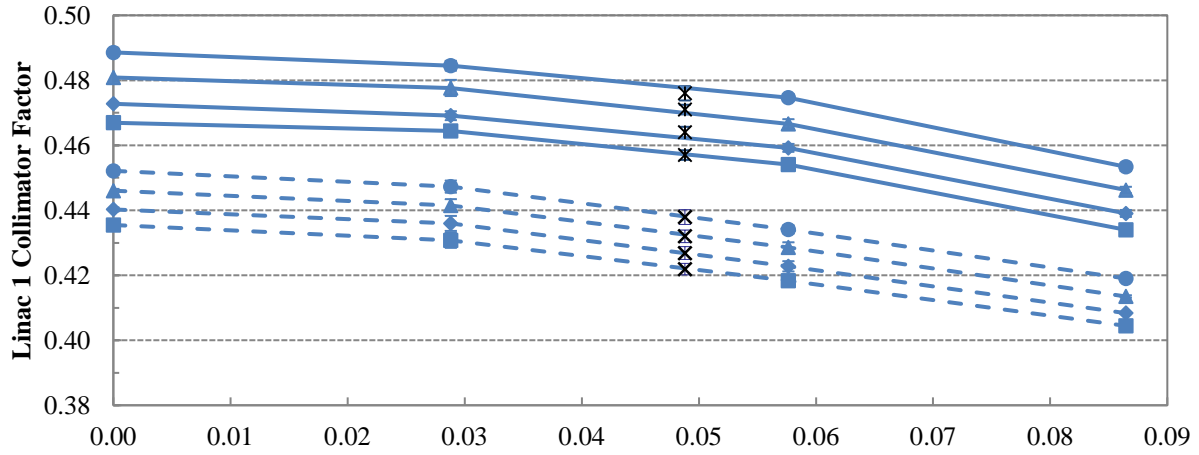


Figure 5.11. Measured collimator factor vs collimator inclination for each diode detector. The values obtained from measurements of the unaligned fields are also shown.

observed when the collimator is further at greater angles. The change in delivered dose as a function of collimator inclination was consistent on all three linacs, with a change in collimator inclination of 0.09° resulting in a clinically significant decrease in measured collimator factor of 7.1% for each detector. The differences incurred by changes in collimator alignment with respect to the beam central axis required that this effect be accounted for in the characterization process.

The original collimator factors (see Figure 5.10) are fitted within experimental uncertainty to the trends in Figure 5.11. The initial inclination angles for each linac did not correspond to the relative magnitude of the measured collimator factor, and the difference persists at alignment.

5.6.5. Aligned Dose Profiles

After the dependence on inclination was accounted for, the characterization measurements were repeated with the collimator aligned with the beam central axis. The percent depth doses remained unchanged, as they depend mainly on beam energy, which is insensitive to the presence of the mini-beam collimator, as shown in Figure 5.8. However, the dose profiles did respond to the collimator alignment, as shown in Figure 5.12. Table 5.5 shows the new PVDR for each linear accelerator. The lowest PVDR (Linac 3) and the highest PVDR (Linac 1) differ by >14%, with a maximum deviation from the mean of 8.1% in the case of Linac 1.

Comparing the profiles shown in Figure 5.12 to the profiles prior to alignment in Figure 5.9, it can be seen that failure to properly align the collimator for the linear accelerator results in a reduction in PVDR. This decrease is particularly noticeable at the edges of the field, where the alignment of the divergence angle of the beam and collimator blades is poorest. Similarly, deviation from 0° collimator inclination were found to result in asymmetric profiles. This is most noticeable for Linac 1, the least aligned of the original measurements. Due to the divergence of

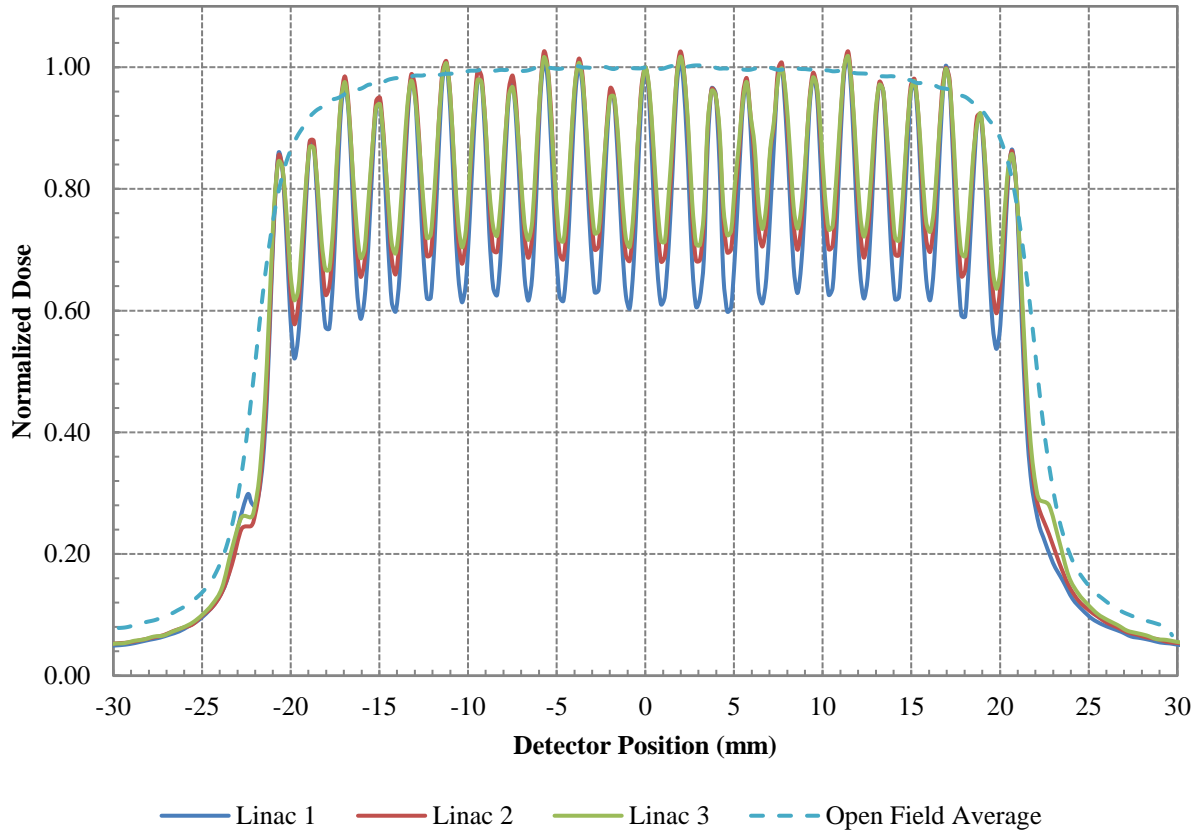


Figure 5.12. Dose profiles after collimator alignment at 10 cm depth normalized to the central axis dose on each linear accelerator. The average of the dose profiles at 10 cm depth for the open field, as calculated by MEPHYSTO, is also shown.

Linac	PVDR
1	1.595 ± 0.019
2	1.472 ± 0.023
3	1.414 ± 0.024

Table 5.5. The calculated peak-to-valley dose ratio and uncertainty for each linear accelerator.

the blades, one half of the septa would be further from alignment than the other, resulting in greater apparent blade spacing, and therefore a larger PVDR on one side of the profile. When the collimator is properly aligned with the beam central axis, the profile will appear more symmetric, aside from differences arising from variation in the blade spacing incurred during fabrication.

5.6.6. Aligned Collimator Factors

The collimator factors at a collimator inclination of 0° with respect to the beam central axis was taken as the final measured collimator factor. These measurements eliminate any variation due to collimator alignment, allowing for a more rigorous comparison. The results continued to show the same trends that were observed for the unaligned collimator: being linear within the measurement uncertainty, and showing the disagreement across linear accelerators.

5.6.6.1. Measured Collimator Factors

The final measured collimator factors and their uncertainties for each diode detector are shown in Figure 5.13. Figure 5.13 clearly shows the persistent difference in measured collimator factor across the three linear accelerators, up to $\pm 3.6\%$ deviation from the mean collimator factor. In all cases, this difference is much greater than the measurement uncertainty. In addition, it can be seen that the collimator factor retains the approximately linear dependence on the field side length.

5.6.6.2. Mini-Beam Relative Output Factors

The mini-beam relative output factors were calculated for each linear accelerator using the measured values for the open field relative output factor and the collimator factor. Figure 5.14 shows the mini-beam relative output factors for each measurement. Due to the increase in relative output factor for larger open fields, the trend in the mini-beam relative output factor with respect to field size is inverted from that of the collimator factor, but remains linear within uncertainty.

With one exception, the relative output factors do not agree to within experimental uncertainty. As well, the measured relative output factors deviate from the mean by up to $\pm 3.4\%$.

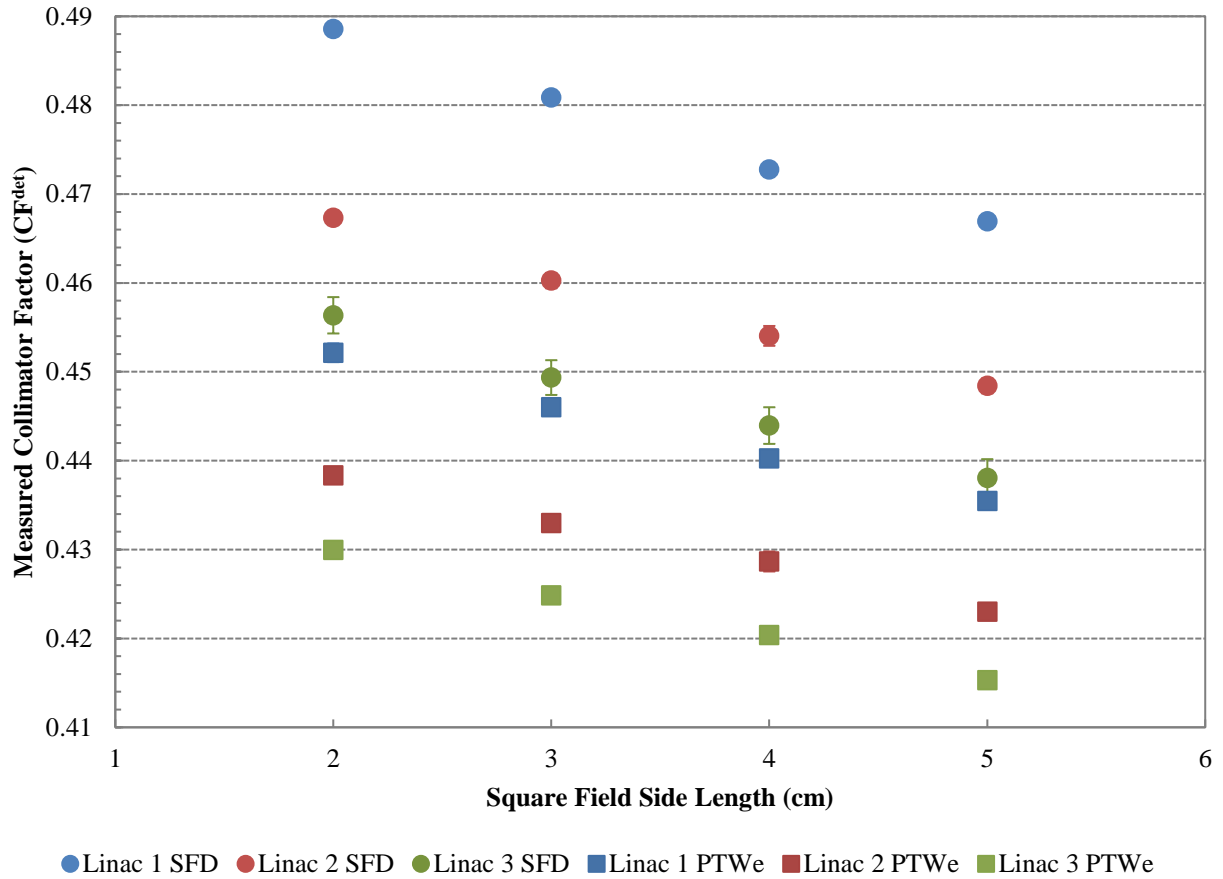


Figure 5.13. Measured collimator factors for each diode detector.

5.7. Discussion

These results reveal several features of the mini-beam collimator which must be considered before clinical use.

5.7.1. Open Field Measurements

The good agreement between the open field measurements for all linear accelerators served to verify the clinical beam matching condition. Therefore, the results of measurements on the different linacs can be compared directly. This finding was expected, but verification was necessary in order to confirm that the mini-beam collimated fields could be directly compared.

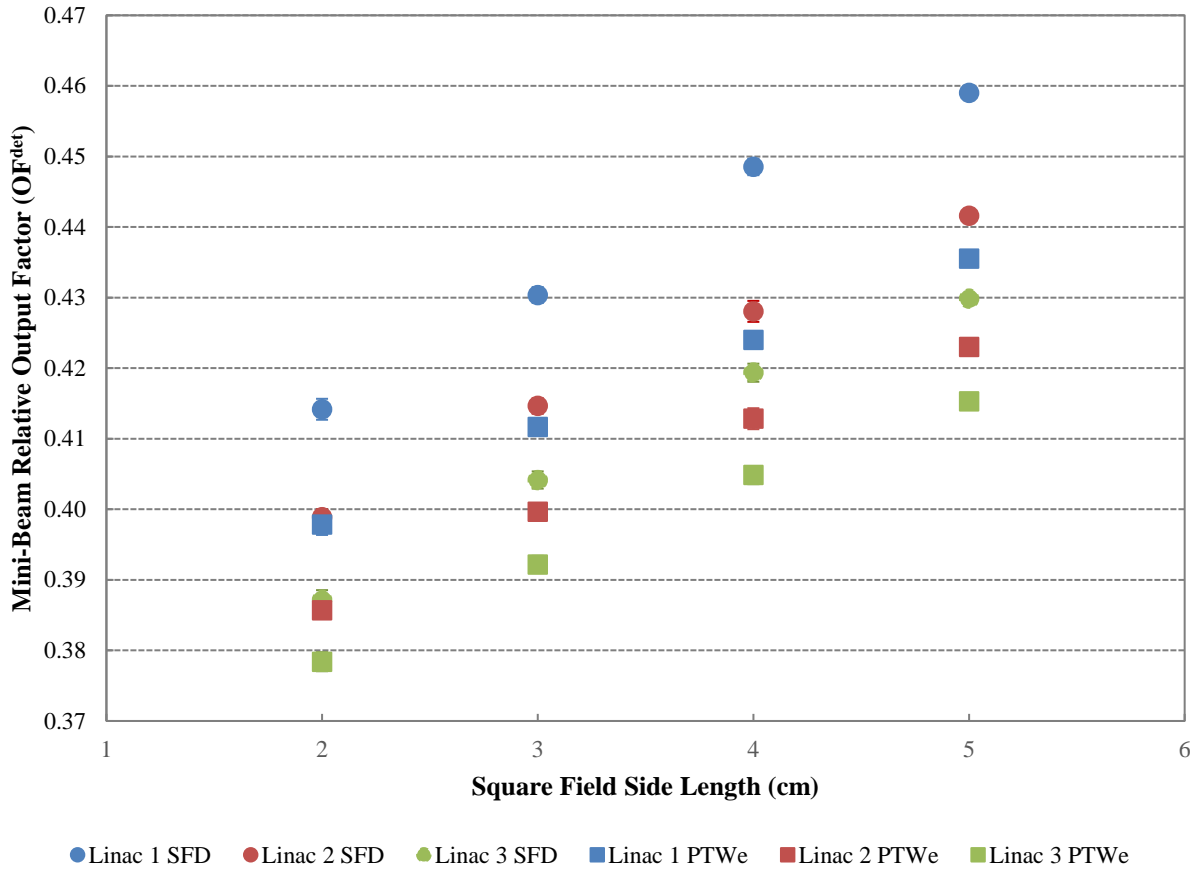


Figure 5.14. Relative output factors of the mini-beam collimated field for each diode detector.

5.7.2. Percent Depth Dose and Dose Profile

Figure 5.8 shows that the beam qualities of the four collimated fields agreed with the open field value within the clinical standard. This was a desirable outcome, as it shows that the energy spectrum of the mini-beams was clinically indistinguishable to that of the open field. This indicates that the mini-beam collimator has little effect on the energy spectrum of the photon beam, and is therefore suitable for the irradiation of targets well below the surface. As such, the mini-beam arrays could be used to deliver doses capable of tumour control to a target volume without delivering prohibitive doses to intervening tissue, one of the key advantages of MV energy MBRT. However, the electron contamination must be planned for to prevent excessive skin dose.

Figure 5.13 and Table 5.6 reveal the existence of differences in the mini-beam collimated fields generated by the three accelerators. This outcome is unfavourable, since clinical differences in the collimated field across linacs may limit or complicate the transferability of the collimator. Due to this effect nominally clinically equivalent fields on different linacs will not deliver equivalent doses when used with the mini-beam collimator. However, the peak dose can be fixed across linacs by varying the duration of the beam. This linac dependence was also observed in the point dose measurements.

5.7.3. Collimator Factors and Relative Output Factors

Figure 5.11 shows the rapid decrease in collimator factor due to small changes in collimator inclination angle with respect to the beam central axis. This indicates that the collimator factor is highly sensitive to the collimator geometry, verifying the expectations from the design process. The collimator factor varied by an amount exceeding the beam matching tolerance in response to a change in inclination of less than the observed change in beam axis inclination across linear accelerators. This effect must be characterized and controlled in order to deliver a consistent dose using the mini-beam collimated field.

However, despite causing clinically significant variation, this effect does not account for the differences in collimator factor obtained on each medical linear accelerator. As can be seen in Figure 5.11 and 5.13, the collimator factor measured with the collimator at 0° alignment varied across linacs by a clinically significant extent. This indicates a difference between the linacs other than variation in beam steering or mechanical differences in the accessory mount.

Another significant result is that the change in collimator factor across linacs follows the same trend as change in PVDR. Equation 5.3 indicates that variation in peak dose would naturally

result in a proportional change in collimator factor. The correlation observed in measurements indicates that the two features may be connected.

It is clear that the mini-beam collimated fields on different linacs are dosimetrically distinct, despite the open fields being clinically beam matched. However, the measured collimator factors for each linac were consistent across multiple experimental setups. The consistency of the measured values and agreement between the corrected values for each individual linac indicate that the variation is a feature of the accelerators, and that proper dosimetric characterization must be pursued to allow for treatment planning and delivery of the mini-beam collimated fields for clinical purposes.

The fact that the collimator factors and PVDR differ to such an extent across linear accelerators was unexpected. The very small scale of the mini-beams appears to reveal differences between the linacs which are not apparent in the open field data. The next stage of the study was to identify the cause of this difference. Direct testing of the suspected causes would have required alteration to the internal settings of the accelerators, requiring that the linacs be removed from clinical use until the commissioning data could be updated. Instead, Monte Carlo simulations, which allowed fine and arbitrary control of the parameters being investigated, were used to test the hypotheses.

CHAPTER 6

COLLIMATOR TRANSFERABILITY:

MONTE CARLO SIMULATIONS

As described in Chapter 4, Monte Carlo simulation can be a powerful tool for the study of radiation in matter. By making use of simulations, it is possible to analyze the output of the collimated field without the mechanical or dosimetric constraints inherent in physical measurements. Furthermore, simulations allow for the adjustment of accelerator settings without interfering with other uses of the accelerator. The freedom to alter internal accelerator settings proved essential to identifying the cause of the disagreement in measured collimator factors.

This chapter will provide a description of the process by which the simulations were performed. The simulation results will be covered and discussed. Finally, the process necessary to convert the measurements into values which can be used for treatment planning will be outlined, and the corrected values presented.

6.1. Simulation Procedure

The Monte Carlo simulations used to test the response to changes in linac parameters were carried out in three stages. Simulations of the linacs were carried out in BEAMnrc to produce the collimated field and open field outputs using a model of a Varian iX medical linear accelerator head used in earlier studies of very small fields [23, 64, 66, 67, 68]. Subsequently, simulations of the resultant beams incident on a water phantom were used to simulate each of the experimental

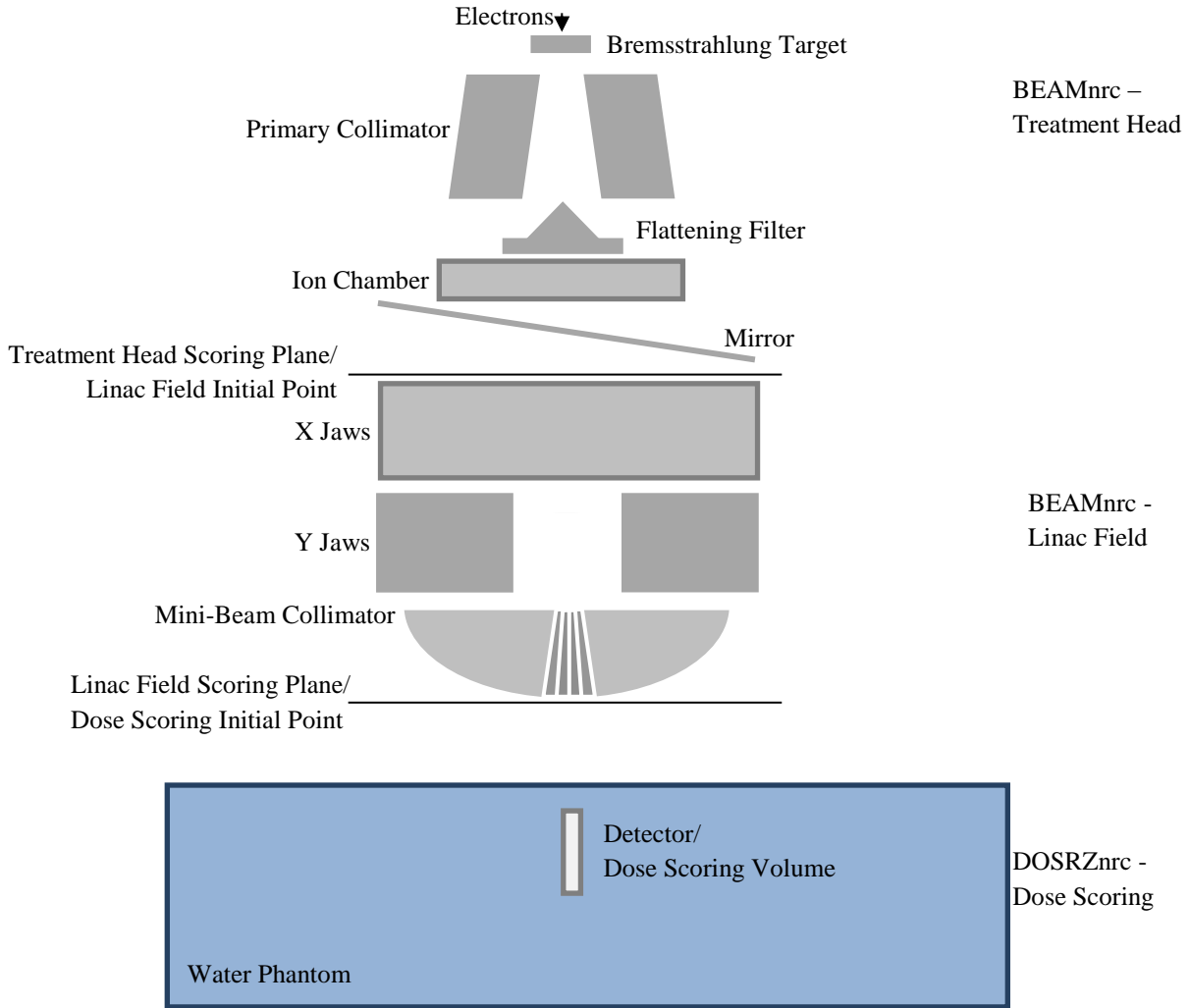


Figure 6.1. The simulated linac. The simulated components and scoring planes for each stage of the simulation are labelled.

measurements. A representation of the simulated linac is depicted in Figure 6.1. An example EGSnrc input file for each stage is provided in the Appendix.

6.1.1. Stage 1: Treatment Head

The first stage in the modelling of the field was the simulation of the electron beam incident on the Bremsstrahlung target and the resultant photon fluence in BEAMnrc. At this step, the

photons are generated by electron interactions with the target and transported through the internal components of the linear accelerator head.

The incident 6.2 MeV electron beam was simulated as a circularly symmetric Gaussian source at the top surface (the surface facing towards the particle source) of the target. Below the target, the primary collimator, flattening filter, monitor unit chamber, and mirror were modelled as component modules. The beam head model used at this step terminated above the jaws, with a scoring plane located at the bottom of the mirror, 26.796 cm below the reference point and 26.8849 cm below the electron source.

1.0×10^8 electrons histories were used to simulate the incident beam. The electrons incident on the target triggered Bremsstrahlung photon showers. Directional Bremsstrahlung splitting was used to improve the efficiency of the simulation. All photons within an 8 cm radius (defined at isocenter) splitting field were split 1000 times. These photons were transported through the geometry of the treatment head to the scoring plane, just above the jaws. The output of the simulation was the state of the particles at the scoring plane as a phase-space.

6.1.2. Stage 2: Linac Field

The next stage in the process was to simulate the field emitted from the medical linear accelerator in BEAMnrc. At this step, the distinction between the mini-beam collimated field and open field simulations was established. Unique inputs were made with and without the collimator to create representations of the mini-beam collimated and open fields.

The phase-space resulting from the Treatment Head simulation was used as the particle source for these simulations. These particles were transported through the jaws to the location of the accessory mount. The field size of the simulation was defined using the jaw position. For each

electron beam FWHM, inputs were made for four field sizes: 2 cm x 2 cm, 3 cm x 3 cm, 4 cm x 4 cm, and 5 cm x 5 cm.

Two inputs were made for each field size combination, one with the mini-beam collimator in place and one without. The collimator was represented using the ARCCHM component module, which was intended for simulation of an arc-chamber attachment having a configuration similar to the collimator [56]. The component module consists of an array of alternating chambers and septa arranged in an arc. The chamber and septa regions are defined by their chamber width and spacing and the front and back radii of the component module. The walls of the component module define the limits of the arc-chamber. A representation of the mini-beam collimator was created by setting the appropriate dimensions to match the collimator design. For the collimated field input, the chambers were set to be tungsten, the walls aluminum, and the septa air. For the open field input the component module was left in place, but all the media were set to be air. This ensured consistency in the geometry of the two simulations.

The inputs called for 4.5×10^8 particle histories from the Stage 1 phase-space. The particles were transported through the jaws and collimator to the scoring plane 75 cm below the reference point. Thus, the phase-space created at the scoring plane serves as a representation of the mini-beam collimated field or open field.

6.1.3. Stage 3: Dose Scoring

The final stage in the process was to simulate the linac output incident on the water phantom and detector. The simulated collimator factor was determined from the results of simulations of the mini-beam collimated and open fields. Thus, four unique simulations were required to obtain the collimator factor for both detectors in a given field.

The DOSRZnrc simulation geometry at this step is a reconstruction of the experimental setup described in Chapter 5. A 25 cm thick region of air is the intervening medium between the initial point of the beam and the simulated phantom. The phantom consists of a region of water containing a model of the detector. The detector is located such that the active volume is at 10 cm depth in the water, as was the case in the experimental setup. The inputs are distinguished by the composition and geometry of the detector and the choice of input phase space. The detector geometry also defined the simulation outputs, the dose deposited in the volume corresponding to the active volume of the detectors being the quantity of interest.

The simulation was set with a target uncertainty of $\pm 0.5\%$ and sufficient histories to satisfy this condition, generally 1.0×10^{10} . The particles in the Linac Field phase space were transported from their start point 25 cm above the water surface to their termination point. Thus, the simulated collimator factor for each detector was obtained from the ratio of the dose deposited by the mini-beam collimated field to the dose deposited by the open field.

DOSXYZnrc simulations were used to investigate the dose distribution of the fields. As with the DOSRZnrc simulations, the simulated media consists of a 25 cm thick layer of air over a homogenous volume of water. The detector was not included in the simulation geometry. The region of interest in the water phantom was created out of voxels with a crossplane width of 0.2 mm, equal to the crossplane resolution of the measured profiles. The inplane and depth resolution were set to 1 mm and 1.5 mm. The reduced resolution in these axes serves to reduce the computational requirements, as the resolution in this axis has minimal effect on the PVDR. 1.3×10^9 particles from the Stage 2 phase space were used to represent the incident beam. Profiles at 10 cm depth in the simulation phantom were constructed from the 3ddose file, and the PVDR was calculated as described by Equation 5.9.

6.2. Parameter Testing

The Monte Carlo simulations were carried out to test the effect of changes to linear accelerator parameters on the mini-beam collimated field so as to identify the cause of the variation described in Chapter 5. Two features of the linacs were identified as plausible causes: the width of the initial electron beam incident on the Bremsstrahlung target and the separation between the source and the accessory mount holding the collimator. Simulations for a range of reasonable values for these parameters were carried out to test these hypotheses.

6.2.1. Electron Beam FWHM

During the commissioning process, it was observed that the width of the initial electron source influenced the simulated collimator factor [23]. The width of the linac electron beam is nominally 1.0 mm, but is difficult to directly measure, and may vary. Thus, it was hypothesized that differences in the width of the electron beam incident on the Bremsstrahlung target within each accelerator was responsible for the variation in PVDR and collimator factor across linacs.

In the open field configuration, small changes in the electron beam FWHM are acceptable. The source may differ in terms of area, but because the entire source is exposed the dose rate remains consistent. However, the spacing of the blades in the collimator is narrower than the projection of the electron source. When the collimator is in place, the source may be partially occluded by the blades, reducing the observable area of the electron. The fraction of the source which is occluded by the collimator blades depends on the width of the electron source. For greater electron beam FWHM, a larger percentage of the source is occluded, leading to a reduction in relative output factor for the mini-beam collimated field.

The electron beam FWHM was manipulated in the first stage of the simulations by changing the FWHM of the electron source in the Stage 1 simulation. The full simulation process was carried out for electron beam FWHMs from 0.7 mm to 1.2 mm at 0.1 mm intervals. As an initial test of the effect, the simulations were carried out for the 4 cm x 4 cm mini-beam collimated field and open field incident on both detectors. Subsequently, additional simulations were carried out for 2 cm x 2 cm, 3 cm x 3 cm, and 5 cm x 5 cm fields incident on both detectors. Finally, DOSXYZnrc simulations of the 4 cm x 4 cm field for each electron beam FWHM were used to construct dose profiles to determine the PVDR of the simulated mini-beam collimated field as a function of FWHM.

6.2.2. Source-to-Collimator Distance

Another feature that may differ across medical linear accelerators is the distance between the beam source and the collimator in the accessory mount. Though this distance is expected to agree between any two linear accelerators to a tolerance of ± 1 mm, wear over the varied service lives of the linacs may induce differences in the accessory mounts.

As described in Section 5.6.4, the mini-beam collimated field is highly sensitive to changes in the blade spacing of the mini-beam collimator. As the collimator was designed such that the blades align to the beam divergence at the height of the accessory mount, raising or lowering the collimator will cause a change in the alignment of the blades relative to the beam divergence.

The collimator height was varied in the Stage 2 simulations by varying the height of the ARCCHM component module in 0.1 cm steps for 0.5 cm above and below the nominal position of 58.9 cm from the source. DOSRZnrc simulations were carried out for the 4 cm x 4 cm field incident on both detectors as a test of the effect.

6.3. Results of Parameter Testing

The hypothesized causes of the discrepancies were tested by studying the relationship between the simulated collimator factor and PVDR and the parameter of interest.

6.3.1. Collimator Factor and PVDR as a Function of Electron Beam FWHM

DOSRZnrc simulations for all field sizes using both detectors were carried out to obtain collimator factors for a range of electron beam widths. The results were observed to cover the range of measured collimator factors obtained by the experimental measurements and shown in Figure 5.14. As such, it was possible to fit the experimental data to the simulation trends in order to determine the electron beam FWHM of each linear accelerator. The eight measured values for each linac were fitted to the interpolated trend between the two nearest simulated collimator factors by the method of least squares regression. The simulated and measured collimator factors are plotted against electron beam FWHM in Figure 6.2. The experimental data can be seen to fit the simulation results within the calculated uncertainty. The electron beam FWHMs obtained from the data are stated in Table 6.1.

DOSXYZnrc simulations served to determine the PVDR as a function of electron beam FWHM. The simulated PVDR for each FWHM are shown in Figure 6.2. As expected, the PVDR decreases with increasing electron beam FWHM. The measured PVDR for each linac (Table 5.5) are shown at the fitted FWHM stated in Table 6.1. All values fit the trend of simulated PVDR within the calculated uncertainty, and agree with the simulated PVDR to within $\pm 1.2\%$ along the trend line obtained by linear interpolation.

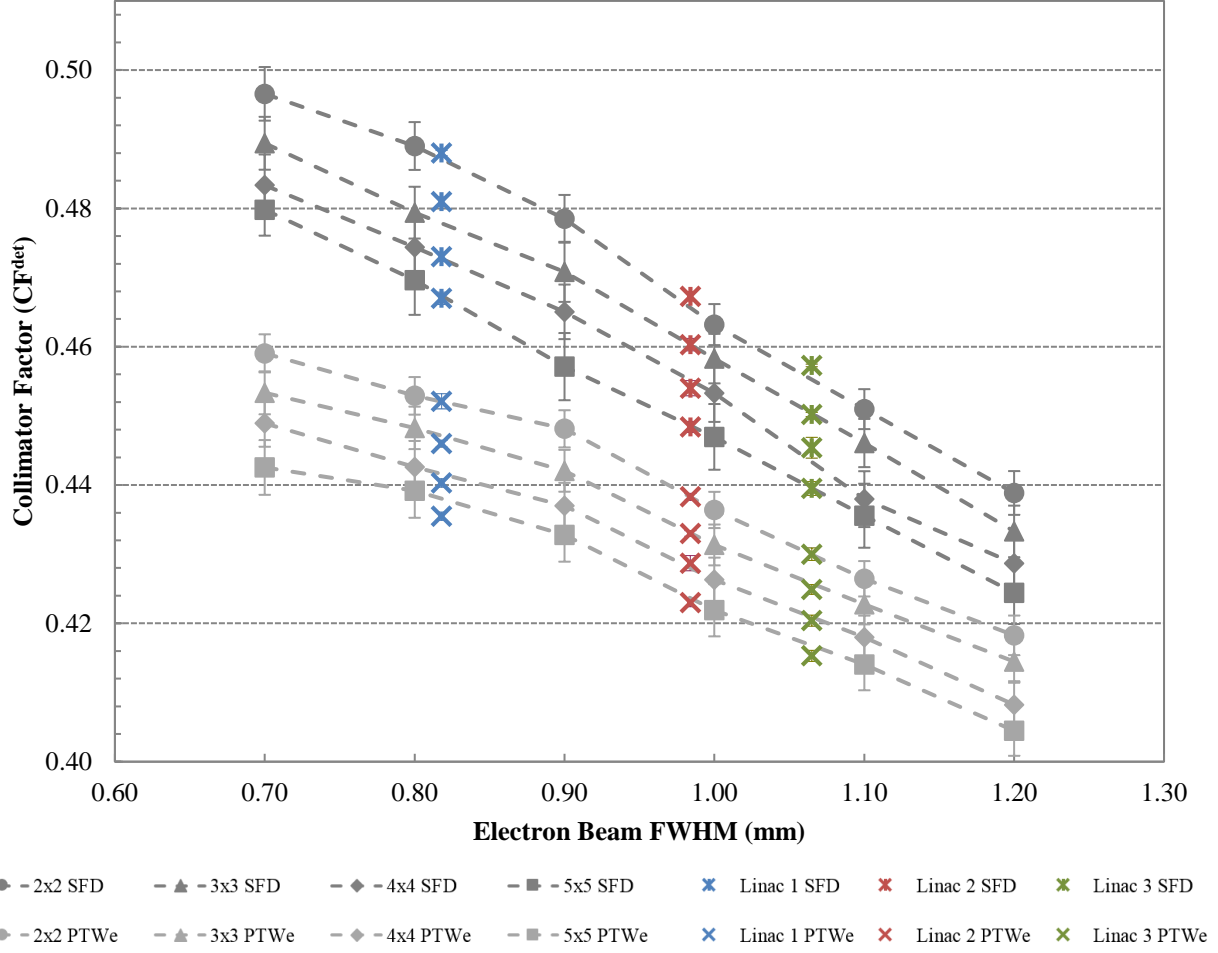


Figure 6.2. Collimator Factors vs Electron Beam FWHM. The measured collimator factors for each detector are shown at fitted linac-specific electron beam FWHM. Simulated collimator factors are shown in gray, and experimental collimator factors are shown in colour.

Linac	Electron Beam FWHM (mm)
1	0.82
2	0.98
3	1.07

Table 6.1. Fitted electron beam FWHMs for Linacs 1-3.

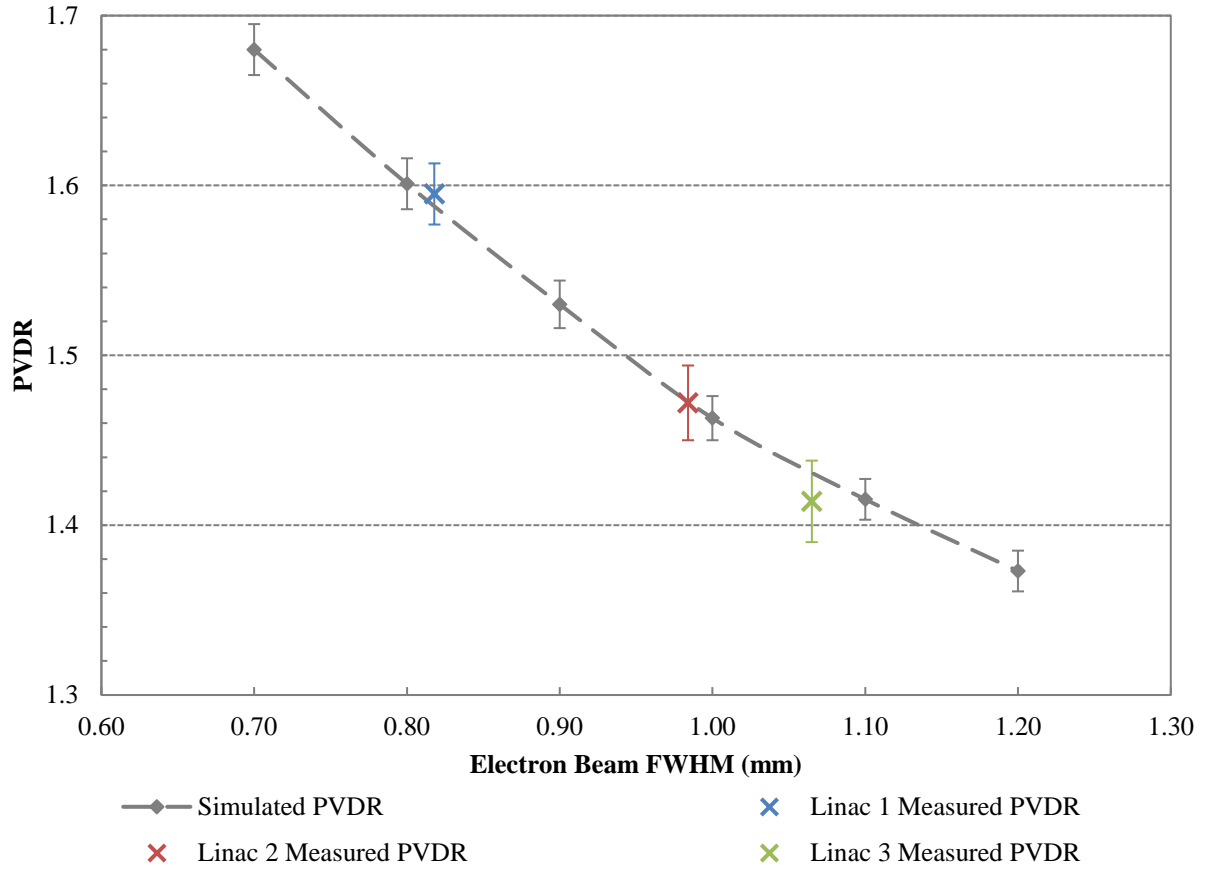


Figure 6.3. PVDR vs Electron Beam FWHM. The measured PVDR for each detector are shown at the previously fitted electron beam FWHM. Simulated PVDR are shown in gray and experimental PVDR are shown in colour.

6.3.2. Collimator Factor as a Function of Source to Collimator Distance

Simulations of the mini-beam collimated field revealed minimal change in the collimator factor as a function of any plausible change in the distance between the Bremsstrahlung target and the mini-beam collimator. Figure 6.4 shows the simulated collimator factors obtained for all collimator to source distances. As can be seen, all simulated collimator factors are equal to within the calculated uncertainty. Thus, the vertical position of the mini-beam collimator has no noticeable effect of the simulated collimator factor.

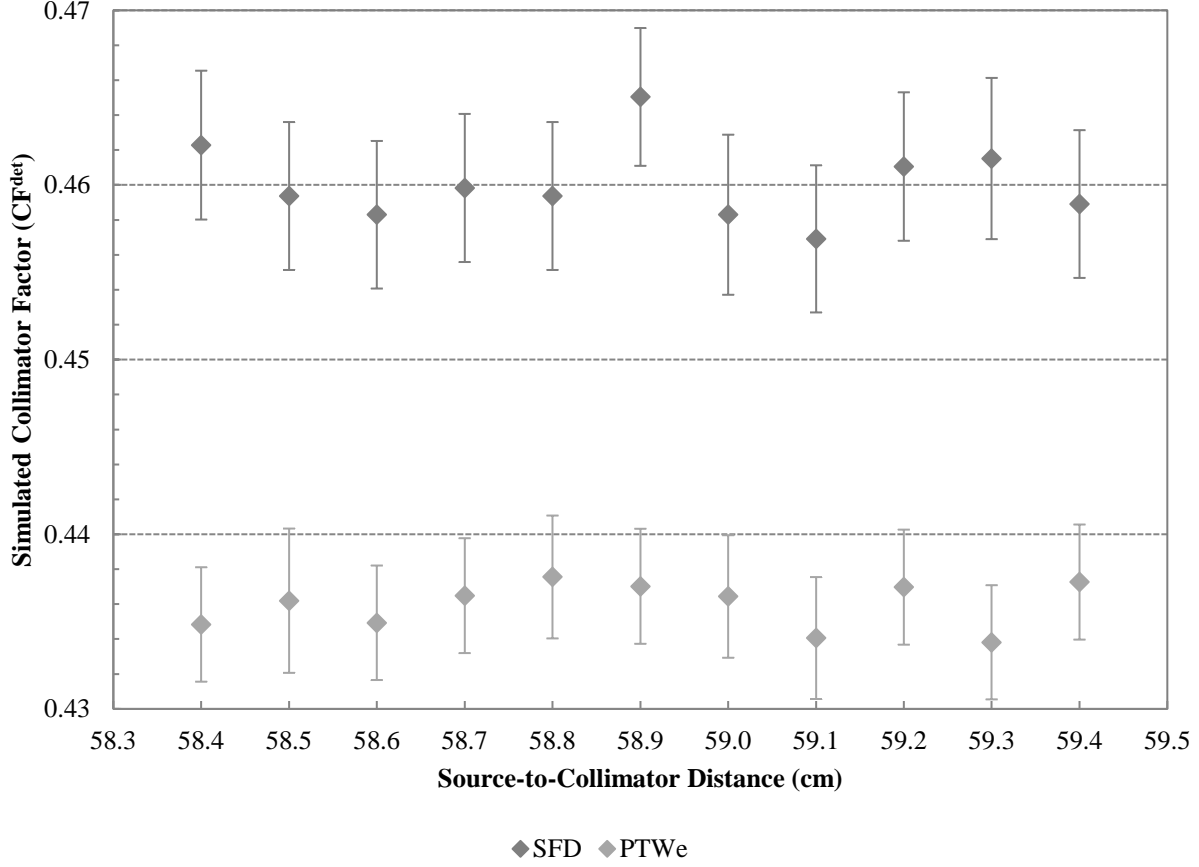


Figure 6.4. Simulated collimator factors versus source-to-collimator distance for a 4 cm x 4 cm field.

6.4. Mini-Beam Correction Factors

High-resolution diode detectors have been shown to over-respond relative to the dose to water in very small fields [67, 69, 70]. A correction must be applied to dose measurements of small fields, such as the mini-beams, in order to account for this effect [71]. When the dose ratios for small fields are calculated, this correction ($k_{f_{mini}}^{det}$) can be applied such that:

$$CF_{f_{mini}}^w = CF_{f_{mini}}^{det} * k_{f_{mini}}^{det}, \quad (6.1)$$

and it follows that Equation 5.2 can be found by:

$$OF_{f_{mini}}^w = OF_{f_{clin}}^w * CF_{f_{mini}}^{det} * k_{f_{mini}}^{det}, \quad (6.2)$$

The correction factors can be calculated by Monte Carlo simulation of the mini-beam collimated field and open field incident on the detector of interest and homogenous water phantom via:

$$k_{f_{mini}}^{det} = \left(\frac{\left(\frac{D_{f_{mini}}^w}{D_{f_{clin}}^w} \right)}{\left(\frac{D_{f_{mini}}^{det}}{D_{f_{clin}}^{det}} \right)} \right)_{MC} . \quad (6.3)$$

The correction factors are dependent on the geometry and composition of the detector. Therefore, different detectors each have different correction factors.

When applying the correction factor to obtain $CF_{f_{mini}}^w$ and $OF_{f_{mini}}^w$, Equations 5.10 and 5.11 can be rewritten to account for the uncertainty in the correction, such that:

$$u_{CF_{f_{mini}}^w} = \sqrt{\left(u_{CF_{f_{clin}}^{det}}\right)^2 + \left(u_{k_{f_{mini}}^{det}}\right)^2} \quad (6.4)$$

and

$$u_{OF_{f_{mini}}^w} = \sqrt{\left(u_{OF_{f_{clin}}^{det}}\right)^2 + \left(u_{CF_{f_{mini}}^{det}}\right)^2 + \left(u_{k_{f_{mini}}^{det}}\right)^2} . \quad (6.5)$$

6.4.1. Calculation

As described in Equation 6.3, a correction for the effects of the detector geometry can be determined using Monte Carlo simulation of the mini-beam collimated field. Four values were necessary to obtain each correction factor: the DOSRZnrc outputs for both the mini-beam collimated and open fields incident on a water phantom with and without the detector. A unique correction factor was calculated for each field and electron beam FWHM. After the variation across linacs was linked to electron beam FWHM, simulations using the linac specific FWHM

	Linac 1		Linac 2		Linac 3	
Field (cm ²)	PTWe	SFD	PTWe	SFD	PTWe	SFD
5 x 5	1.054 ± 0.008	0.984 ± 0.008	1.044 ± 0.008	0.986 ± 0.008	1.035 ± 0.005	0.982 ± 0.006
4 x 4	1.060 ± 0.007	0.986 ± 0.007	1.039 ± 0.007	0.978 ± 0.008	1.038 ± 0.006	0.981 ± 0.006
3 x 3	1.050 ± 0.006	0.976 ± 0.007	1.042 ± 0.006	0.984 ± 0.006	1.035 ± 0.005	0.979 ± 0.006
2 x 2	1.053 ± 0.005	0.978 ± 0.006	1.046 ± 0.005	0.986 ± 0.007	1.035 ± 0.005	0.975 ± 0.005

Table 6.2. Linac-specific correction factors with calculated uncertainty for each field and detector.

were carried out to obtain dose to water for each linac. The correction factors, stated in Table 6.2, were calculated via simulation of the fields generated for the FWHM stated in Table 6.1. Note that the PTWe correction is consistently greater than 1, while the SFD correction factor is consistently less than 1. This shows that the PTWe under-responds to the mini-beam collimated field, despite the diode detector over-response in very small fields. As with the previous difference between the PTWe and SFD, this is a result of the greater diameter of the PTWe active volume.

6.4.2. Corrected Collimator Factors

The $k_{f_{mini}}^{det}$ were applied to the measured collimator factors from Figure 5.13 to obtain the collimator factors in water. Figure 6.5 shows the collimator factors in water for each linear accelerator. The correction factors eliminate the difference between the measured collimator factors for each detector, bringing the measurements for each linac into agreement within the calculated uncertainty. The corrected collimator factors for certain fields show agreement within experimental uncertainty (e.g. 3 cm x 3 cm for Linacs 2 and 3).

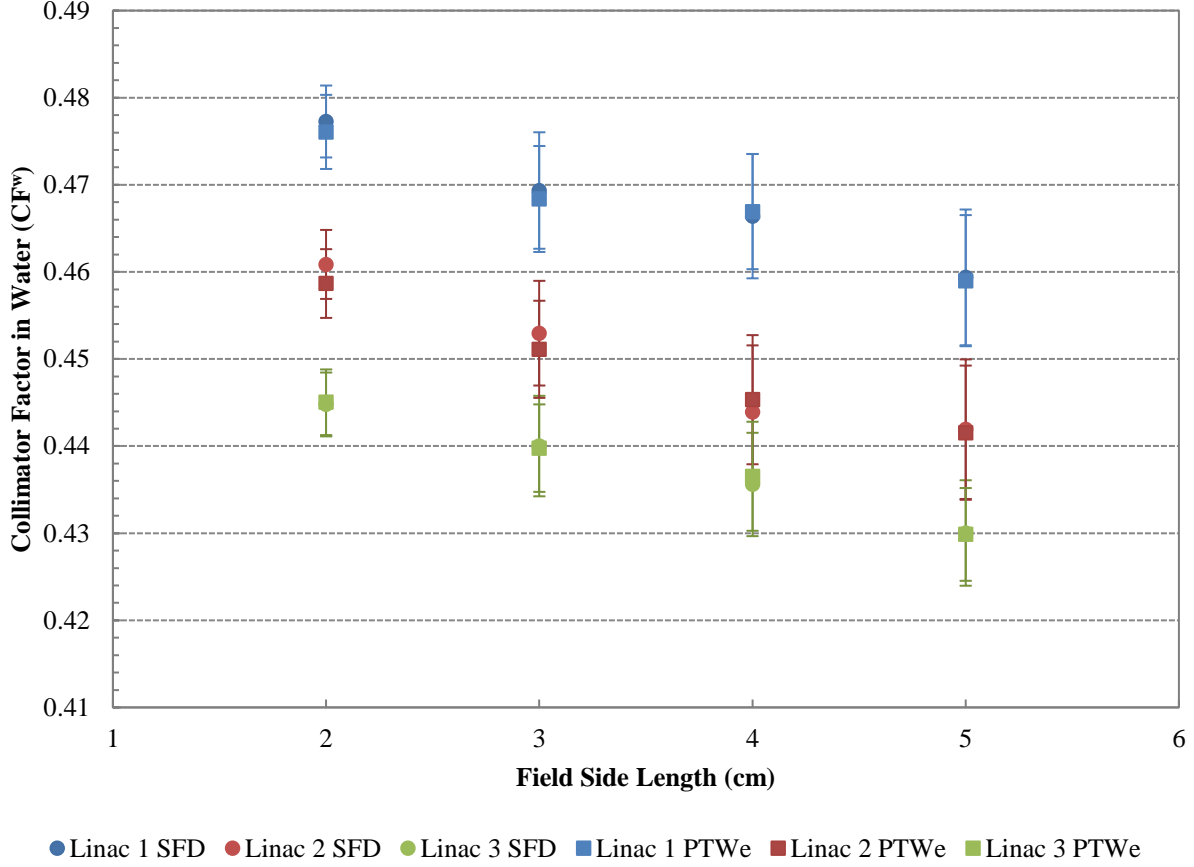


Figure 6.5. Collimator factors in water ($CF_{f_{mini}}^w$) for each linear accelerator.

6.4.3. Corrected Mini-Beam Relative Output Factors

The collimator factors in water were used to calculate the mini-beam relative output in water. These corrected relative output factors are shown in Figure 6.6. $CF_{f_{mini}(5 \times 5)}^w$ is equal to $OF_{f_{mini}(5 \times 5)}^w$ for all linacs because the 5 cm x 5 cm field was used as the reference field.

The relative output factors in water for each detector agree within experimental uncertainty. Once again, agreement between some values on different linacs can be observed, but no two linacs agree within the calculated uncertainty for all fields.

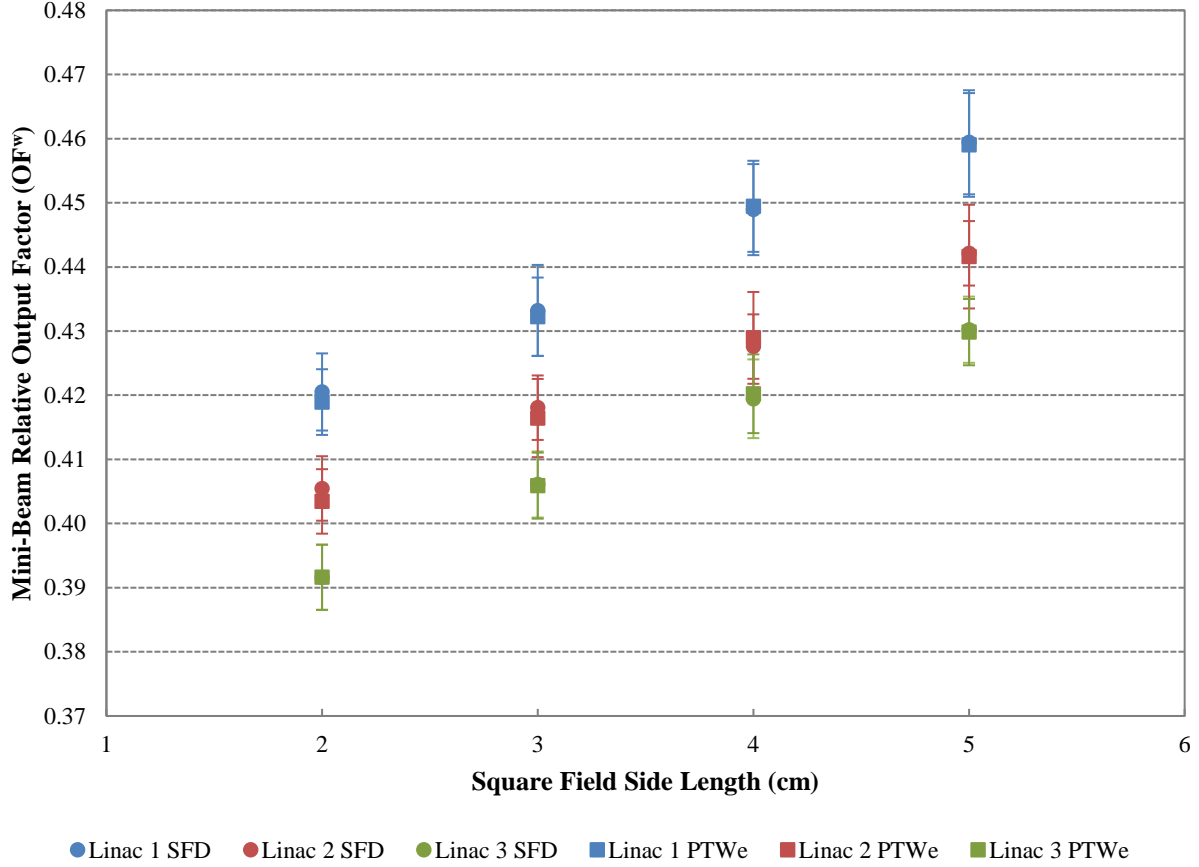


Figure 6.6. Mini-beam relative output factors in water ($OF_{f_{mini}}^w$) for each diode detector.

6.5. Discussion

The Monte Carlo simulations offered greater insight into the factors influencing the mini-beam collimated field.

6.5.1. Parameter Testing

The simulations strongly indicate that the discrepancies between the mini-beam collimated fields are linked to variation in the FWHM of the linac electron beam incident on the Bremsstrahlung target. The experimental results were successfully fitted to simulated collimator factors. With few exceptions, the measured collimator factors show agreement with the simulated

	Linac 1		Linac 2		Linac 3	
Field (cm ²)	CF _{mini} ^w	OF _{f_{mini}} ^w	CF _{mini} ^w	OF _{f_{mini}} ^w	CF _{mini} ^w	OF _{f_{mini}} ^w
5 x 5	0.459 ± 0.010	0.459 ± 0.012	0.442 ± 0.011	0.442 ± 0.010	0.430 ± 0.008	0.430 ± 0.007
4 x 4	0.467 ± 0.010	0.449 ± 0.010	0.445 ± 0.011	0.428 ± 0.009	0.436 ± 0.009	0.420 ± 0.009
3 x 3	0.469 ± 0.009	0.433 ± 0.009	0.452 ± 0.009	0.417 ± 0.008	0.440 ± 0.008	0.406 ± 0.008
2 x 2	0.477 ± 0.008	0.420 ± 0.008	0.459 ± 0.009	0.405 ± 0.007	0.445 ± 0.007	0.392 ± 0.007

Table 6.3. Average corrected collimator factors and mini-beam relative output factors with calculated uncertainties for each linac.

trends within measurement uncertainty, and all measured collimator factors agreed with the simulated trends within the interpolated simulation uncertainty. Similarly, the measured PVDR were in agreement with the trend of simulated PVDR. Thus, the established Monte Carlo model of the linear accelerator can be matched to any particular characterized linac by setting the initial electron beam FWHM appropriately.

The collimator factor was found to be insensitive to variation in source-to-collimator distance over a 5 mm in either direction from the nominal distance. Any change of this magnitude due to the accessory mount position would be detected during annual inspection of the isocenter position, being five times greater than the TG-142 tolerance [62].

6.5.2. Corrected Collimator Factors and Relative Output Factors

The diode correction factors brought the measured collimator factor and mini-beam relative output factor for each linear accelerator into agreement. Due to the agreement within uncertainty of the corrected values, the average of the two detector-measured values for each field can be taken to give a single value. The averages are stated in Table 6.3. The calculated uncertainties of all

values are less than 3.0%, sufficient for clinical repeatability. These average corrected values can be used as the primary characterization metric of the mini-beam collimated field on the different linear accelerators. Furthermore, the effectiveness of the correction factors serves as additional verification of the accuracy of the model, as it produced valid correction factors over a range of initial parameters.

The results of the Monte Carlo simulations provide an explanation for the variation observed in the experimental measurements. Though the characterization metrics for individual linacs do not agree within the beam matching criterion, the simulations show that this discrepancy stems from a feature of the linacs, and can be expected to remain consistent over time. Thus, use of the mini-beam collimator will produce a consistent field.

CHAPTER 7

CONCLUSION

A mini-beam collimator intended to deliver high-energy mini-beam radiotherapy using standard medical linear accelerators has been developed by a group at the Saskatoon Cancer Centre. The goal of this work was the dosimetric characterization of the mini-beam collimator on multiple beam matched medical linear accelerators. Experimental measurements and Monte Carlo simulations were used to accomplish this goal.

7.1. Transferability

The experimental characterization of the mini-beam collimated field involved measurements of percent depth dose curves, dose profiles, and dose to a reference point at 10 cm depth in water. Two diode detectors were used in the measurements. The measurements were performed on three clinically beam matched medical linear accelerators using the 6 MV beam energy. Corresponding measurements of the open field verified the beam matching criteria and provided a reference point for comparison with the mini-beam collimated field.

%DD measurements were performed on all three linacs. All results showed close agreement in both $\%DD(10\text{ cm})$ and d_{max} . As well, the results were consistent with the measurements of the open field. These results show that the mini-beam collimator has minimal impact of the energy spectrum of the field, such that the nominal energy of each mini-beam remains equivalent to that of the open field. Thus, the mini-beams exhibit the same attenuation characteristics.

Crossplane dose profiles of the mini-beam collimated field were measured for all three linacs. The PVDR varied to a clinically significant degree across linacs. A linac dependence was also observed in the collimator factor, calculated from the point doses obtained in the mini-beam collimated field and open field. The collimator factors on each linac were proportional to the PVDR, suggesting that they stem from the same root cause. This difference between linear accelerators complicates the use of the mini-beam collimator, necessitating the full characterization of the mini-beam collimated field on each linac before use.

However, while the PVDR and magnitude of the collimator factor varied across linacs, several other features were found to be linac-independent. The effect of changes in all controllable parameters, most notably field size, on the mini-beam collimated field to was consistent across linacs. Thus, the mini-beam collimated field delivered on each linac remains consistent across multiple experimental sessions.

A feature that must be noted when setting the mini-beam collimator is the collimator inclination angle relative to the beam central axis. The mini-beam collimated field shows a strong dependence on collimator inclination. There exists a narrow range where the collimator factor remains constant before rapidly decreasing with increased deviation from the optimum inclination angle. This dependence on collimator inclination angle must be accounted for when transferring the mini-beam collimator between linacs.

EGSnrc modelling of the mini-beam collimated field was used to identify the cause of the variation observed in the experimental results. BEAMnrc simulations were used to generate phase spaces representing a field corresponding to each set of linac parameters. DOSRZnrc simulations were used to calculate the collimator factor for each detector in each field for a range of electron beam FWHM. Similarly, DOSXYZnrc simulations were used to determine the PVDR as a

function of electron beam width. The results showed that variation in the FWHM of the linac electron beam could account for the observed variation in collimator factor and PVDR.

By fitting the measured collimator factors to the simulated values, electron beam FWHM for each linac were predicted. Correction factors to eliminate detector specific effects in the measured collimator factors were calculated for each electron beam FWHM by taking the ratio of the simulated collimator factor in water to that in the detector. Applying these correction factors to the measured values eliminated the discrepancy introduced by the detector small field effects. Thus, a single collimator factor for each linac and field was obtained. The efficacy of these correction factors serves to validate the mini-beam collimated field models.

With the mini-beam collimated field characterized and the EGSnrc model validated, the mini-beam collimator may be utilized in the same way as any linac accessory. It is now possible to establish a procedure for characterization of the mini-beam collimator.

7.2. Recommended Procedure for Characterization

While the mini-beam collimated field for each linac is consistent when properly used, thorough characterization is necessary due to the differences between linacs. The following procedure is based on the experience gained from this transferability study.

First, a baseline lateral position and inclination angle for the collimator must be set. This setting must be carried out with the collimator mounted on a linac, because inserting or removing the collimator from the accessory mount influences the micrometer reading. The collimator should be returned to this position when not is use on another linac.

After the baseline setting is established, the next step is determining the proper collimator position on the new linac. The mini-beam collimator should first be centered in the field, followed

by aligning the collimator inclination to the beam central axis. The process for these adjustments are described in Section 5.3.3 and Section 5.3.4, respectively. The initial and final positions measured by the micrometer for each of these steps must be recorded. These offsets will be used to set the collimator position for the linac in the future.

With the collimator aligned, measurements of the collimator factor must be carried out as described in Section 5.5. The measured collimator factors should then be fitted to a range of simulated collimator factors for the detector used in commissioning to determine the linac electron beam FWHM. A BEAMnrc simulation input using this electron beam FWHM should then be made for planning purposes.

Regular quality assurance must be used to ensure the positional settings of the mini-beam collimator do not change in the course of use. Unlike the full characterization, this does not necessarily require the precision of the water phantom; any test apparatus (e.g. solid water) with a previously determined response can be used. If the dose to the reference point in the mini-beam collimated field agrees with the nominal value within clinical requirements, the mini-beam collimator settings for that linac remain valid. Any significant reduction in this dose is cause to repeat the alignment procedure for the collimator. In this event, the mini-beam collimated field on all linacs must be checked for agreement before further use of the collimator.

In addition, the characterization measurements must be repeated periodically to obtain up-to-date micrometer readings. These measurements could be integrated into an annual QA procedure.

7.3. Related Work

While the collimated field has been shown to be reliable, it will not be adopted for clinical use unless the clinical benefits can be verified. With the dosimetric characterization of the mini-beam collimated field complete, other studies are being carried out to examine biological response to the mini-beam collimated field.

A study of the response of cells to mini-beam and open field radiation is being carried out in conjunction with the University of Saskatchewan Cancer Cluster [72]. This work will serve to assess the radiobiology of MV energy MBRT. Irradiation of two glioblastoma cell lines and a control cell line are being used to examine the radiation effects as a function of both dose and time is being carried out. Cell survival fractions as a function of dose and of time were obtained, and occurrences of the modes of radiation damage (e.g. apoptosis, nuclear damage) are being investigated.

A study of the efficacy of mini-beam treatments of canines is being carried out with the Western College of Veterinary Medicine [73]. Sixteen dogs with spontaneous brain tumours are selected from the available patients and randomly assigned treatment with conventional radiotherapy or MBRT. The health of the dogs is tracked for the remainder of their lives. After the patient dies, post-mortem analysis of the irradiated regions will be carried out to examine the brain for signs of radiation damage.

A collimator accessory which allows the delivery of spatially-fractionated mini-beam treatment was developed by a group at the Saskatoon Cancer Centre. The mini-beam collimator has been dosimetrically characterized on three beam matched linear accelerators. Dosimetric differences between the mini-beam collimated fields delivered on each linac were observed. By

varying the parameters of an EGSnrc model of the collimated field, these differences were traced back to variation in the FWHM of the electron beam incident on the Bremsstrahlung target. This finding is a step towards the planning of mini-beam collimated fields across multiple linacs, and forms a basis for expanded use of the mini-beam collimator. Thus, transferability of the mini-beam collimator can be attained by the thorough dosimetric characterization of the mini-beam collimated field.

APPENDIX A

EXAMPLE EGSnrc INPUT FILES

Examples of the input files used for each step of the simulation process (described in Chapter 6) are provided here. Significant lines or sections are indicated by bold font.

A.1. BEAMnrc Input for the Treatment Head

The input at this stage served to create the photons that constitute the beam. Note Line 6 of the input, which specifies the source. The simulation calls an elliptical (ISOURCE = 19) electron (IQIN = -1) source with a Gaussian FWHM of 0.09 cm (RBEAM = -0.09) and zero eccentricity (RBEAMY = 0). The number of photons generated by electron interactions with the target is increased via the use of Directional Bremsstrahlung splitting (DBS). The DBS options are specified in Line 5. As well, Line 4 specifies the number of histories and RNG seeds, and Line 8 specifies the initial energy of the electrons. The simulation geometry is defined in the subsequent Component Modules. Line 11 specifies that particles be scored to the phase space below the sixth component module, MIRROR. The transport settings are specified following the component modules [56].

```

AIR521ICRU
0, 0, 0, 0, 0, 1, 0, IWATCH ETC.
100000000, 33, 97, 999, 2, 1000, 0, 0, NCASE ETC.
8, 100, 0, 20, 1, 12.7, DIRECTIONAL BREM OPTIONS
-1, 19, -0.09, 0, 0, 0, 0.0, -, 0.0, 0.0, IQIN, ISOURCE + OPTIONS
0, MONOENERGETIC
6.2
0, 0, 0.521, 0.01, 0, 0, , 0, ECUT, PCUT, IREJCT, ESAVE
0, 0, 0, 0, 0, PHOTON FORCING
1, 6, SCORING INPUT
0, 1
0, DOSE COMPONENTS
-0.0889, Z TO FRONT FACE
***** start of CM SLABS with identifier target *****
10, RMAX
Target
2, NSLABS
-0.0889, ZMIN
0.0889, 0, 0, 0, 1, -1
W521ICRU
0.1575, 0, 0, 0, 2, -1
CU521ICRU
***** start of CM CONS3R with identifier pri_coll *****
10, RMAX
pri_coll
0.1575, ZMIN
7.3725, ZTHICK
4, NUM_NODE
0.1575, 2.5,
1.54, 2.5,
1.54, 0.613,
7.53, 2.09,
0, 0, 0, 3, -1,
VACUUM
0, 0, 0, 4, -1,
WLIGHT
***** start of CM SLABS with identifier be_win *****
10, RMAX
AIR GAP
2, NSLABS
7.53, ZMIN
0.94, 0.521, 0.01, 0, 5, 0
VACUUM
0.0254, 0.521, 0.01, 0, 6, 0

```


BE521ICRU

***** start of CM FLATFILT with identifier fla_filt *****

10, RMAX

FLATFILT

10.485, ZMIN

19, NUMBER OF LAYERS

1, 0.028, # CONES, ZTHICK OF LAYER 1

0.0,

0.064,

1, 0.028, # CONES, ZTHICK OF LAYER 2

0.064,

0.127,

1, 0.038, # CONES, ZTHICK OF LAYER 3

0.127,

0.191,

1, 0.041, # CONES, ZTHICK OF LAYER 4

0.191,

0.254,

1, 0.074, # CONES, ZTHICK OF LAYER 5

0.254,

0.381,

1, 0.1535, # CONES, ZTHICK OF LAYER 6

0.381,

0.508,

1, 0.1235, # CONES, ZTHICK OF LAYER 7

0.508,

0.635,

1, 0.1235, # CONES, ZTHICK OF LAYER 8

0.635,

0.762,

1, 0.1235, # CONES, ZTHICK OF LAYER 9

0.762,

0.889,

1, 0.1135, # CONES, ZTHICK OF LAYER 10

0.889,

1.016,

1, 0.2235, # CONES, ZTHICK OF LAYER 11

1.016,

1.27,

1, 0.2035, # CONES, ZTHICK OF LAYER 12

1.27,

1.524,

1, 0.2035, # CONES, ZTHICK OF LAYER 13

1.524,

1.778,

1, 0.1835, # CONES, ZTHICK OF LAYER 14

1.778,
 2.032,
 1, 0.1735, # CONES, ZTHICK OF LAYER 15
 2.032,
 2.286,
 1, 0.142, # CONES, ZTHICK OF LAYER 16
 2.286,
 2.54,
 1, 0.13, # CONES, ZTHICK OF LAYER 17
 2.54,
 2.794,
 3, 0.097, # CONES, ZTHICK OF LAYER 18
 2.794, 3.366, 3.81,
 3.061, 3.302, 3.81,
 1, 0.165, # CONES, ZTHICK OF LAYER 19
 3.81,
 3.81,
 0, 0, 0, 7,
 CU521ICRU
 0, 0, 0, 8,
 AIR521ICRU
 0, 0, 0, 7,
 CU521ICRU
 0, 0, 0, 8,
 AIR521ICRU
 0, 0, 0, 7,
 CU521ICRU
 0, 0, 0, 8,
 AIR521ICRU
 0, 0, 0, 7,
 CU521ICRU
 0, 0, 0, 8,
 AIR521ICRU
 0.521, 0.01, 0, 7,
 CU521ICRU
 0.521, 0.01, 0, 8,
 AIR521ICRU
 0, 0, 0, 7,
 CU521ICRU
 0, 0, 0, 8,
 AIR521ICRU
 0, 0, 0, 7,
 CU521ICRU
 0, 0, 0, 8,
 AIR521ICRU
 0, 0.01, 0, 7,

CU521ICRU
0, 0.01, 0, 8,
AIR521ICRU
0, 0.01, 0, 7,
CU521ICRU
0, 0.01, 0, 8,
AIR521ICRU
0, 0.01, 0, 7,
CU521ICRU
0, 0.01, 0, 8,
AIR521ICRU
0.521, 0.01, 0, 7,
CU521ICRU
0.521, 0.01, 0, 8,
AIR521ICRU
0, 0.01, 0, 7,
CU521ICRU
0, 0.01, 0, 8,
AIR521ICRU
0, 0.01, 0, 7,
CU521ICRU
0, 0.01, 0, 8,
AIR521ICRU
0, 0.01, 0, 7,
CU521ICRU
0, 0.01, 0, 8,
AIR521ICRU
0, 0.01, 0, 7,
CU521ICRU
0, 0.01, 0, 8,
AIR521ICRU
0.521, 0.01, 0, 7,
CU521ICRU
0.521, 0.01, 0, 8,
AIR521ICRU
0.521, 0.01, 0, 7,
CU521ICRU
0.521, 0.01, 0, 8,
AIR521ICRU
0, 0.01, 0, 7,
CU521ICRU
0, 0.01, 0, 7,
AIR521ICRU
0, 0.01, 0, 7,
CU521ICRU
0, 0, 0, 8,

```

AIR521ICRU
0, 0.01, 0, 7,
CU521ICRU
0, 0.01, 0, 8,
AIR521ICRU
***** start of CM CHAMBER with identifier ion_cham *****
10, RMAX
Ion Chamber
14.2, ZMIN
0, 15, 0, N_TOP, N_CHM, N_BOT
4.7625, 4.7752, 4.95, RADII FOR CENTRAL PART
0.629, 0, ZTHICK, FLAG FOR LAYER 1 IN CENTRAL PART
0, 0.01, 0, 0,
AIR521ICRU
0.0127, 0, ZTHICK, FLAG FOR LAYER 2 IN CENTRAL PART
0, 0.01, 0, 0,
KAPTON521ICRU
0.229, 0, ZTHICK, FLAG FOR LAYER 3 IN CENTRAL PART
0, 0, 1, 0,
AIR521ICRU
0.0051, 0, ZTHICK, FLAG FOR LAYER 4 IN CENTRAL PART
0.521, 0.01, 0, 0,
KAPTON521ICRU
0.234, 0, ZTHICK, FLAG FOR LAYER 5 IN CENTRAL PART
0, 0, 2, 0,
AIR521ICRU
0.0051, 0, ZTHICK, FLAG FOR LAYER 6 IN CENTRAL PART
0, 0, 0, 0,
KAPTON521ICRU
0.229, 0, ZTHICK, FLAG FOR LAYER 7 IN CENTRAL PART
0.521, 0.01, 3, 0,
AIR521ICRU
0.0127, 0, ZTHICK, FLAG FOR LAYER 8 IN CENTRAL PART
0.521, 0.01, 0, 0,
KAPTON521ICRU
0.299, 0, ZTHICK, FLAG FOR LAYER 9 IN CENTRAL PART
0.521, 0.01, 4, 0,
AIR521ICRU
0.0051, 0, ZTHICK, FLAG FOR LAYER 10 IN CENTRAL PART
0.521, 0.01, 0, 0,
KAPTON521ICRU
0.233, 0, ZTHICK, FLAG FOR LAYER 11 IN CENTRAL PART
0.521, 0.01, 5, 0,
AIR521ICRU
0.0051, 0, ZTHICK, FLAG FOR LAYER 12 IN CENTRAL PART
0.521, 0.01, 0, 0,

```

```

KAPTON521ICRU
0.23, 0, ZTHICK, FLAG FOR LAYER 13 IN CENTRAL PART
0.521, 0.01, 6, 0,
AIR521ICRU
0.0127, 0, ZTHICK, FLAG FOR LAYER 14 IN CENTRAL PART
0.521, 0.01, 0, 0,
KAPTON521ICRU
0.628, 0, ZTHICK, FLAG FOR LAYER 15 IN CENTRAL PART
0.521, 0.01, 0, 0,
AIR521ICRU
0.521, 0.01, 0, 9,  chamber wall
AIR521ICRU
0.521, 0.01, 0, 10,  gap
AIR521ICRU
0.521, 0.01, 0, 11,  container
AIR521ICRU
0, MRNGE
***** start of CM MIRROR with identifier mirror *****
10, RMAX
MIRROR
18.873, 7.923, ZMIN, ZTHICK
4.67, -6.645, XFMIN, XBMIN
1, # LAYERS
0.00508, thickness of layer 1
0.521, 0.01, 0, 12,
MYLAR521ICRU
0.521, 0.01, 0, 13,
AIR521ICRU
0.521, 0.01, 0, 14,
AIR521ICRU
*****end of all CMs*****
#####
:Start MC Transport Parameter:

Global ECUT= 0.521
Global PCUT= 0.01
Global SMAX= 5
ESTEPE= 0.25
XIMAX= 0.5
Boundary crossing algorithm= PRESTA-I
Skin depth for BCA= 0
Electron-step algorithm= PRESTA-II
Spin effects= On
Brems angular sampling= Simple
Brems cross sections= BH
Bound Compton scattering= Norej

```

Compton cross sections= default
Pair angular sampling= Simple
Pair cross sections= BH
Photoelectron angular sampling= Off
Rayleigh scattering= Off
Atomic relaxations= On
Electron impact ionization= Off
Photon cross sections= si
Photon cross-sections output= Off

:Stop MC Transport Parameter:

#####

:Start DBS rejection plane:

Use a rejection plane= On

Z(cm) from zero reference plane= 26.78

:Stop DBS rejection plane:

#####

A.2. BEAMnrc Input for the Linac Field

The input at this stage transported the Bremsstrahlung photons through the jaws and mini-beam collimator. The simulation parameters are defined in the same way as in the first stage. At this stage, particles are called from the phase space file generated in the first stage instead of being produced on demand (ISOURCE = 21). DBS is not used in this simulation. The X and Y settings of CM JAWS define the field. CM ARCCHM represents the mini-beam collimator, with the chambers (CHM) corresponding to the blades and the septa (SEP) to the air gaps [56]. Note that the MIRROR and CHAMBER component modules are included in this simulation geometry to account for backscatter within the treatment head. This input is for a mini-beam collimated field, and includes the aluminum (AL521ICRU) and tungsten (W521ICRU) components. These components are set as air (AIR521ICRU) for the open field input. The scoring plane is below the ARCCHM module

Minibeam with Jaws, correlated to measurements

#!/GUI1.0

AIR521ICRU

0, 0, 0, 0, 0, 1, 0, IWATCH ETC.

452302612, 33, 97, 99, 0, 0, 0, 0, NCASE ETC.

9, 21, 3, 0, 0, 0, 0, 0, 0, IQIN, ISOURCE + OPTIONS

../BEAM_varian_6x_above_jaws/0_090eSource_SYMM.egsphsp1

0, 0, 0.521, 0.01, 0, 0, , 0, ECUT, PCUT, IREJCT, ESAVE

0, 0, 0, 0, 0, PHOTON FORCING

1, 4, SCORING INPUT

0, 1

0, DOSE COMPONENTS

12.853, Z TO FRONT FACE

***** start of CM CHAMBER with identifier ion_cham *****

10, RMAX

Ion Chamber

14.2, ZMIN

0, 15, 0, N_TOP, N_CHM, N_BOT

4.7625, 4.7752, 4.95, RADII FOR CENTRAL PART

0.629, 0, ZTHICK, FLAG FOR LAYER 1 IN CENTRAL PART

0, 0.01, 0, 0,

AIR521ICRU

0.0127, 0, ZTHICK, FLAG FOR LAYER 2 IN CENTRAL PART

0, 0.01, 0, 0,

KAPTON521ICRU

0.229, 0, ZTHICK, FLAG FOR LAYER 3 IN CENTRAL PART

0, 0, 1, 0,

AIR521ICRU

0.0051, 0, ZTHICK, FLAG FOR LAYER 4 IN CENTRAL PART

0.521, 0.01, 0, 0,

KAPTON521ICRU

0.234, 0, ZTHICK, FLAG FOR LAYER 5 IN CENTRAL PART

0, 0, 2, 0,

AIR521ICRU

0.0051, 0, ZTHICK, FLAG FOR LAYER 6 IN CENTRAL PART

0, 0, 0, 0,

KAPTON521ICRU

0.229, 0, ZTHICK, FLAG FOR LAYER 7 IN CENTRAL PART

0.521, 0.01, 3, 0,

AIR521ICRU

0.0127, 0, ZTHICK, FLAG FOR LAYER 8 IN CENTRAL PART

0.521, 0.01, 0, 0,

KAPTON521ICRU

0.299, 0, ZTHICK, FLAG FOR LAYER 9 IN CENTRAL PART

0.521, 0.01, 4, 0,

AIR521ICRU

0.0051, 0, ZTHICK, FLAG FOR LAYER 10 IN CENTRAL PART
 0.521, 0.01, 0, 0,
 KAPTON521ICRU
 0.233, 0, ZTHICK, FLAG FOR LAYER 11 IN CENTRAL PART
 0.521, 0.01, 5, 0,
 AIR521ICRU
 0.0051, 0, ZTHICK, FLAG FOR LAYER 12 IN CENTRAL PART
 0.521, 0.01, 0, 0,
 KAPTON521ICRU
 0.23, 0, ZTHICK, FLAG FOR LAYER 13 IN CENTRAL PART
 0.521, 0.01, 6, 0,
 AIR521ICRU
 0.0127, 0, ZTHICK, FLAG FOR LAYER 14 IN CENTRAL PART
 0.521, 0.01, 0, 0,
 KAPTON521ICRU
 0.628, 0, ZTHICK, FLAG FOR LAYER 15 IN CENTRAL PART
 0.521, 0.01, 0, 0,
 AIR521ICRU
 0.521, 0.01, 0, 9, chamber wall
 AIR521ICRU
 0.521, 0.01, 0, 10, gap
 AIR521ICRU
 0.521, 0.01, 0, 11, container
 AIR521ICRU
 0, MRNGE
 ***** start of CM MIRROR with identifier mirror *****
 10, RMAX
 MIRROR
 18.873, 7.923, ZMIN, ZTHICK
 4.67, -6.645, XFMIN, XBMIN
 1, # LAYERS
 0.00508, thickness of layer 1
 0.521, 0.01, 0, 12,
 MYLAR521ICRU
 0.521, 0.01, 0, 13,
 AIR521ICRU
 0.521, 0.01, 0, 14,
 AIR521ICRU
 ***** start of CM JAWS with identifier jaws *****
 10, RMAX
 jaws
 2, # PAIRED BARS OR JAWS
 X
 28.0, 35.8, 0.56000, 0.71600, -0.56000, -0.71600,
 Y
 36.7, 44.5, 0.73400, 0.89000, -0.73400, -0.89000,

```

0.521, 0.01, 0, 0,
0.521, 0.01, 0, 0,
W521ICRU
0.521, 0.01, 0, 0,
W521ICRU
***** start of CM ARCCHM with identifier minibeam *****
100, RMAX
Column
58.9, ZSRC
60, ZRAD1
34, NUMBER OF CHAMBERS
0.06, WIDTHCHM
0.044, WIDTHSEP
10, ARCTHICK
5e-7, FRONTHCK
5e-7, BACKTHCK
0.84, WIDTH OF X WALL
-20, 20, XMIN1 XMAX2
75, ZMAX
0.521, 0.01, 0, 0,
AIR521ICRU
0.521, 0.01, 0, 0,
AIR521ICRU
0.521, 0.01, 0, 0,
AL521ICRU
0.521, 0.01, 0, 0, 1
W521ICRU
0.521, 0.01, 0, 0, 1
AIR521ICRU
0.521, 0.01, 0, 0,
AIR521ICRU
0.521, 0.01, 0, 0,
AIR521ICRU
0.521, 0.01, 0, 0,
AL521ICRU
*****end of all CMs*****
#####
:Start MC Transport Parameter:

Global ECUT= 0.521
Global PCUT= 0.01
Global SMAX= 5
ESTEPE= 0.25
XIMAX= 0.5
Boundary crossing algorithm= EXACT
Skin depth for BCA= 0

```

Electron-step algorithm= PRESTA-II
Spin effects= On
Brems angular sampling= Simple
Brems cross sections= BH
Bound Compton scattering= Norej
Compton cross sections= default
Pair angular sampling= Simple
Pair cross sections= BH
Photoelectron angular sampling= Off
Rayleigh scattering= Off
Atomic relaxations= Off
Electron impact ionization= Off
Photon cross sections= xcom
Photon cross-sections output= Off

:Stop MC Transport Parameter:

#####

A.3. DOSRZnrc Input for the Dose to Detector

The final stage of the simulations used DOSRZnrc to score the dose to a simulated detector. Note that the input is structured rather differently to the preceding inputs, being for a different system. The geometrical inputs section specifies the structure and media of the simulation environment. I/O control specifies the voxels to which dose should be scored, which are chosen to correspond to the active volumes. Geometric data on the detectors was supplied by the manufacturers with the condition of a non-disclosure agreement. Media are assigned to voxels by range, with subsequent assignment overwriting earlier specifications as necessary. DOSRZnrc includes the functionality to terminate the simulation before all histories are run if a target uncertainty is achieved. These quantities are specified under Monte Carlo inputs. The call for particle inputs from a phase space file is again $ISOURC = 21$, with the phase space output by the second phase. The transport settings and VRT options are specified at the end of the input [59].

TITLE= dosrznrc_template—dose to ptwe detector

#####

:start I/O control:

IWATCH= off

STORE INITIAL RANDOM NUMBERS= no

IRESTART= first

STORE DATA ARRAYS= yes

OUTPUT OPTIONS= short

ELECTRON TRANSPORT= normal

DOSE ZBOUND MIN= 6

DOSE ZBOUND MAX= 9

DOSE RBOUND MIN= 0

DOSE RBOUND MAX= 1

:stop I/O control:

#####

#####

:start Monte Carlo inputs:

NUMBER OF HISTORIES= 15000000000

INITIAL RANDOM NO. SEEDS= 26, 67

MAX CPU HOURS ALLOWED= 999

IFULL= dose and stoppers

STATISTICAL ACCURACY SOUGHT= 0.500

SCORE KERMA= no

:stop Monte Carlo inputs:

#####

#####

:start geometrical inputs:

METHOD OF INPUT= individual

Z OF FRONT FACE= 0.0

DEPTH BOUNDARIES= 25.0, 34.924, 34.953, 34.954, 34.98, 34.985, 35.015, 35.02, 35.084, 35.252, 35.61, 35.745, 35.885, 36.55, 40, 50

RADII= 0.0655, 0.075, 0.18, 0.2375, 0.2616, 0.275, 0.2812, 0.345, 20

MEDIA= AIR521ICRU,

H2O521ICRU,

RW3521ICRU,

AL521ICRU,

POLYETH521ICRU,

FR4521ICRU,

EPOXY521,

SI521ICRU,

COAX521;

DESCRIPTION BY= planes

MEDNUM= 1, 2, 3, 4, 5, 6, 7, 8, 9, 4, 4

START ZSLAB= 1, 2, 3, 4, 5, 5, 5, 6, 5, 11, 11

STOP ZSLAB= 2, 16, 14, 4, 14, 9, 8, 8, 11, 14, 14

START RING= 1, 1, 1, 1, 1, 1, 1, 1, 5, 5, 1

STOP RING= 9, 9, 8, 5, 5, 4, 3, 2, 5, 8, 2

:stop geometrical inputs:

#####

#####

:start source inputs:

INCIDENT PARTICLE= all

SOURCE NUMBER= 21

SOURCE OPTIONS= 0, 0, 0, 0

FILSPC= ../BEAM_ion_jaws_mini/04x04_MB_0_090eSource_3444.egsphp1

:stop source inputs:

#####

#####

:start MC transport parameter:

Global ECUT= 0.521

Global PCUT= 0.001

Global SMAX= 1e10

ESTEPE= 0.25

XImax= 0.5

Skin depth for BCA= 3

Boundary crossing algorithm= EXACT

Electron-step algorithm= PRESTA-II

Spin effects= on

Brems angular sampling= KM

Brems cross sections= BH

Electron Impact Ionization= On

Bound Compton scattering= On

Pair angular sampling= Simple

Photoelectron angular sampling= On

Rayleigh scattering= Off

Atomic relaxations= On

Set PCUT= 0

Set PCUT start region= 1

Set PCUT stop region= 1

Set ECUT= 0

Set ECUT start region= 1

Set ECUT stop region= 1

```

Set SMAX= 0
Set SMAX start region= 1
Set SMAX stop region= 1

:stop MC transport parameter:
#####
#####
:start variance reduction:

BREM SPLITTING= off
NUMBER OF BREMS PER EVENT= 1
CHARGED PARTICLE RUSSIAN ROULETTE= off
ELECTRON RANGE REJECTION= on
ESAVEIN= 2.0
RUSSIAN ROULETTE DEPTH= 0.0000
RUSSIAN ROULETTE FRACTION= 0.0000
EXPONENTIAL TRANSFORM C= 0.0000
PHOTON FORCING= off
START FORCING= 1
STOP FORCING AFTER= 1
CS ENHANCEMENT FACTOR= 1
CS ENHANCEMENT START REGION= 1, 1
CS ENHANCEMENT STOP REGION= 1, 1

:stop variance reduction:
#####
#####
:start plot control:

PLOTTING= off

:stop plot control:
#####

```

APPENDIX B

PERMISSION TO REPRODUCE FIGURES

Figure 1.1.

Original image was Figure 5.5 (b) from Chapter 5 “Treatment machines for external beam radiotherapy” of Podgorsak E B 2005. *Radiation Oncology Physics: A Handbook for Teachers and Students*. IAEA. Vienna, Austria. [3]



M.Edvardsen@iaea.org
Thu 12/22/2016 5:21 AM

Mark as unread

To: Davis, William;

● You forwarded this message on 12/22/2016 10:01 AM.

Action Items

Dear Mr Davis,

The IAEA can give you permission to reproduce Figure 5.5 (b) from IAEA Publication titled Radiation Oncology Physics: A Handbook for Teachers and Students to the extent and for the purposes detailed in your email. Kindly note that the IAEA retains the copyright.

We kindly ask you to clearly indicate that you are reproducing the Figure with permission by the IAEA. Please ensure due acknowledgement and reference to the following IAEA publication: International Atomic Energy Agency, PODGORSK E. B., "Treatment machines for external beam radiotherapy", Radiation Oncology Physics: A Handbook for Teachers and Students, IAEA, Vienna (2005) 123–160.

Best regards,

Ms Miriam EDVARDSEN | Publications Assistant (Marketing and Sales) |
Publishing section | Division of Conference and Document Services | Department of Management |
International Atomic Energy Agency | Vienna International Centre, PO Box 100, 1400 Vienna, Austria |
Email: M.Edvardsen@iaea.org | T: (+43-1) 2600-22530 | F: (+43-1) 2600-29302
Follow us on www.iaea.org



Figure 3.3.

Original image was Figure 3 from Beddar, A S, Mason D J, and O'Brien P F 1994. Absorbed dose perturbation caused by diodes for small field photon dosimetry. *Medical Physics*, 21(7) pp. 1075-1079. [65]



DATE OF REQUEST: December 21, 6016

FROM:

William Davis
333 - 2710 Main St, Saskatoon, SK, Canada, S7H 0M3

EMAIL ADDRESS: wmd145@mail.usask.ca

1. Permission is granted to:

William Davis, University of Saskatchewan Department of Physics and Engineering Physics

2. Permission is requested to use the following material:

P.R. Almond et al. / AAPM's TG-51 protocol for reference dosimetry of high-energy photon and electron beams / *Medical Physics* / 26(9) / 1847-1870 / 1999 / Figure 3: Schematic of the SSD or SAD setups which may be used for photon beam reference dosimetry.

3. For what purpose:

Reproduction of the above mentioned figure in M.Sc Thesis.

Authors seeking permission must also notify the first author of the article from which permission is being sought.

Permission is hereby granted: _____ 12/22/16
Signature Date

Submit via Email


Reset Form

The Association's Journals are *Medical Physics* and *Journal of Applied Medical Physics*
Member Society of the American Institute of Physics and the International Organization of Medical Physics

1631 Prince Street | Alexandria, VA 22314-2818 | phone 571.298.1300 | fax 571.298.1301 | www.aapm.org

Figure 5.6.

Original image was Figure 1 from Almond P R, Biggs P J, Coursey B M, Hanson W F, Huq M S, Nath R, and Rogers DWO 1999. AAPM's TG-51 protocol for clinical reference dosimetry of high-energy photon and electron beams. *Medical Physics*, 26(9), pp. 1847-1870. [34]

 **AMERICAN ASSOCIATION
of PHYSICISTS IN MEDICINE**

Angela R. Keyser
Executive Director
akeyser@aapm.org
571.298.1285

DATE OF REQUEST: December 21, 6016

FROM:
William Davis
333 - 2710 Main St, Saskatoon, SK, Canada, S7H 0M3

EMAIL ADDRESS: wmd145@mail.usask.ca

1. Permission is granted to:
William Davis, University of Saskatchewan Department of Physics and Engineering Physics

2. Permission is requested to use the following material:
A.S. Beddar et al. / Absorbed dose perturbation caused by diodes for small field dosimetry / *Medical Physics* / 21(7) / 1075 - 1079 / 1994 / Figure 1: Schematic diagram of the three different diodes orientations with respect to the central axis beam direction and water-phantom scanning direction.

3. For what purpose:
Reproduction of the above mentioned figure in M.Sc Thesis.

Authors seeking permission must also notify the first author of the article from which permission is being sought.

Permission is hereby granted: _____ 12/22/16
Signature Date

Submit via Email

Reset Form

The Association's Journals are *Medical Physics* and *Journal of Applied Medical Physics*
Member Society of the American Institute of Physics and the International Organization of Medical Physics

1631 Prince Street | Alexandria, VA 22314-2818 | phone 571.298.1300 | fax 571.298.1301 | www.aapm.org

LIST OF REFERENCES

- [1] Joiner M and van der Kogel A, 2009. *Basic Clinical Radiobiology*. Fourth Edition. Hodder Arnold. London, England.
- [2] Balagamwala E H, Chao S T, and Suh J H 2012. Principles of Radiobiology of Stereotactic Radiosurgery and Clinical Applications in the Central Nervous System. *Technology in Cancer Research and Treatment*, 11(1).
- [3] Podgorsak E B 2005. *Radiation Oncology Physics: A Handbook for Teachers and Students*. IAEA. Vienna, Austria.
- [4] Marks H 1952. Clinical Experience with Irradiation Through a Grid. *Radiology*. 58(3), pp. 338-342.
- [5] Mohiuddin M, Curtis D L, Grizos W T, and Komarnicky L 1990. Palliative Treatment of Advanced Cancer Using Multiple Nonconfluent Pencil Beam Radiation: A Pilot Study. *Cancer*, 66(1), pp. 1159-1170.
- [6] Mohiuddin M, Fujita M, Regine W F, Megooni A S, Ibbott G S, and Ahmed M M 1999. High-dose spatially-fractionated radiation (GRID): a new paradigm in the management of advanced cancers. *International Journal of Radiation Oncology*, 45(3), pp. 721-727.
- [7] Ha J K, Zhang G, Naqvi S A, Regine W F, Yu C X 2006, Feasibility of delivering grid therapy using a multileaf collimator. *Medical Physics*, 33(1), pp. 76-82.
- [8] Neuner G, Mohiuddin M D, Walde N V, Goloubeva O, Ha J, Yu C X, and Regine W F 2012. High-dose spatially fractionated GRID radiation therapy (SFGRT): a comparison of treatment outcomes with cerroben vs MLC SFGRT. *International Journal of Radiation Oncology*, 82(5), pp. 1642-1649.
- [9] Slatkin D N, Spanne P, Dilmanian F A, and Sandborg M 1992. Microbeam Radiotherapy. *Medical Physics*. 19(6), pp 1395-1400.
- [10] Slatkin D N, Spanne P, Dilmanian F A, Gebbers J O, and Laissue J A 1995. Subacute neuropathic effects of microplanar beams of x-rays from a synchrotron wiggler. *Proceedings of the National Academy of Sciences of the United States of America*. 92(19), pp. 8783-8787.
- [11] Brauer-Krisch E, Serduc R, Siegbahn E A, Le Duc G, Prezado Y, Bravin A, Blattmann H, and Laissue J A, 2010. Effects of pulsed, spatially fractionated, microscopic synchrotron X-ray beams on normal and tumoral brain tissue. *Mutation Research*, 704(1-3), pp 160-166.
- [12] Laissue J *et al.* 1998. Neuropathology of ablation of rat gliosarcomas and contiguous brain tissues using a microplanar beam of synchrotron-wiggler-generated X rays. *International Journal of Cancer*, 78(5), pp. 654-660.
- [13] Dilmanian F A, *et al.* 2006. Interlace x-ray microplanar beams: A radiosurgery approach with clinical potential. *Proceedings of the National Academy of Sciences of the United States of America*, 103(25), pp. 9709-9714.

- [14] Regnard P *et al.*, 2008. Irradiation of intracerebral 9L gliosarcoma by a single array of microplanar x-ray beams from a synchrotron: balance between curing and sparing. *Physics in Medicine and Biology*, 53(4), pp. 861-878.
- [15] Serduc R *et al.*, 2009. Synchrotron microbeam radiation therapy for rat brain tumor palliation - influence of the microbeam width at constant valley dose. *Physics in Medicine and Biology*, 54(21), pp. 6711-6724.
- [16] Bouchet A *et al.*, 2010. Preferential effect of synchrotron microbeam radiation therapy on intracerebral 9L gliosarcoma vascular networks. *International Journal of Radiation Oncology*, 78(5), pp. 1503-1512.
- [17] Crosbie J C *et al.*, 2010. Tumor cell response to synchrotron microbeam radiation therapy differs markedly from cells in normal tissues. *International Journal of Radiation Oncology Biology Physics*, 77(3), pp 886-894.
- [18] Romanelli P and Bravin A 2011. Synchrotron-generated microbeam radiosurgery: a novel experimental approach to modulate brain function. *Neurological Research*, 33(8), pp. 825-831.
- [19] Dilmanian F A *et al.*, 2002. Response of rat intracranial 9L gliosarcoma to microbeam radiation therapy. *Neuro-Oncology*, 4(1), pp. 26-30.
- [20] Deman P *et al.* 2012. Monochromatic Minibeams Radiotherapy: From Healthy Tissue Sparing Studies Toward First Experimental Glioma Bearing Rats Study. *International Journal of Radiation Oncology*, 82(4), pp. e693-e700.
- [21] Prezado Y, Deman P, Varlet P, Jouvion G, Gil S, Le Clec'H C, Bernard H, Le Duc G, and Sarun S 2015. Tolerance to Dose Escalation in Minibeam Radiation Therapy Applied to Normal Rat Brain: Long Term Clinical, Radiological and Histopathological Analysis. *Radiation Research*, 184(3), pp. 314-321
- [22] Babcock K, Sidhu N, Kundapur V, and Ali K 2011. Collimator design for experimental minibeam radiation therapy. *Medical Physics*, 38(4), pp. 2192-2197.
- [23] Cranmer-Sargison G, Crewson C, Davis W, Sidhu N, and Kundapur V, 2015. Medical linear accelerator mounted mini-beam collimator: design, fabrication, and dosimetric characterization. *Physics in Medicine and Biology*, 60(17), pp. 6991-7005.
- [24] Podgorsak E B 2010. *Radiation Physics for Medical Physicists*. 2nd Edition. Springer. Berlin, Germany.
- [25] Seltzer S M, Bartlett D T, Burns D T, Dietze G, Menzel H G, Paretzke H G, and Wambersie A 2011. Fundamental Quantities and Units for Ionizing Radiation (Revised). *Journal of the ICRU*, 11(1).
- [26] Griffiths D J 1999. *Introduction to Electrodynamics*. 3rd Edition. Pearson. Upper Saddle River, NJ, United States.

- [27] Evans R D 1955. *The Atomic Nucleus*. McGraw-Hill Inc. New York, NY, United States.
- [28] Storm E and Israel H 1970. Photon Cross Sections for 1 keV to 100 MeV for Elements Z=1 to Z=100. *Nuclear Data Tables*, A7, pp. 565-681.
- [29] Rangacharyulu C 2013. *Physics of Nuclear Radiations: Concepts, Techniques and Applications*. CRC Press. Boca Raton, FL, United States.
- [30] Attix F H 1991. *Introduction to Radiological Physics and Radiation Dosimetry*. 1st Edition. Wiley-VCH. Hoboken, NJ, United States.
- [31] Hirayama H 2000. *Lecture Note on Photon Interactions and Cross Sections*. High Energy Accelerator Research Organization. Oho, Japan.
- [32] Klein O and Nishina Y Z 1929. *Über die Streuung von Strahlung durch freie Elektronen nach der neuen relativistischen Quantendynamik von Dirac*. *Zeitschrift für Physik*, 52(11), 853-868.
- [33] Johns H E and Cunningham J R 1983. *The Physics of Radiology*. 4th Edition. Charles C Thomas. Springfield, IL, United States.
- [34] Almond P R, Biggs P J, Coursey B M, Hanson W F, Huq M S, Nath R, and Rogers DWO 1999. AAPM's TG-51 protocol for clinical reference dosimetry of high-energy photon and electron beams. *Medical Physics*, 26(9), pp. 1847-1870.
- [35] Kase K R, Bjärngard B E, and Attix F H 1985. *The Dosimetry of Ionizing Radiation*. Volume 1. Academic Press Inc. Orlando, FL, United States.
- [36] Metcalfe P, Kron T, and Hoban P 1997. *The Physics of Radiotherapy X-Rays from Linear Accelerators*. Medical Physics Publishing. Madison, WI United States.
- [37] Gray L H 1936. An Ionization Method for the Absolute Measurement of γ -Ray Energy. *Proceedings of the Royal Society A*, 156(889), pp. 578-596.
- [38] Spencer L V and Attix F H. 1955. A theory of cavity ionization. *Radiation Research*, 3(3), pp. 239-254.
- [39] Hill R, Healy B, Holloway L, Kuncic Z, Thwaites D, and Baldock C 2014. Advances in kilovoltage x-ray beam dosimetry. *Physics in Medicine and Biology*, 59(6), pp. 183-231.
- [40] Seco J, Clasié B, and Partridge M 2014. Review on the characteristics of radiation detectors for dosimetry and imaging. *Physics in Medicine and Biology*, 59(20), pp. 303-347.
- [41] Ma C *et al.* 2001. AAPM protocol for 40-300 kV x-ray dosimetry in radiotherapy and radiobiology. *Medical Physics*, 28(6), pp. 868-897.

- [42] Andreo P, Burns D T, Hohlfeld K, Huq M S, Kanai T, Laitano F, Smythe V G, and Vynckier S 2000. *Absorbed Dose Determination in External Beam Radiotherapy: An International Code of Practice for Dosimetry Based on Standards of Absorbed Dose to Water*. International Atomic Energy Agency. Vienna, Austria.
- [43] Huq M S, Andreo P, and Song H 2001. Comparison of the IAEA TRS-398 and AAPM TG-51 absorbed dose to water protocols in the dosimetry of high-energy photon and electron beams. *Physics in Medicine and Biology*, 46(11), pp. 2985-3006.
- [44] Fraass B, Doppke K, Hunt M, Kutcher G, Starkschall G, Stern R, and Van Dyke J 1998. American Association of Physicists in Medicine Radiation Therapy Committee Task Group 53: Quality assurance for clinical radiotherapy treatment planning. *Medical Physics*, 25(10), pp. 1773-1828.
- [45] JCGM/WG 1, 2008. *JCGM 100:2008 Evaluation of measurement data – Guide to the expression of uncertainty in measurement*. Joint Committee for Guides in Metrology. Paris, France.
- [46] Nelson W R, Hirayama, H, and Rogers D W O 1985. *SLAC-265: The EGS4 Code System*. National Technical Information Service. Springfield, VT, United States.
- [47] Bielajew A. 2006. *The Monte Carlo Simulation of Radiation Transport*. University of Michigan. Ann Arbor, MI, United States.
- [48] Metropolis N and Ulam S 1949. The Monte Carlo Method. *Journal of the American Statistical Association*, 44(247), pp. 335-341.
- [49] Lyons L 1986. *Statistics for nuclear and particle physicists*. Press Syndicate of the University of Cambridge. Cambridge, England.
- [50] Sobol I M 1974. *The Monte Carlo Method*. University of Chicago Press. Chicago, IL, United States.
- [51] Chetty I J *et al.* 2007. *Report of the AAPM Task Group No. 105: Issues associated with clinical implementation of Monte Carlo-based photon and electron external beam treatment planning*. *Medical Physics*, 34(12), pp. 4818-4853.
- [52] Berger M J 1963. Monte Carlo calculation of the penetration and diffusion of fast particles. *Methods in Computational Physics*, 1, pp. 135-215.
- [53] Kawrakow I, Mainegra-Hing E, Rogers D W O, Tessier F, and Walters B R B 2013. *The EGSnrc Code System: Monte Carlo Simulation of Electron and Photon Transport*. NRCC Report PIRS-701. National Research Council of Canada. Ottawa, Canada.
- [54] Jenkins T M, Nelson W R, and Rindi A 1988. *Monte Carlo Transport of Electrons and Photons*. Plenum Press. New York, NY, United States.

- [55] Seco J and Verhaegen F 2013. *Monte Carlo Techniques in Radiation Therapy*. CRC Press. Boca Raton, FL, United States.
- [56] Rogers D W O, Walters B, and Kawrakow I 2016. *BEAMnrc Users Manual*. NRCC Report PIRS-0509(A)revL. National Research Council of Canada. Ottawa, Canada.
- [57] Rogers D W O, Faddegon B A, Ding G X, Ma C-M, and We J 1995. BEAM: A Monte Carlo code to simulate radiotherapy treatment units. *Medical Physics*, 22(5), pp. 503-524.
- [58] Walters B, Kawrakow I, and Rogers D W O 2016. *DOSXYZnrc Users Manual*. NRCC Report PIRS-794revB. National Research Council of Canada. Ottawa, Canada.
- [59] Rogers D W O, Kawrakow I, Seuntjens J P, Walters B R B, and Mainegra-Hing E 2016. *NRC User Codes for EGSnrc*. NRCC Report PIRS-702(revC). National Research Council of Canada. Ottawa, Canada.
- [60] Aspradakis M M, Byrne J P, Palmans H, Conway J, Rosser K, Warrington A P, and Duane S 2010. *Small Field MV Photon Dosimetry: IPEM Report Number 103*. Institute of Physics and Engineering in Medicine. York, UK.
- [61] Burlin T E 1966. A general theory of cavity ionisation. *British Journal of Radiology*, 39, pp. 727-734.
- [62] Klein E E *et al.* 2009. Task Group 142 report: quality assurance of medical accelerators. *Medical Physics*, 36(9), pp. 4197-4212.
- [63] Das I J, Ding G X, and Ahnesjö A 2007. Small fields: Nonequilibrium radiation dosimetry. *Medical Physics*, 35(1), pp. 206-215.
- [64] Cranmer-Sargison G, Charles P H, Trapp J V, and Thwaites D I, 2013. A methodological approach to reporting corrected small field relative outputs. *Radiotherapy and Oncology*, 109(3), pp. 350-355.
- [65] Beddar, A S, Mason D J, and O'Brien P F 1994. Absorbed dose perturbation caused by diodes for small field photon dosimetry. *Medical Physics*, 21(7) pp. 1075-1079.
- [66] Babcock K, Cranmer-Sargison G, and Sidhu N 2008. Increasing the speed of DOSXYZnrc Monte Carlo simulations through the introduction of nonvoxelated geometries. *Medical Physics*, 35(2), pp. 633-644.
- [67] Cranmer-Sargison G, Weston S, Evans J A, Sidhu N P, and Thwaites D I 2011. Implementing a newly proposed Monte Carlo based small field dosimetry formalism for a comprehensive set of diode detectors. *Medical Physics*, 38(12), pp. 6592-6602.

- [68] Cranmer-Sargison G, Weston S, Evans J A, Sidhu N P, and Thwaites D I 2012. Monte Carlo modelling of diode detectors for small field MV photon dosimetry: detector model simplification and the sensitivity of correction factors to source parameterization. *Physics in Medicine and Biology*, 57(16), pp. 5141-5153.
- [69] Scott A J D, Kumar S, Nahum A E, and Fenwick J D 2012. Characterizing the influence of detector density on dosimeter response in non-equilibrium small photon fields.. *Physics in Medicine and Biology*, 57(14), pp. 4461-4476.
- [70] Moignier C, Huet C, and Makovicka L 2014. Determination of the $k_{Q_{clin}, Q_{msr}}^{f_{clin}, f_{msr}}$ correction factors for detectors used with an 800 MU/min CyberKnife system equipped with fixed collimators and a study of detector response to small photon beams using a Monte Carlo method. *Medical Physics*, 41(7), pp. 071702.
- [71] Alfonso R *et al.* 2008. A new formalism for reference dosimetry of small and non-standard fields. *Medical Physics*, 35(11), pp. 5177-5186.
- [72] Smith S, Davis W, Kundapur V, Moiseenko V, Anderson D, and Cranmer-Sargison G 2015. *Poster: Cellular Response to High Energy Mini-Beam Radiation*. 2015 Annual Saskatchewan Cancer Research Conference. Saskatoon, Canada.
- [73] Alexander A, Crewson C, Davis W, Mayer M, Cranmer-Sargison G, and Kundapur V 2016. *Presentation: Design to delivery of spatially fractionated mini-beam canine radiotherapy*. 2016 COMP Annual Scientific Meeting. St. John's, Canada.